

Dissertation
submitted to the
Combined Faculties for the Natural Sciences and for Mathematics
of the Ruperto-Carola University of Heidelberg, Germany
for the degree of
Doctor of Natural Sciences

Put forward by
Dipl.Phys. Ulrich Schmidt
born in Basel/CH

oral examination: 4 February 2010

Dynamics of intracellular macromolecules: A mesoscopic simulation study

Referees:

Prof. Dr. Michael Hausmann
Dr. Matthias Weiß

Zusammenfassung

Diese Arbeit untersucht mittels mesoskopischer Simulationsmethoden das dynamische Verhalten von Makromolekülen in lebenden Zellen. Im Fokus stehen die großen Molekülklassen der integralen Membranproteine und der flexiblen Biopolymere. Im ersten Teil dieser Arbeit wird untersucht welche Auswirkungen ein 'hydrophober Mismatch' (HM) mit der umgebenden Membran auf die Dynamik und das kollektive Verhalten integraler Membranproteine besitzt. Dieser geometrische Defekt führt zur Anziehung zwischen Proteinen mit gleichem HM und kann zur vollständigen Separation von Proteinen mit unterschiedlichem HM führen. Basierend auf diesen Ergebnissen schlagen wir ein Model vor wie Membranproteine in lebenden Zellen verteilt werden. Weiterhin wird untersucht, ob und inwieweit Clustering von Membranproteinen deren Diffusionseigenschaften beeinflusst. Im zweiten Teil wenden wir uns der Bewegung eines flexiblen Polymers durch eine enge Pore zu. Wir untersuchen, wie sich das Translokationsverhalten des Polymers ändert, wenn die Qualität des Lösungsmittels auf beiden oder nur auf einer Seite der Pore verschlechtert wird. Überraschenderweise variiert das Translokationsverhalten im ersten Fall nicht, wohingegen im zweiten Fall eine Beschleunigung der Bewegung durch die Pore beobachtet wird.

Abstract

This work uses mesoscopic simulation techniques to study the dynamical behaviour of macromolecules in living cells. Emphasis is put on the large molecule classes of integral membrane proteins and flexible biopolymers. In the first part, the influence of a 'hydrophobic mismatch' (HM) with the surrounding membrane on the dynamics and on the collective behaviour of integral membrane proteins is analysed. This geometrical defect creates an attraction between proteins with like HM, and is able to segregate proteins with different HM. Based on these results, we propose a model of how sorting of membrane proteins occurs in living cells. Furthermore, we study whether and to which extent the clustering of membrane proteins alters their diffusional character. In the second part, we address the translocation of a flexible polymer through a narrow pore. We analyse how the translocation behaviour is altered if the solvent quality is decreased either on both sides or only on one side of the pore. Surprisingly, the translocation behaviour does not change in the first case while an accelerated translocation is observed in the second case.

The most exciting phrase to hear in science,
the one that heralds new discoveries, is not
'Eureka!' (I found it!) but 'That's funny ...'

Isaac Asimov

Contents

1	Introduction	1
I	Prerequisites	7
2	Membranes, Polymers & Proteins	9
2.1	Membranes	9
2.2	Polymers	15
2.3	Proteins	20
3	Membrane Simulations	27
3.1	Dissipative particle dynamics	27
3.2	DPD membranes	36
II	Results	39
4	Hydrophobic mismatching	41
4.1	Introduction to hydrophobic mismatching	41
4.2	Protein clustering	43
4.3	Protein segregation	59
4.4	Hydrophobic mismatching as a lipid environment sensor	62
4.5	Protein sorting by hydrophobic mismatching	65
5	Diffusion of oligomers	75
5.1	Diffusion in a nutshell	75
5.2	Dynamics of oligomers	80
6	Polymer Translocation	93
6.1	Basic setup	94
6.2	Static polymer properties	96
6.3	Translocating polymers	102

CONTENTS

7 Summary & Outlook	111
 III Appendix	 115
A Integration schemes	117
A.1 Integrating the NpT ensemble	117
B List of DPD parameters	119
B.1 Parameters for the NVT and NpT ensemble	119
B.2 Conversion to SI units	120
 Bibliography	 121
 Acknowledgement	
 List of publications	

Chapter 1

Introduction

Complex systems represent a vast research area in the natural sciences especially in physics. We refer here to a complex system as an ensemble of interconnected and interacting components whose collective behaviour is not obvious from the properties of the isolated components. The character of the system as a whole thus reflects the interplay between the individual components and collective phenomena are appreciated. The interaction between the single parts are governed by fundamental laws of physics and can thus be described by the universal language of mathematics.

A prime example for complex systems are cells of living organisms. An accurate characterization of generic phenomena common to all cells requires the application of concepts from classical and statistical mechanics, elasticity theory, hydrodynamics and, in parts, electrodynamics. Going to atomistic details, e.g. concerning protein folding, even quantum mechanical principles have to be taken into account.

Classical mechanics and elasticity theory are used to describe mechanical properties of the cell and its individual parts like the cell membrane or intracellular biopolymers. For example, such properties can be a bending rigidity or a compression modulus (Boal02). A correct hydrodynamic treatment allows to investigate the motion of molecules in a cell's interior as well as in the various (two-dimensional) cellular membranes that can both be interpreted as complex fluids. A prominent example here is the diffusion of membrane inclusions (Saffman75). Statistical mechanics is appropriate to investigate membranes, a huge structural class of intracellular surfaces and interfaces consisting of a vast number of lipid molecules (Safran03). Electrodynamics is appropriate to calculate the membrane potential which is a key factor in signal transduction in nerve cells (Hancock05). Finally, the accurate exploring and understanding of chemical reactions that occur permanently in living cells ultimately has to be addressed in a thorough quantum mechanical framework.

Introduction

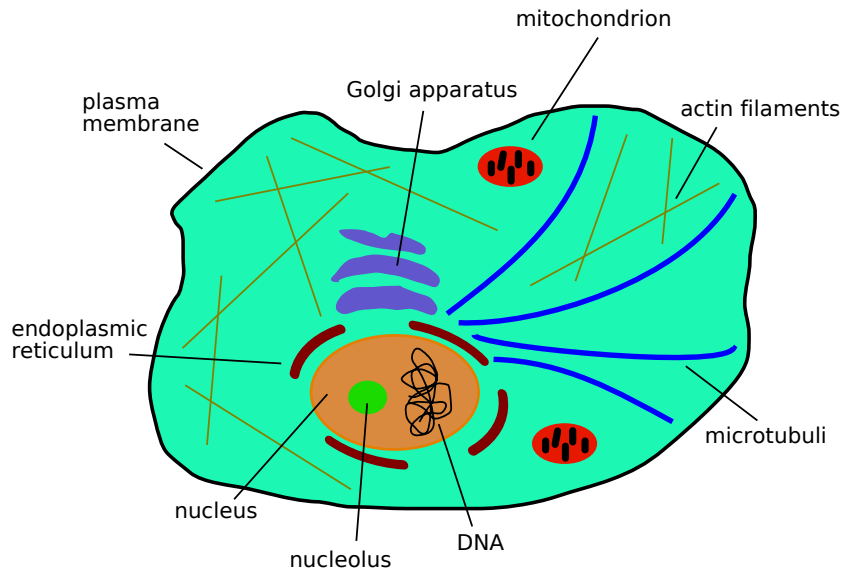


Figure 1.1: *Schematic drawing of a typical eukaryotic cell.*

Since living cells can be regarded as open thermodynamic systems, approaches of statistical thermodynamics play a particular role in describing their behaviour and their evolution. Concepts connected with entropy, free energy and the chemical potential are useful tools to investigate single cells and sub-systems contained therein. Moreover, methods from non-equilibrium thermodynamics are also necessary to investigate living cells.

In the past years, the strategy to address biological questions with the help of physics and mathematics has proven to be very successful. For instance, the emergence of various shapes of red blood cells could be successfully explained by a single-parameter model of the underlying membrane mechanics (Lim02). Another example covers the dynamical growth and shrinkage of microtubules, intracellular filaments, via a stochastic model (Mitchinson84; Flyvbjerg94). Recently, the motility of intracellular pathogens by actin filaments was also investigated (Cossart04; Shenoy07). Accompanied with recent developments in optical devices and the ever-growing capability of computational resources, tremendous progress has been achieved in understanding complex living systems. In addition, mathematical modeling and simulations contributed in large parts to recent developments in biophysical research. Following these lines, this work is intended to elucidate the dynamics of intracellular macromolecules by using computer simulations. Before we are going to discuss these results in detail, we would like to recapitulate basic knowledge about cells and to provide a biological motivation. As pointed out before, cells are the structural and functional units of all living

organisms. An organism is classified as living if several conditions are fulfilled. These include the existence of a regulated metabolism, the ability to grow and to respond to stimuli. Furthermore, the organism should be able to reproduce and to adapt to its environment. All these demands are met by cells, it is thus no surprise that cells are also termed the basic building blocks of life (Alberts02; Lodish04; Schrödinger44). The word 'cell' originates from the Latin *cellula* meaning a small room. The English scientist *Robert Hooke*¹ coined this term since the tiny compartments in cork he saw under his microscope reminded him of the small rooms monks lived in (Hooke65).

In general, one can distinguish between two kinds of cells: prokaryotes and eukaryotes. Prokaryotes possess less intracellular organization than eukaryotes, for example no specialized compartments. The most striking difference is the absence of a nucleus. In this compartment, eukaryotes store their genetic information in form of deoxyribonucleic acid (DNA).

In contrast to the very tidy and spartan appearance of cloistral rooms, typical eukaryotic cells are very dense and crammed. Their interior is filled with a visco-elastic medium (Guigas07), the *cytoplasm*. This medium represents a crowded solution of water, the universal biological solvent, and a plethora of different chemical molecules. Their individual sizes range from single hydrogen atoms via small lipid molecules to complex polypeptides (proteins) and up to giant macromolecules like the ribosome, the manufacturer of proteins.

A cell's structure is largely determined and supported by an internal scaffold, the *cytoskeleton*. It is created by various types of filaments which span the whole cell interior. These highly dynamic entities enable the cell to move or to change its size and shape. Some of these filaments serve as narrow tracks for directed transport of intracellular cargo by small motor proteins. These motors act as towing vehicles pulling spherical transport containers along these tracks.

In eukaryotes, the intracellular anatomy is supplemented by numerous independent compartments. Vital processes are distributed among these highly developed organelles giving each organelle its own particular function. Some important representatives of this family are the nucleus where the genetic code is stored, the mitochondria representing the power plants of the cell or the lysosomes providing efficient cleaning and waste disposal.

In addition to these sharply defined intracellular compartments, the cell has a further organelle that is distributed throughout the whole cell. It is called the *endoplasmic reticulum* (ER) and forms an interconnected network of tubules, vesicles and cisternae. It is mainly involved in metabolic and synthesizing processes.

The cell and its internal organelles are separated from their environment by mem-

¹mainly known from Hooke's law of elasticity

Introduction

branes, thin and flexible envelopes, typically a few nanometers thick. They are organized as two opposing leaflets each consisting of individual lipid molecules. Lipids are extraordinary molecules, one remarkable property of which being their amphiphilic nature. That means lipids possess both a hydrophilic and a hydrophobic part. Owing to this intrinsic characteristic, lipids have the ability to self-assemble into sheet-like structures (Boal02).

During the last decade, a growing interest in lipids has emerged culminating in the creation of the term *lipidomics* (Mouritsen05). In the advent of membrane science, membranes were thought to be passive envelopes only representing a boundary layer (Gorter25) with a mere protective function. Although the individual lipids in the two membrane leaflets were seen as very dynamic, the membrane as a whole did not achieve the status of an active entity.

The formulation of the fluid-mosaic membrane model by Singer & Nicholson in 1972 (Singer72), turned this inert picture of membranes into a biologically and chemically active one. The crucial ingredient in this model are proteins being either associated with or integrated into the membrane. The latter class of proteins are consequently termed (trans-)membrane or integral proteins. Because of the great abundance of membrane-associated proteins (nearly half of all proteins interact with membranes and two thirds of these are transmembrane proteins), they represent an important functional class.

Transmembrane proteins possess a hydrophobic core, the transmembrane domain (TMD), capped on either end by a hydrophilic portion. To place such proteins into a lipid bilayer, the cell has developed sophisticated processes that are carried out either during or after protein synthesis. Due to their spatial location, they establish a connection between topologically distinct spaces. According to this property, these proteins often serve as transporters, channels, receptors or enzymes (Rapoport07; Wikstrom98; Pawson97). Apart from that, membrane proteins can also be involved in creating structural changes of their host bilayer (Wallace90; Illya08; Reynwar07).

Despite their role in active processes as described above, membranes also serve as protective barriers against noxious intruders. Among these pathogens are on the one hand autonomous organisms like bacteria, fungi and eukaryotic parasites. All these microbes perform most of their metabolic functions themselves, the occupied host only serves as a nutrient source.

On the other hand, there are *viruses* that (ab-)use the host cell and its internal machinery for their own replication and proliferation. In contrast to other pathogens, viruses are not considered as living since they lack essential features connected with living organisms, e.g. a regulated metabolism. Although there is a wide variety of different kinds of viruses, they share a common construction: a piece of genetic information, DNA or RNA, is wrapped by a protective shell of proteins (Crick56). This so-called *virion* may additionally be enclosed by a lipid

membrane that facilitates the entry into potential host cells.

Upon entry, the virus starts to ensconce itself in the cell interior and to exploit the cell's machinery for its own needs. The timetable for successful viral replication and proliferation includes i) replication of the viral genome, ii) synthesis of viral proteins, iii) re-assembly into progeny virions and iv) egress and spreading to neighboring cells. The viral replication rate is remarkable, a single virion can be the source of more than 1000 new viral genome-protein particles.

Manipulation of the host cell begins shortly after the virus has entered the cell. Being inside, the virus has to find an appropriate niche where its lethal cargo can be replicated without being disturbed by the cell's cleaning machinery. To this end, the intracellular trafficking systems is exploited, delivering the viral genome to its preferred site of replication (Sodeik00). Viral particles of Hepatitis C, for example, establish replication cavities at the endoplasmic reticulum (Appel06; Moradpour07).

Newly replicated viral DNA/RNA is then transformed into viral proteins via the host's transcription and translation machinery. As a consequence, the synthesis of host-cell macromolecules can be severely disturbed and even completely inhibited (Kääriäinen84). Assembly of progeny virion occurs at various sites inside the cell, be it near the endoplasmic reticulum or at the plasma membrane (Stephens88). To get exported from the host cell and to spread the viral genome throughout the host organism, the internal trafficking system is again abused. Vesicular trafficking pathways can be redirected (Hackstadt00) to successfully leaving the host cell. In some cases virion replication is extremely high resulting in cell lysis, i.e. the cell breaks open and the present virions have direct access to the extracellular space.

In this work, we address dynamical aspects of intracellular macromolecules at the level of the endoplasmic reticulum connected to viral replication. The study of intracellular processes usually involves elaborate light microscopy approaches, e.g. confocal or TIRF (total internal reflection) microscopy. However, their resolution is diffraction-limited and even more sophisticated techniques like STED (stimulated emission depletion (Hell94)) are not capable to resolve structures smaller than approximately $20nm$. To overcome this barrier, we use extensive computer simulations that are able to elucidate dynamics of single molecules inside the cell.

The computer simulations used throughout this work operate on a mesoscopic, i.e. coarse-grained, level. Main advantages of this approach are the access to longer time and larger length scales as compared to atomistic simulation techniques. Neglecting details on the Ångström scale has another positive side effect: our simulational results can readily be interpreted in a more universal framework. They are not restricted to virus-host systems but rather describe generic physical mechanisms that are common to all cells.

Introduction

The present work can roughly be divided into two parts. The first part focuses on the dynamics of integral membrane proteins that possess a so-called *hydrophobic mismatch* (HM) with the surrounding lipid bilayer. That means, they are either too long or too short to fit perfectly into the lipid bilayer. We analyze how this geometrical defect can influence the motion and the behaviour of membrane inclusions. Based on these results, we propose a model of how transmembrane proteins may organize their spatial distribution in living cells. The latter represents a crucial task for endogenous as well as for viral proteins.

The second part investigates a prevalent event in biological systems, that is the translocation of a linear polymer through a narrow pore. Prominent examples are DNA/RNA translocation through nuclear pores (Kohler07) or the escape of viral RNA from replication cavities as observed during Hepatitis C virus replication (Moradpour07). Here, we aim at elucidating the physics of the translocation process when different solvents are present on each side of the pore. The next chapter will give an introduction to membranes, polymers and basic biological concepts. We present how membranes can be treated mathematically and discuss their mechanical properties. Next, we explore the nature of polymers and introduce two models that are used to address problems in polymer physics. To complement this introductory chapter, we give a brief introduction to protein synthesis and how these macromolecules are distributed throughout the cell.

Chapter 3 contains a detailed introduction to our preferred simulation technique which is called *dissipative particle dynamics* (DPD). We summarize basic principles of this particle-based simulation method, discuss assets and drawbacks and show its application to biological systems. Numerical integration procedures of our simulations are provided in the appendix.

After these preliminary sections we discuss in Chapter 4 the influence of hydrophobic mismatching on the dynamics of integral membrane proteins. We derive that hydrophobic mismatching can facilitate aggregation and segregation of membrane proteins and acts as a guide towards membrane regions where the HM is minimized. We propose a simple HM-based model for protein sorting along the secretory pathway.

Chapter 5 can be seen as a direct application of HM-induced protein clustering presented in the preceding chapter. We here discuss whether and to which extent oligomerization of transmembrane proteins alters the diffusional properties of the involved individual proteins as experimentally observed.

Driven polymer translocation through a nanopore is discussed in Chapter 6. As pointed out before, we here solely focus on effects arising from different solvent qualities on each side of the nanopore.

In the last chapter, we briefly review our results and conclude with an outlook on possible future research.

Part I

Prerequisites

Chapter 2

Membranes, Polymers & Proteins

This chapter will give an introduction to mathematical descriptions of membranes and polymers. In the first part, the focus is on fluid membranes and the physical principles governing their behaviour. In the second part, emphasis is put on a short but thorough description of polymers. The chapter is completed with a short section on the synthesis and the intracellular distribution of transmembrane proteins.

2.1 Membranes

In biological systems, membranes are the most abundant and also the most important structures. Without membranes, cells would not have a defined boundary and their agglomeration into more complex organisms would fail. In this section, we review how biological membranes are constructed, describe their mechanical properties, and give a description on how to treat membranes mathematically.

2.1.1 Self-assembly of lipid bilayers

Biological membranes are made of lipids, amphiphilic molecules with a hydrophilic head and a hydrophobic tail region (Figure 2.1). The hydrophilic head group consists of a polar molecule that is covalently linked to one or two non-polar hydrocarbon chain(s). Lipids possess the remarkable property that, when being exposed to an aqueous environment, they start to self-assemble into higher-order structures. This process is driven by the aversion of the hydrophobic parts to contact with water (Boal02). Depending on concentration, shape and other factors like temperature, lipids are able to form a variety of structures from simple micelles and flat lipid bilayers to winding sponge-like structures.

If the lipid head and tail group have a similar cross-sectional area, i.e. if the lipid

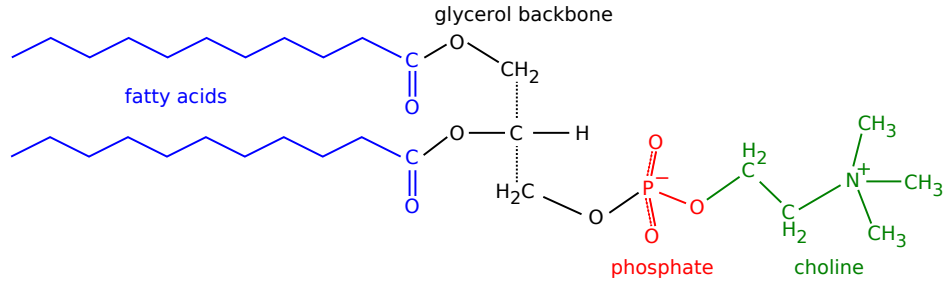


Figure 2.1: A typical glycerophospholipid, here phosphatidylcholine, consists of a polar head group (here choline) that is linked via a phosphate group (red) to a glycerol backbone (black). Attached to the latter are strongly hydrophobic fatty acid chains (blue).

can be approximately represented by a cylinder, the result of the self-assembly process is a lipid bilayer. A bilayer is made of two opposing leaflets consisting of lipids with the head groups facing the water and the tail group being buried in the bilayer interior, cf. Figure 2.2. Lipids in the individual leaflets of the bilayer are restricted to lateral diffusion in the corresponding leaflet. The case that single lipids do a flip-flop into the opposing leaflet is extremely rare. At first guess, one might assume the self-assembly process being of energetic origin. However, a more detailed analysis shows that this process is in fact entropy driven. Suppose a single blob of lipids as a reference state with zero free energy and no interaction between the lipid molecules in the blob. The removal of a single molecule from the blob into the solvent is accompanied by an energy penalty E_{pen} . This energy cost is simply the product of the lateral surface area of a molecule and the surface tension between water and the molecule's hydrophobic region yielding (Boal02)

$$E_{pen} = 2\pi R\ell\gamma \quad (2.1)$$

Here, R is the radius and ℓ the length of the cylindrical amphiphile, and γ denotes the surface tension; the contributions from the caps of the cylinder have been omitted.

We furthermore assume the solution of molecules to be dilute so that the dissolved amphiphiles can be regarded as an ideal gas. The entropy per molecule, S_{gas} , of an ideal gas with density ρ is given by

$$S_{gas} = k_B \left[\frac{5}{2} - \ln(\rho \cdot \lambda^3) \right] \quad \text{with} \quad \lambda = \frac{h}{\sqrt{2\pi m k_B T}} \quad (2.2)$$

where λ is the thermal de Broglie wavelength. It is now straightforward to calculate at which density a cross-over between the condensed and the dissolved

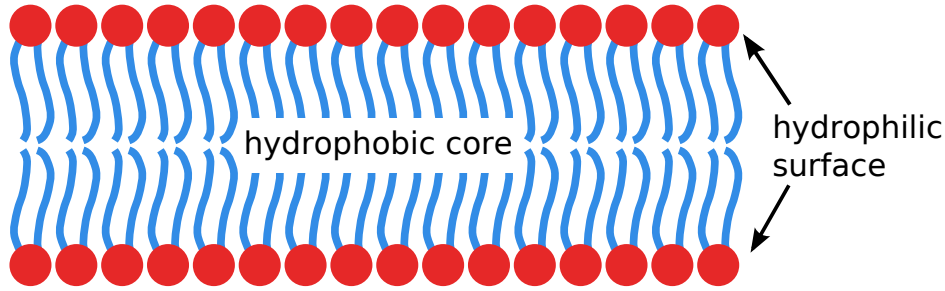


Figure 2.2: Schematic representation of a lipid bilayer consisting of cylindrical lipid molecules. The hydrophilic head groups shield the hydrophobic core from the surrounding solvent.

phase occurs. Equating the expressions for E_{pen} and S_{gas} and solving for ρ yields directly the density ρ^* at which aggregation starts to dominate

$$\rho^* = C \lambda^{-3} \cdot e^{-E_{pen}/k_B T} \quad (2.3)$$

This result is reasonable since it predicts that the critical density decreases as the energy penalty increases.

2.1.2 Mathematical description of membranes

To characterize lipid membranes, one usually describes them as a thin, elastic surfaces (two-dimensional manifolds) that are described by using tools of differential geometry. To be more specific, a membrane is interpreted as a two-dimensional surface embedded in three-dimensional space. This is of course a simplification since the surface is assumed to be infinitely thin, which is not true for real membranes. However, results originating from this simple model extremely well agree with experimental observations.

The general formula for a two-dimensional hyperplane \mathbf{S} is given by

$$\mathbf{S}(\mathbf{r}) = \begin{pmatrix} f_1(\mathbf{r}) \\ f_2(\mathbf{r}) \\ f_3(\mathbf{r}) \end{pmatrix} \quad (2.4)$$

The analytical treatment of a surface is coupled to the choice of coordinates and representation. One possible approach is to use a set of basis vectors that are embedded in the surface itself. This is similar to describe a one-dimensional trajectory by its arc length s .

A simple and common way to describe membranes is to use Cartesian coordinates. That means, the membrane is characterized as a height field h over the underlying

xy plane. Consequently, the surface \mathbf{S} is represented by

$$\mathbf{S} = (x, y, h(x, y)) \quad (2.5)$$

In general, $h(x, y)$ can adopt multiple values at a given point in the xy plane. That means, the surface can posses an overhang at this point. A common way to resolve this obstacle is to interpret the surface in the so-called *Monge* representation: $h(x, y)$ is restricted to be single-valued at every point thus preventing overlap regions.

Based on Equation 2.5, it is now straightforward to determine basic entities like tangential (\mathbf{t}) and normal (\mathbf{n}) vectors in a given point p of the surface \mathbf{S}

$$\mathbf{t}_x = \partial_x \mathbf{S} = (1, 0, \partial_x h) \quad (2.6)$$

$$\mathbf{t}_y = \partial_y \mathbf{S} = (0, 1, \partial_y h) \quad (2.7)$$

$$\mathbf{n} = \frac{\mathbf{t}_x \times \mathbf{t}_y}{|\mathbf{t}_x \times \mathbf{t}_y|} = (-\partial_x h, -\partial_y h, 1)/\sqrt{g} \quad (2.8)$$

Here, the factor g is the metric of the surface. The metric of a surface describes how to measure distances and angles on the surface. In the present case, g is given by

$$g = 1 + (\partial_x h)^2 + (\partial_y h)^2 \quad (2.9)$$

The local shape of the surface in every point p is characterized by two principal curvatures, κ_1 and κ_2 . They can be determined by constructing the osculating circles with minimal and maximal radius in point p . Two important quantities derived from κ_1 and κ_2 are the mean and Gaussian curvature, H and K , respectively.

$$H = \frac{1}{2}(\kappa_1 + \kappa_2) \quad \left[\frac{1}{length} \right] \quad \text{and} \quad K = \kappa_1 \cdot \kappa_2 \quad \left[\frac{1}{length^2} \right] \quad (2.10)$$

They are very important entities when the energy functional governing the dynamics of the membrane is considered. We address this point later. The assumption of small curvatures further simplifies the expressions for the mean and Gaussian curvature (Schwarz09)

$$|\partial_{x,y} h| \ll 1 \quad \Rightarrow \quad H = \frac{1}{2} (\partial_x^2 h + \partial_y^2 h) \quad , \quad K = \partial_x^2 h \cdot \partial_y^2 h - (\partial_{xy}^2 h)^2 \quad (2.11)$$

The Monge gauge allows to establish results applicable at long length scales that do not exceed the persistence length ξ_p of the surface. The latter quantity is a measure for the distance over which the surface's normal vectors become decorrelated. According to (Peliti85), the persistence length of a surface is given by

$$\xi_p = b \cdot \exp(4\pi\kappa_b/3k_B T)$$

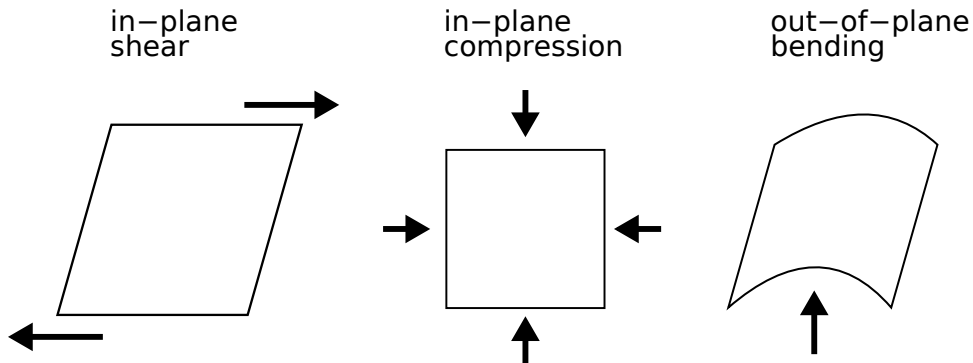


Figure 2.3: *Three fundamental kinds of elastic deformations: shearing, compressing and bending.*

with b being an intrinsic length scale of the surface and κ_b the corresponding bending rigidity of the surface. Setting $b \approx 1\text{nm}$ and $\kappa_b \approx 10k_B T$, one obtains $\xi_p \approx 10^6\text{km}$. This astronomical length does not imply that membranes are planar, they rather undulate smoothly on cellular length scales.

2.1.3 Mechanical properties of membranes

Belonging to the class of soft condensed matter, membranes are subject to different kinds of deformations. According to elasticity theory, there are three fundamental deformations that can be applied to thin films like membranes, namely in-plane shear, in-plane compression and out-of-plane bending. Sketches of these are depicted in Figure 2.3. How and at which expense do these deformations change the conformation of a lipid bilayer?

Broadly speaking, a lipid bilayer can exist in a fluid or solid (also ‘gel’) phase depending on temperature. In the fluid phase, lipids are able to diffuse freely within their membrane leaflet while in the gel-like phase their motility is extremely restricted. Thus, a shear stress applied to a lipid bilayer in the fluid phase has only a marginal effect on its conformation.

Regarding in-plane compression, one has to distinguish between different tension regimes. At zero tension, thermal membrane fluctuations are conserved while applying a small tension leads to a flattening of the membrane, i.e. fluctuations are suppressed. Increasing the tension further results in a stretching of the membrane area that becomes more and more expensive in terms of energy. Thus, a moderate lateral tension does not change the membrane conformation in terms of average area per lipid.

The last deformation mode, out-of-plane bending, is the most important one.

Since the bending modulus (κ_b) of a lipid bilayer is of the order of $10k_B T$, it is relatively easy to curve a membrane. In the following, we restrict our discussion to fluid and incompressible bilayers, i.e. only elastic bending deformations contribute to structural changes of the bilayer.

The Helfrich Hamiltonian

The simplest expression for the energy density of elastic bending deformations involves the mean and Gaussian curvatures. The corresponding Hamiltonian \mathcal{H}_H coined by Helfrich (Helfrich73) reads

$$\mathcal{H}_H = \int_{\mathcal{A}} \left[\frac{\kappa_b}{2} (2H - C_0)^2 + \kappa_G K \right] d\mathcal{A} \quad (2.12)$$

The parameters κ_b and κ_G within this formula are the bending rigidity and the Gaussian bending rigidity, respectively. Furthermore, C_0 is the spontaneous curvature, i.e. the curvature a membrane would adopt in equilibrium. A non-zero spontaneous curvature can be due to, for example, a different lipid composition of the two opposing leaflets. For our purposes, we set C_0 equal to zero. One property of the Gaussian curvature facilitates this bending-energetical treatment. Due to the Gauss-Bonnet theorem (Weinstein09), the integral over the surface involving the Gaussian curvature remains unchanged as long as the topology of the surface is fixed, which is definitely the case for flat biological membranes. Here, we have to remark that vesiculation processes alter the topology of the membrane requiring now the incorporation of the Gaussian curvature term.

Membrane undulations

For the following consideration, we investigate a membrane to which a tension τ is applied. Its energy E is then given by

$$E = \tau \int d\mathcal{A} + 2\kappa_b \int H^2 d\mathcal{A} \quad (2.13)$$

where we assume that the topology of the membrane does not change and hence the contribution of the Gaussian curvature term vanishes. Inserting the expression for the mean curvature derived in the Monge gauge (cf. Equation 2.11), applying the Fourier representation (\mathbf{q} space) of the height function $h(x, y)$ and subsequent integration yields

$$E = \frac{1}{2} \frac{\mathcal{A}^2}{4\pi^2} \int (\tau q^2 + \kappa_b q^4) h(\mathbf{q}) h^*(\mathbf{q}) d\mathbf{q} \quad (2.14)$$

To find the thermal expectation value $\langle h(\mathbf{q}) \cdot h^*(\mathbf{q}) \rangle$ one uses the equipartition theorem. Equation 2.14 can be regarded as a generalization of the harmonic oscillator. Assigning each mode in \mathbf{q} space an average energy of $k_B T/2$ directly results in

$$\langle h(\mathbf{q}) \cdot h^*(\mathbf{q}) \rangle = \frac{k_B T}{\mathcal{A}} \cdot \frac{1}{\tau q^2 + \kappa_b q^4} \quad (2.15)$$

demonstrating that the thermal average in Fourier space increases with temperature. In the thermodynamic limit, i.e. fluctuations of infinitely large, nearly flat membranes, surface tension effects can be neglected since the applied tension has no effect on the lateral size. Thus, one can set $\tau = 0$ which further simplifies Equation 2.15.

2.2 Polymers

Aside from membranes, polymers make up the second broad category of structural components of cells. We concentrate here on linear polymers constructed from individual monomeric units that may not be identical. The aim of this section is to introduce basic concepts in polymer physics. We first summarize static properties for ideal and real polymer chains. A short overview of dynamical aspects completes the section.

2.2.1 Static properties of polymers

We now derive static properties of ideal polymers. Our calculations in this section are based on the freely-jointed chain model which is the simplest model to describe a polymer. Here, a polymer is regarded as a random walk and interactions among individual monomers are neglected. In addition, the individual monomers are considered point-like, i.e. steric effects are not taken into account. Despite its simplicity, it is a useful tool to gain insight into polymer physics.

Ideal polymer chains

Consider a flexible polymer consisting of $N + 1$ monomers. A conformation can be identified by the set of $N + 1$ position vectors \mathbf{R}_i ($i = 0, \dots, N$), or by the set of bond vectors $\mathbf{r}_i = \mathbf{R}_i - \mathbf{R}_{i-1}$ ($i = 1, \dots, N$). The latter set represents an ensemble of independent connection vectors.

The end-to-end vector A first entity related to the size of a polymer is its *end-to-end vector* \mathbf{R}_{ee} that is defined as

$$\mathbf{R}_{ee} = \sum_{i=1}^N \mathbf{r}_i = \mathbf{R}_N - \mathbf{R}_0 \quad (2.16)$$

Since there is no preferred direction, the average value of the end-to-end vector vanishes: $\langle \mathbf{R}_{ee} \rangle = 0$. The simplest non-zero average is the mean-square end-to-end vector

$$\langle \mathbf{R}_{ee}^2 \rangle = \sum_{i=1}^N \sum_{j=1}^N \langle \mathbf{r}_i \cdot \mathbf{r}_j \rangle \quad (2.17)$$

Assuming all bond vectors having the same length b , the last formula can be expressed as

$$\langle \mathbf{R}_{ee}^2 \rangle = b^2 \sum_{i=1}^N \sum_{j=1}^N \langle \cos(\theta_{ij}) \rangle = N \cdot b^2 \quad (2.18)$$

where we take into account that directions between different bond vectors are uncorrelated. The last equation reveals that the mean-square end-to-end vector is directly proportional to the number of monomer bonds: $\langle \mathbf{R}_{ee}^2 \rangle \propto N$. Although we used a very simple model to derive this relation, the dependence of \mathbf{R}_{ee} on N is very general (Doi01).

To conclude this paragraph, we provide an expression for the distribution of end-to-end vectors. The projection of the configuration of a polymer chain onto the individual coordinate axes reduces the initial problem to determine separate one-dimensional distributions. For example the x -component of the end-to-end vector is just the sum of the individual monomer vectors projected onto the x -axis

$$X_{ee} = \sum_i X_i \quad (2.19)$$

Since the single components X_i are independent of each other, the projections form a random walk in one dimension. If the number of segments is large, one can apply the central limit theorem that states that the corresponding length distribution has to adopt a Gaussian form. Following this approach in every other direction and combination of the individual results yields the distribution of end-to-end vectors that is also Gaussian

$$P(\mathbf{R}_{ee}, N) = \left(\frac{3}{2\pi N b^2} \right)^{\frac{3}{2}} \exp \left(-\frac{3\mathbf{R}_{ee}^2}{2N b^2} \right) \quad (2.20)$$

However, this well-known formula exhibits a small taint which is the occurrence of values of $|\mathbf{R}_{ee}|$ being larger than the maximal extended length $N \cdot b$. A more

realistic model is available in the literature (Flory69). The above mentioned similarity between polymer chains and random walks is applied frequently to illustrate the behaviour of polymers and to solve problems in polymer science.

The radius of gyration The mean-square end-to-end vector is a suitable measure for the size of a linear polymer. Unfortunately, branched or ring polymers can not appropriately be described by this quantity. A more convenient quantity is the *radius of gyration* R_g that measures the dimension of the polymer relative to its center of mass. It is given by

$$R_g^2 = \frac{1}{N} \sum_{i=1}^N (\mathbf{R}_i - \mathbf{R}_{CM})^2 \quad \text{with} \quad \mathbf{R}_{CM} = \frac{1}{N} \sum_{j=1}^N \mathbf{R}_j \quad (2.21)$$

where we assume in the second term all monomers having the same mass. As before, the square radius of gyration is usually averaged over the ensemble of allowed conformations resulting in the mean-square radius of gyration

$$\langle R_g^2 \rangle = \frac{1}{N^2} \sum_{i=1}^N \sum_{j=1}^N \langle (\mathbf{R}_i - \mathbf{R}_j)^2 \rangle \quad (2.22)$$

Equation 2.22 was obtained by merging the two expressions given in Equation 2.21 and subsequent rearrangement.

For a linear, ideal polymer chain, the square radius of gyration can be easily calculated. The discrete sums are converted into integrals over the contour of the polymer. After a few lines of calculation one arrives at the following expression for $\langle R_g^2 \rangle$

$$\langle R_g^2 \rangle = \frac{b^2 N}{6} = \frac{\mathbf{R}_{ee}^2}{6} \quad (2.23)$$

Thus, the mean-square radius of gyration of an ideal, linear polymer obeys the same scaling behaviour as its mean-square end-to-end vector $\langle \mathbf{R}_{ee}^2 \rangle$. The calculation of $\langle R_g^2 \rangle$ for other polymer shapes, e.g. branched or rod polymers, can be done accordingly. Rubinstein et al. give results for these polymer types (Rubinstein06).

Real polymer chains

In the last section, conformations of ideal chains were discussed. We now take into account interactions between monomers that are separated by many bond lengths along the polymer chain. In particular, we discuss alterations in the statistical properties if steric interactions are considered, i.e. the polymer consists of monomers with a finite lateral dimension. To keep things simple we restrict our analysis to spherical monomers.

solvent	good	θ	poor
ν	0.588	1/2	1/3

Table 2.1: *The scaling exponent ν connected to the polymer size R varies with solvent quality. A decreasing solvent quality yields the reduction of the scaling exponent from $\nu \approx 3/5$ to $\nu = 1/3$.*

Excluded volume effect One key result of the last section was that an ideal polymer can be interpreted as a random walk, i.e. every polymer segment is independent from all others. However, prohibiting a pair of monomers to occupy the same spatial location directly leads to correlations between the monomers. Following this line, a real polymer chain can consequently be characterized as a self-avoiding random walk, i.e. a random walk that does not visit the same point more than once.

A detailed analysis of real polymer chains was carried out by Flory (Flory49). Flory calculated configurations of real polymers based on the idea that their size is governed by two competing interactions. On the one hand, steric repulsion is responsible for polymer swelling. On the other hand, chain connectivity creates an attraction counteracting monomer departure. Flory combined both interactions and derived a single parameter, ν , which summarizes the net interaction between monomers. According to (Rubinstein06), ν also characterizes the quality of solvent the polymer is floating in: athermal, good, θ , poor and non-solvent.

An important result from Flory's theory for a polymer in good solvent is that it yields an universal power-law dependence of polymer size R on the number of monomers N , i.e.

$$R^2 \propto N^{2\nu} \quad \text{with} \quad \nu = \frac{3}{2+d} \quad (2.24)$$

In contrast to ideal chains, the scaling behaviour of the polymer size now exhibits a dependence on the dimension of space d in which the polymer resides. Compared to ideal linear polymers where $\nu = 1/2$, Flory concluded the scaling exponent for real chains to be $\nu = 3/5$. Subsequent perturbative approaches found the more accurate value of $\nu = 0.588$ (Doi01).

In a poor solvent environment, polymers change their shape drastically. Attractions between monomers now dominate resulting in the collapse of the polymer into the so-called *molten globule* state. Poor solvent conditions also lead to a decrease in the scaling factor which has a lower bound at $\nu = 1/3$ (Rubinstein06). Interesting is also the case of a θ solvent. Here, attraction and repulsion exactly balance each other. As a consequence $\nu = 0$, meaning that polymer chains have nearly ideal conformation. The corresponding scaling exponent thus adopts the value $\nu = 1/2$. Table 2.1 summarizes the possible different values of the scaling exponent ν .

2.2.2 Polymer dynamics

During the last section we saw that scaling concepts play an important role in determining static properties of polymers. Indeed, these concept are also frequently encountered when the dynamical behaviour of polymers is discussed. We are now going to present two different models for polymer dynamics namely the Rouse (Rouse53) and the Zimm model (Zimm56).

The Rouse model

In the Rouse model monomers connected by springs set up the polymer chain. The average distance between two consecutive monomers is taken to be b , i.e. the root-mean-square bond length. Interaction between monomers is exerted only by the connecting springs. Excluded volume and hydrodynamic interactions with the surrounding solvent are disregarded.

The motion of a Rouse chain can be described by a Langevin equation which determines the time evolution of the individual monomer positions. Assuming a harmonic form of the interaction potential yields

$$\zeta \frac{d\mathbf{R}_i}{dt} = -k \cdot (2\mathbf{R}_i - \mathbf{R}_{i+1} - \mathbf{R}_{i-1}) + \mathbf{f}_i \quad i = 2, \dots, N-1 \quad (2.25)$$

where ζ is the monomer's friction coefficient, k the amplitude of the harmonic force and \mathbf{f}_i a random force with Gaussian statistics. Care must be taken for the first and last monomer

$$\zeta \frac{d\mathbf{R}_1}{dt} = -k \cdot (\mathbf{R}_1 - \mathbf{R}_2) + \mathbf{f}_1 \quad (2.26)$$

$$\zeta \frac{d\mathbf{R}_N}{dt} = -k \cdot (\mathbf{R}_N - \mathbf{R}_{N-1}) + \mathbf{f}_N$$

Two key quantities connected to the dynamical behaviour are the diffusion coefficient of the polymer's center of mass, D_{cm} , and the relaxation time of the polymer chain, τ_R . Following (Rubinstein06), these two parameters exhibit a distinct scaling dependence on the number of monomers N

$$D_{cm} \propto N^{-1} \quad \text{and} \quad \tau_R \propto N^{1+2\nu} \quad (2.27)$$

It is known that the first scaling relation holds in two and three dimensions (Doi01) whereas the second relation is only true in three dimensions. The parameter ν corresponds to Flory's exponent describing the polymer size (see above). However, these values do not coincide with experimental results. This is mainly due to the neglect of hydrodynamic interactions. Nevertheless, the Rouse model is a suitable approach when inspecting dynamics of polymer melts.

model	D_{cm}	τ
Rouse	N^{-1}	$N^{1+2\nu}$
Zimm	$N^{-\nu}$	$N^{3\nu}$

Table 2.2: 3D-scaling behaviour of center of mass diffusion coefficient D_{cm} and relaxation time τ on polymer size for Rouse and Zimm model. The factor ν denotes the Flory exponent of the polymer's radius of gyration.

The Zimm model

The Zimm model explicitly takes into account interactions related to hydrodynamics. A particle moving in a fluid couples to the surrounding solvent and has to drag solvent molecules in order to move. This viscous resistance leads to a long-ranged force. The treatment of Zimm polymers can again be done in form of a Langevin equation that now reads

$$\frac{d\mathbf{R}_n}{dt} = \sum_m \mathbf{H}_{nm} \cdot \left(k \frac{\partial^2 \mathbf{R}_m}{\partial m^2} + \mathbf{f}_m(t) \right) \quad (2.28)$$

Here, monomer bonds are assumed to be realized via harmonic potentials, the random force \mathbf{f} is Gaussian and \mathbf{H}_{nm} is the Oseen or mobility tensor (Doi01). The qualitative difference compared to Rouse polymers is that here interactions between monomers are not local.

The basic approach of the Zimm model is to regard a polymer chain as a solid object of size $R \propto N^\nu$ that moves through the solvent. The scaling of the center of mass diffusion coefficient D_{cm} can be easily determined by employing Stoke's law and the Einstein-Stokes equation. The scaling behaviour of the corresponding relaxation time τ_Z is then immediately derived.

$$D_{cm} \propto N^{-\nu} \quad \text{and} \quad \tau_Z \propto N^{3\nu} \quad (2.29)$$

It is worthwhile noting that τ_Z exhibits a weaker dependence on the polymer size than τ_R since for $\nu < 1$ the relation $3\nu < 2\nu + 1$ applies. This means that Zimm motion has less frictional resistance than Rouse motion, and therefore Zimm motion is the faster process.

To conclude this section about polymers, we recapitulate in Table 2.2 the key results concerning polymer dynamics obtained by the Rouse and Zimm model.

2.3 Proteins

Apart from water, proteins are the main constituents in living cells representing approximately 50% of a cell's dry mass (Alberts02). They are made of amino acids that are, besides lipids, nucleotides and monosaccharides, the fundamental

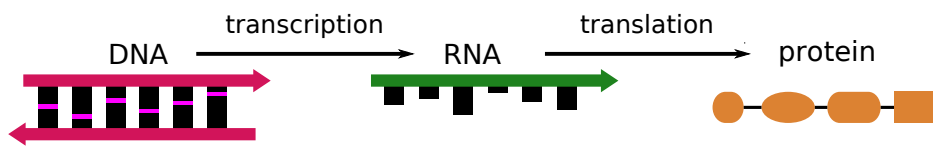


Figure 2.4: From DNA to protein: transcription copies DNA into RNA, translation converts RNA into amino acids. Every organism synthesizes its proteins according to this general pathway.

molecules of cells. Connected to the former section, proteins can be seen as polymers consisting of peptides that adopt a distinct three-dimensional shape. Here, we sketch briefly protein synthesis and discuss how transmembrane proteins are distributed throughout the cell.

2.3.1 Protein synthesis

Information which proteins eukaryotic cells can produce is hidden in their hereditary material in form of DNA. In order to produce new proteins, this information has first to be converted into RNA that is another kind of genetic information. The difference to DNA is that RNA consists of different nucleotide base pairs. The process of DNA-RNA conversion is called *transcription* and is carried out by numerous macromolecules and regulation factors (Kornberg07).

The resulting piece of RNA is further manipulated, one can say that it is kind of purged. Fragments unnecessary for protein synthesis are dumped and the remainder is called *messenger RNA* (mRNA). These molecules contain the chemical blueprint for proteins. In order to generate a functional protein, mRNA is brought to a giant molecular machine called *ribosome* (Frank00). Here, its nucleotide sequence is *translated* into a linear amino acid sequence representing a protein's native state.

To become a fully and properly functional protein, the linear chain has to fold up into a distinct three-dimensional structure that is determined by its amino acid sequence. Auxiliary proteins called *molecular chaperones* (Hartl96) assist the folding process and also provide an efficient quality control machinery. Figure 2.4 depicts the above described general route of protein synthesis.

Transmembrane proteins

In eukaryotic cells, transmembrane proteins represent a huge family of intracellular macromolecules. Nearly 30% of all encoded proteins are transmembrane proteins. Most of these are directly synthesized at the membrane of the rough endoplasmic reticulum (ER). Their particular spatial location inside lipid bilayers enables them

to perform a variety of tasks as different as signal and mass transfer across the membrane barrier, induction of structural changes of the surrounding lipid bilayer and regulatory functions.

Given the characteristic topology of transmembrane proteins, the question arises of how insertion, integration and folding of transmembrane segments within the ER membrane is realized. The main actor during this process is the *translocon*, an elaborate protein complex that is responsible for proper transmembrane protein integration (Rapoport07). Its principle is as follows: a nascent amino acid chain enters a narrow tunnel provided by the translocon and is successively transported across the membrane barrier. Inside the tunnel transmembrane segments are recognized and led through a central gate into the membrane.

2.3.2 Sorting of transmembrane proteins

The distribution of transmembrane proteins throughout the cell occurs along the secretory pathway. One can imagine that pathway originating at the endoplasmic reticulum. Further downstream, proteins have to pass through the Golgi apparatus. From there, different routes lead to the plasma membrane and the cell exterior, or to endosomes and lysosomes (see Figure 2.5).

Shuttling of intracellular cargo, i.e. proteins, enzymes or lipids, is organized by vesicular transport intermediates, small spherical membrane-bound containers. As a general rule, one can say that different kind of vesicles use different routes of the secretory pathway. The various types of vesicles are distinguished by their protein envelope, a so-called coat. Transport between ER and Golgi and in between the latter occurs by means of COP-coated vesicles. Post-Golgi traffic is mediated by clathrin-coated vesicles. Figure 2.5 provides a simplified overview of the different vesicle types and their preferred transport direction.

The secretory pathway possesses an anterograde (forward) and retrograde (backward) direction. We restrict ourselves here to the description of the passage between endoplasmic reticulum and the Golgi apparatus, i.e. the early secretory pathway.

The early secretory pathway

Like the ER, the Golgi apparatus is not a clearly confined organelle. It is rather a stack of flat membrane-bound compartments, so-called Golgi cisternae. On either end of this stack are several loose vesicular and tubular structures that are termed the cis- and trans-Golgi network depending on their position with respect to the nucleus. Accordingly, the Golgi complex is divided into a cis-, a medial- and a trans-Golgi part.

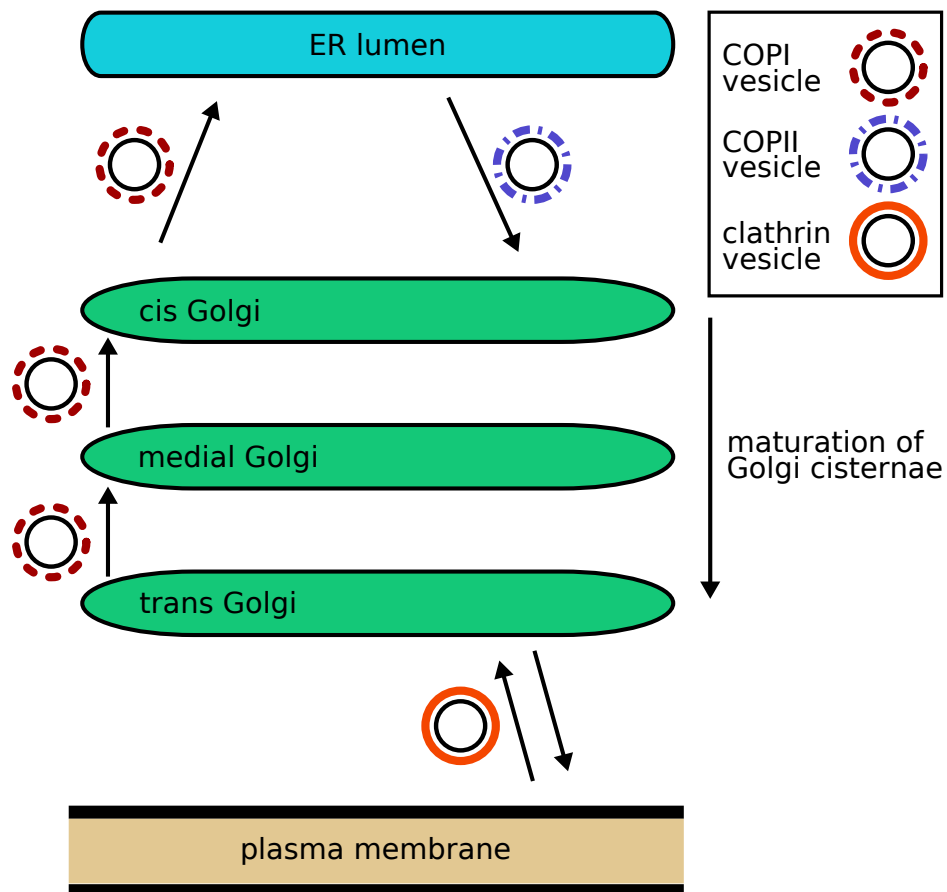


Figure 2.5: Sketch of vesicular transport along the secretory pathway: COP-coated transport vesicles are responsible for shuttling cargo between the endoplasmic reticulum and the Golgi apparatus as well as between different Golgi cisternae. Export from the Golgi and import from the cell exterior occurs via clathrin-coated vesicles. In addition to vesicular transport, Golgi cisternae can mature and influence in this way the distribution of membrane proteins.

Membranes, Polymers & Proteins

Along the Golgi stacks, proteins and other macromolecules are modified, sorted and prepared for further transport to intra- or extracellular destinations. Furthermore, it plays a role in transport of lipids and the creation of lysosomes.

ER-to-Golgi transport

Transmembrane proteins residing in the ER membrane are exported towards the Golgi apparatus by COPII coated vesicles. They are exclusively formed at special locations of the endoplasmic reticulum membrane which are termed ER exit sites (ERES). ER exit sites are speckled all over the ER membrane and show a distinct spatial and temporal self-organization (Heinzer08). Interestingly, ERES vanish during cell division indicating a transient stop of secretory traffic.

The COPII coat consists of three essential sub-units that are Sar1p, Sec23/24p and Sec13/31p (Barlowe94). Formation of COPII vesicles takes place as follows: floating freely in the cytosol, Sar1p is attracted to the ER membrane and subsequently recruits the two remaining sub-units, Sec23/24p and Sec13/31p. Recently, it was shown that secretory cargo, e.g. transmembrane proteins, slows down the disassembly of the COPII coat complex (Forster06). This is very important since an intact coat complex is required for proper transport vesicle formation, premature coat disassembly would complicate or even prevent the generation of transport carriers.

Membrane-bound Sar1p and Sec13/31p most likely bend the ER membrane in order to stimulate the vesiculation process. In addition, these two sub-units are also believed to trigger the fission event, i.e. to detach the transport vesicle from the ER membrane (Lee05; Stagg06). A typical COPII vesicle has a diameter of roughly 60nm and accommodates right after fission roughly 50 COPII complexes (Stagg06). After detachment from an ER exit site, the coat proteins dissociate from the vesicle due to GTP hydrolysis by Sar1. The 'naked' vesicles are now actively transported towards the Golgi apparatus while the coat subunits stay in the cytosol and can be used in another round of vesicle formation.

Intra-Golgi transport

It is still not completely understood how molecules move from one Golgi cisterna to another. At present, there are two models of cargo transport across the Golgi apparatus that are either based on vesicular transport or assume maturation of Golgi cisternae (Alberts02; Lodish04). Recent experimental studies support the opinion that both hypotheses work in conjunction rather than being mutually exclusive (Glick98; Pelham00; Glick00).

The observation of abundant vesicular transport containers in the vicinity of the Golgi complex created the idea that these vesicles are responsible for shuttling

molecules between the distinct Golgi compartments. They bud from one cisterna and fuse with the next. In contrast to vesicles departing from the ER membrane, their formation is stimulated by a different type of protein coat called COPI. Like COPII, it also consists of several subunits that have to act in concert in order to achieve full functionality.

Another function of COPI vesicles is to retrieve mislocalized proteins and to transport them back to their correct compartment. Furthermore, COPI proteins are also involved in retrograde transport from the Golgi complex to the ER. The combination of backward and forward vesicular flux also guarantees the conservation of the polarized structure of the Golgi apparatus.

According to the cisternal maturation model, the Golgi complex is a dynamic structure that undergoes permanent alterations. In this picture, tubular clusters originating from the ER fuse with each other to form a first cisterna and progressively mature as they move through the Golgi stack. That means, at the cis face of the Golgi, new cis cisternae are constantly formed and then migrate through the stack as they mature. Proteins associated with the different cisternae consequently travel along the Golgi complex as well. To maintain the differential distribution of Golgi proteins, retrograde transport by COPI vesicles again re-distributes mislocalized proteins.

Chapter 3

Membrane Simulations via Dissipative Particle Dynamics

Biological membranes, or lipid bilayers, are the defining envelope of living cells and their internal organelles separating them from their external environments. Far from being inert, membranes accomodate a plethora of transmembrane proteins that are responsible for signal and mass transfer across this boundary (Alberts02; Lodish04). For this reason, it is no surprise that the study of biological membranes has attracted much attention during the last decades.

The number of approaches used to gain insight into the nature of membranes is steadily increasing. These range from biochemical *in vivo* assays and studies on model membranes *in vitro* over sophisticated light and electron microscopy techniques to powerful computer simulations.

The present chapter deals with the latter approach, i.e. an *in silico* investigation of biological membranes. In particular, a coarse-grained molecular dynamics (MD) simulation technique called *dissipative particle dynamics* (DPD) is introduced as a suitable method to study soft matter systems like lipid bilayers.

3.1 Dissipative particle dynamics

The study of subcellular, dynamical processes involves the application of elaborate microscopy techniques. However, structures beyond the diffraction limit of light can not be resolved and a thorough (dynamical) description is impossible. At this point, computer simulations lend themselves as a powerful and versatile tool.

Among the numerous different simulation methods, molecular dynamics is the most accurate one. Here, every single atom of the system of interest is modelled including all possible interactions, be it non-geometrical (van der Waals, electrostatic) or geometrical (bonds, angles) interactions (Thijssen99). However, this

Membrane Simulations

beautiful and precise description has a nasty side effect which is manifested in its enormous need for computational resources. Hence, MD simulations are limited in length and time to the nanoscale. Despite the computational drawback full-atomistic simulations of simple model membranes and membrane-protein systems have been performed (Pasenkiewicz99; Essmann99).

In this work, dissipative particle dynamics, a coarse-grained MD simulation technique was used to study biological systems. The main advantage of DPD compared to MD is that longer time and length scales are accessible. In principal, spatial dimensions of $\mathcal{O}(100\text{ nm})$ and time scales in the microsecond range can be accessed.

3.1.1 From hydrodynamics to soft matter systems

In 1992, Hoogerbrugge and Koelman developed a new simulation method they termed dissipative particle dynamics to investigate hydrodynamic phenomena (Hoogerbrugge92). Their aim was to be able to model correct hydrodynamic behaviour with computational efficiency. For this purpose, they did not model individual atoms but rather simulated the motion of small fluid elements representing a functional group of atoms. Thus, a DPD bead has a mesoscopic character, i.e. it is large on the atomic scale but small compared to the overall dimensions of the system. The basic interactions in a DPD system are chosen in such a way that the system reproduces correctly hydrodynamic properties. DPD satisfies, for example, the Navier-Stokes equation (Hoogerbrugge92).

Soon after its introduction, Español and Warren (Español93) developed a thorough theoretical description of DPD with the result that the statistical mechanics of the DPD bead ensemble was now in agreement with that of the canonical ensemble. At present, the formulation of Español and Warren is the most frequently used implementation of DPD.

In their description, three pairwise-additive forces act between the soft DPD beads; these are a conservative, repulsive force \mathbf{F}^C , a dissipative force \mathbf{F}^D and a random force \mathbf{F}^R . They conserve linear and angular momentum, have no hard core and vanish beyond a certain cut-off radius r_c that in turn also defines the dimension of a single DPD bead.

Complex quantities like polymers, lipids or proteins are realized by joining DPD particles via simple Hookean springs. A bending potential accounts for the rigidity of these objects. DPD was successfully applied to colloid systems, lipid bilayers and micellar systems (Flekkøy99; Yamamoto02; Shilcock02; Laradji04; Venturoli05).

Compared to full-atomistic MD simulations, DPD simulations are able to span much larger length and time scales. This results, on the one hand, from the mesoscopic character of a DPD system that conceals molecular details on the

microscopic level. On the other hand, the choice of soft-core potentials allows the use of a larger time integration step Δt compared to Lennard-Jones potentials usually used in MD simulations.

Fundamentals of DPD

Like in classical MD simulations, DPD particles interact with each other, and the motion of a single particle is described by Newton's equations of motion

$$\dot{\mathbf{x}}_i = \mathbf{v}_i \quad \text{and} \quad \dot{\mathbf{p}}_i = \mathbf{F}_i \quad (3.1)$$

As mentioned before, the total force \mathbf{F}_i acting on a single DPD bead has three different parts yielding the following expression

$$\mathbf{F}_i = \sum_{j \neq i} (\mathbf{F}_{ij}^C + \mathbf{F}_{ij}^D + \mathbf{F}_{ij}^R) \quad (3.2)$$

All particles j that are inside the cut-off radius r_c around particle i contribute to the above sum. The cut-off radius represents the size of a DPD bead and is usually set to unity: $r_c = 1$.

Friction and heat: the thermostat One important point during a DPD simulation is the preservation of the temperature of the system. This is usually achieved by introducing a fluctuation-dissipation theorem (Nyquist28; Callen51), a powerful tool that links the fluctuation properties of a thermodynamic system to its linear response properties.

Following Español and Warren, this task can be done by coupling the dissipation and random force that read

$$\mathbf{F}_{ij}^D = -\gamma \omega^D(\mathbf{r}_{ij}) \cdot (\mathbf{e}_{ij} \cdot \mathbf{v}_{ij}) \mathbf{e}_{ij} \quad (3.3)$$

$$\mathbf{F}_{ij}^R = \sigma \omega^R(\mathbf{r}_{ij}) \xi_{ij} \mathbf{e}_{ij} \quad (3.4)$$

where \mathbf{r}_{ij} denotes the connection vector, \mathbf{e}_{ij} the corresponding unit vector and \mathbf{v}_{ij} the relative velocity of the bead pair i and j . The parameters γ and σ are the amplitudes of the dissipative and random force, respectively. The definition of \mathbf{F}^R includes a symmetric random variable ξ_{ij} with zero mean and unit variance, uncorrelated for different pairs of particles at different times, that is

$$\langle \xi_{ij}(t) \xi_{i'j'}(t') \rangle = (\delta_{ii'} \delta_{jj'} + \delta_{ij'} \delta_{ji'}) \delta(t - t') \quad (3.5)$$

Two different weight functions, ω^D and ω^R , complete the definition. Originally, the random numbers ξ_{ij} were supposed to be drawn from a Gaussian distribution.

Membrane Simulations

However, it has proven appropriate and computationally efficient to use a uniform distribution instead (Nikunen03).

The dissipative force is the result of friction between hidden internal degrees of freedom of the DPD particles. This energy loss is balanced by the random force which is interpreted as the coupling of the DPD beads to their local thermal environment. As pointed out before, these two forces have to act in concert in order to guarantee a stable, only slightly fluctuating temperature of the system. To realize the fluctuation-dissipation theorem, the amplitudes as well as the weight functions are connected via the following relations (Español93)

$$\sigma^2 = 2\gamma k_B T \quad \text{and} \quad \omega^D(r) = (\omega^R(r))^2 \quad (3.6)$$

As a consequence, one amplitude and one weight function can be chosen arbitrarily. Following (Nikunen03), we choose

$$\omega^R(r) = \omega(r) = \begin{cases} (1 - r/r_c) & \text{for } 0 \leq r \leq r_c \\ 0 & \text{else} \end{cases} \quad (3.7)$$

Common numerical values for the amplitudes of the dissipative and the random force are $\gamma = 4.5$ and $\sigma = 3$. For convenience, the thermal energy is also set to unity: $k_B T = 1$. These restrictions guarantee that the DPD system matches the definition of the Gibbs canonical ensemble. Advantages of this fact are that all basic thermodynamic relations hold and can readily be translated into the DPD formalism.

Since \mathbf{F}^D and \mathbf{F}^R both act along the connection vector between two interacting beads, the linear as well as the angular momentum is conserved. A measure for the system's temperature is the average kinetic temperature that is defined via

$$\langle k_B T \rangle = \frac{m}{3N} \sum_i \mathbf{v}_i^2$$

where N is the total number of particles and m their mass. This quantity fluctuates around the initially specified value of $k_B T = 1$, the speeds of the DPD particles follow a Maxwell-Boltzmann distribution (cf. Figure 3.1, right).

The repulsive force The repulsive force accounts for basic steric interactions and is given by

$$\mathbf{F}_{ij}^C = \mathcal{A}_{ij} \omega(r) \cdot \mathbf{e}_{ij} \quad (3.8)$$

The constant \mathcal{A}_{ij} defines how strong the particles i and j repel each other. The weight function $\omega(r)$ is the same as in Eq. 3.7, i.e. \mathbf{F}^C is of linear form which is computationally very stable and efficient. Again, the repulsive force acts along the connection between two beads, conserving thus linear and angular

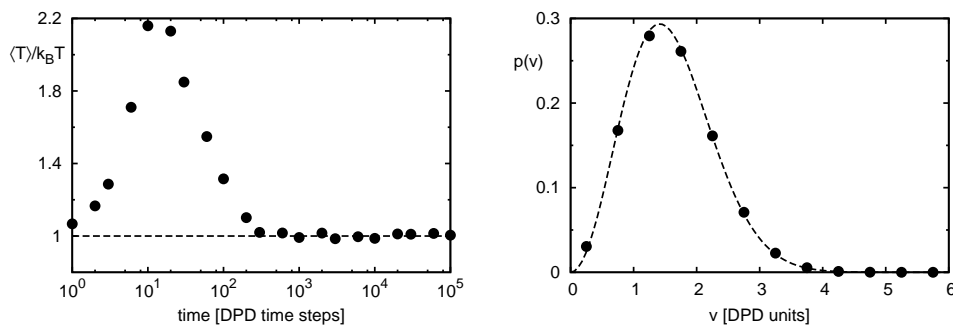


Figure 3.1: *Left: after a short period of equilibration, the average kinetic temperature fluctuates around the initially fixed value of $k_B T$ (Note the logarithmic scale in time). Right: The distribution of speeds of the DPD particles (filled circles) corresponds to a Maxwell-Boltzmann distribution (dashed line).*

momentum. Since all forces are pairwise, the relation $\mathbf{F}_{ij}^* = -\mathbf{F}_{ji}^*$ is true for the repulsive, dissipative and random force.

Apart from determining the repulsion between two DPD particles, the parameter \mathcal{A} can be used to realize different types of DPD beads. We will return to that property in the section on membranes.

To simulate water, one usually sets $\mathcal{A} = 25k_B T$. Together with a DPD bead density of $\rho = 3/r_c^3$, one is able to accurately reproduce the compressibility of water (Groot97). If the DPD system is gauged in this way, a single *in silico* DPD bead represents approximately three water molecules.

Lipids, membranes and proteins

Lipids are one of the four fundamental building blocks in living cells. They are responsible for the formation of membranes, thin flexible sheets, that define the cell and its internal organelles. Although there is a plethora of different lipid species, their structure is universal: a rather small hydrophilic head is covalently linked to one or two strongly non-polar hydrocarbon chains.

A DPD lipid follows this pattern by linking a hydrophilic head particle to a linear chain of a certain number of hydrophobic tail particles that are in the following denoted by H and T , respectively. We classify model DPD lipids via HT_n where n denotes the number of hydrophobic tail beads. In most of our simulations we used lipids of kind HT_3 as the building block for our model membranes. Figure 3.2 displays a simplified model of a glycerophospholipid and our DPD lipid model. Two adjacent lipid beads are kept together by a simple harmonic potential U_h , an additional bending potential U_b between three consecutive beads is applied

Membrane Simulations

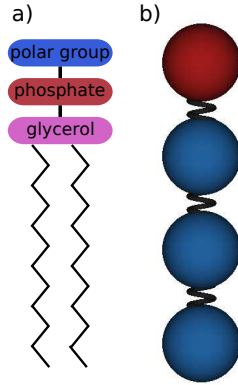


Figure 3.2: Sketch of a typical glycerophospholipid (a) and the corresponding DPD representation (b). The polar head group in (a) can contain a nitrogenous base, a glycerol or an inositol unit. In (b) a single hydrophilic head particle (red) is followed by three hydrophobic tail particles (blue). All DPD particles are connected via harmonic springs as indicated. Note that both pictures are not drawn to scale.

to account for the inherent stiffness of the lipid. Both potentials read

$$U_h(\mathbf{r}_{i,i+1}) = \frac{1}{2} k_h \cdot (r_{i,i+1} - \ell_0)^2 \quad (3.9)$$

$$U_b(\mathbf{r}_{i,i+1}, \mathbf{r}_{i+1,i+2}) = k_b \cdot (1 - \cos(\phi - \phi_0)) \quad (3.10)$$

k_h and k_b are the amplitudes of the harmonic and of the bending potential, respectively. Common numerical values for k_h lie within the range of about $100 k_B T$, the bending stiffness is approximately an order of magnitude smaller, i.e. $k_b \approx 10 - 20 k_B T$. ℓ_0 denotes the harmonic equilibrium distance between two consecutive beads, ϕ_0 is the preferred default angle between three consecutive beads and is, for a linear chain, set to zero. In this case,

$$\cos(\phi) = \mathbf{e}_{i,i+1} \cdot \mathbf{e}_{i+1,i+2}$$

The generalization for non-vanishing default angles ϕ_0 is straightforward and easy to implement (Cheng96).

In real biological systems, membranes are surrounded by an aqueous environment. To mimic this situation, membrane simulations are usually performed with fully-hydrated lipid bilayers, i.e. the surrounding solvent is explicitly modelled. There are approaches that discard the solvent around the membrane and are hence termed implicit-solvent models (Farago03; Brannigan04; Cooke05). The hydrostatic pressure in these simulations is taken into account by additional attractive long-range interactions between lipids in the different leaflets.

In our simulations, the solvent is explicitly modelled, that is we have to establish at least three different types of DPD beads: water (W), head (H) and tail (T) beads. To distinguish between different bead types, one employs the hydrophobicity parameter \mathcal{A} that already occurred in the definition of the repulsive force \mathbf{F}^C . The character of two interacting DPD beads i and j is determined by the numerical value of \mathcal{A}_{ij} : the repulsion between like beads is set to a default value whereas it is increased between water/head beads and tail beads. This allows to

\mathcal{A}	water	head	tail
water (W)	25	25	200
head (H)	25	25	200
tail (T)	200	200	25

Table 3.1: *Interaction matrix of the hydrophobicity parameter \mathcal{A} (in units of $k_B T$) between water, head and tail particles. Water and head beads are essentially equal whereas the repulsion between these and tail particles is much stronger.*

create a plethora of different bead species. Standard values for \mathcal{A} are summarized in Table 3.1.

The integration procedure

DPD simulations can be performed under different conditions that require different integration procedures. Usually, DPD simulations are performed in the NVT ensemble, that is the number of particles, the volume of the simulation box and the temperature are kept constant. This setup proves to be appropriate for simple systems. However, to account for intrinsic properties of biological systems a more sophisticated framework is used. One possibility is that instead of the volume the pressure of the DPD system is kept constant, i.e. the simulations are performed in the NpT ensemble.

NVT ensemble The time evolution of the DPD system is calculated by integration of the equations of motion by using a velocity-Verlet (VV) integration algorithm (Verlet67a; Verlet67b). This is the most commonly used numerical integration scheme in MD simulations. The advantages compared to ordinary Euler schemes are two-fold. On the one hand, a VV integration scheme proves to be a very stable integrator which is manifested in the freedom to choose the time increment Δt approximately a factor of 50 larger than in simple Euler schemes. On the other hand, the underlying numerics are very efficient and do not demand much computation power compared to, for example, Runge-Kutta methods. The integration of the NVT ensemble is performed according to (Nikunen03). The corresponding pseudo-code reads

1. $\mathbf{v}_i \leftarrow \mathbf{v}_i + \frac{1}{2} \frac{1}{m} \left(\mathbf{F}_i^C \Delta t + \mathbf{F}_i^D \Delta t + \mathbf{F}_i^R \sqrt{\Delta t} \right)$
2. $\mathbf{x}_i \leftarrow \mathbf{x}_i + \mathbf{v}_i \Delta t$
3. Update \mathbf{F}_i^C , \mathbf{F}_i^D and \mathbf{F}_i^R
- 4a. $\mathbf{v}_i^* \leftarrow \mathbf{v}_i + \frac{1}{2} \frac{1}{m} \left(\mathbf{F}_i^C \Delta t + \mathbf{F}_i^R \sqrt{\Delta t} \right)$

Membrane Simulations

$$4b. \mathbf{v}_i \leftarrow \mathbf{v}_i^* + \frac{1}{2} \frac{1}{m} \mathbf{F}^D \Delta t$$

5. Update \mathbf{F}_i^D

In all our simulations, steps 1 – 5 are performed only once during a single time step. Steps 4a, b – 5 are to resolve the dependence of the dissipative force on the bead velocities, and vice versa. Although there exist algorithms that loop over steps 4b and 5 until the system temperature converges to its prearranged value, we prefer the simplified version with no self-consistency loop.

One prominent peculiarity is the appearance of $\sqrt{\Delta t}$ in the integration step for the random force. A detailed explanation can be achieved by interpreting the random force as a Wiener process (Risken96). Integration of the underlying stochastic equations leads directly to the observed dependence on $\sqrt{\Delta t}$.

Besides, a heuristic argument to understand the appearance of $\sqrt{\Delta t}$ is as follows: the motion of a particle in a fluid is governed by collisions with other particles. During each time step, the collisions induce a random force f with mean and variance $\langle f \rangle = 0$ and $\langle f^2 \rangle = \sigma^2$, respectively. As the time-integral of the force is proportional to the mean-square displacement of the particle, one concludes that $\langle f^2 \rangle \propto t \cdot \sigma^2 \Delta t$ which would go to zero if Δt decreases. To resolve this unphysical behaviour, the variance of the random forces is coupled to the time increment Δt , that means one has to choose $\langle f^2 \rangle = \sigma^2 / \Delta t$.

NpT ensemble Biological membranes are thought to be tensionless (Boal02). To account for this fact, several computational strategies can be applied. One commonly used technique is to introduce a Monte Carlo algorithm that changes the size of the simulation box at random time points (Venturoli99). Between the individual Monte Carlo steps, the volume of the simulation box does not change. Instead, we use a so-called *barostat*, a method that exists in several implementations (Andersen80; Berendsen84). Here, one does not use a simulation box of fixed size but rather a simulation box that is able to breathe due to a virtual piston system. In this work we follow the barostat implementation developed by Jakobsen (Jakobsen05a).

In order to realize the barostat, the dimensions of the simulation box serve as a piston and introduce three additional degrees of freedom into the DPD system. The motion of the piston is described by a Langevin equation and governed by a force \mathbf{F}_ϵ . This force incorporates several components, like the pressure difference between the present and the target pressure, DPD bead momenta and a dissipative and random force. We note here, that the calculation of the instantaneous pressure includes different contributions one of them being the virial of the DPD system. As a consequence of the Langevin description, a fluctuation-dissipation theorem connected to the motion of the piston has to be satisfied.

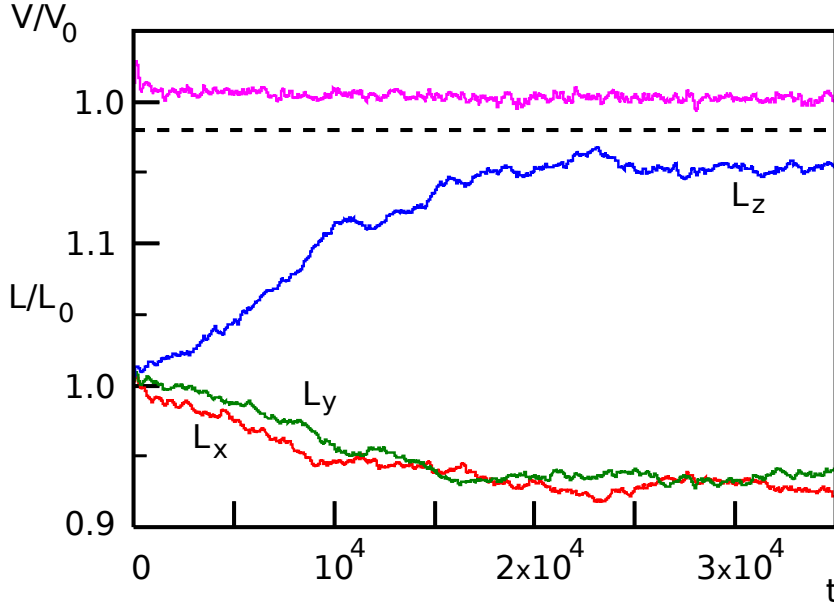


Figure 3.3: Simulation box volume V (upper graph) and the individual box lengths $L_{x,y,z}$ normalized to their initial values. V oscillates around its initial value V_0 , the edge lengths $L_{x,y}$ show a slight decrease that is balanced by an increased value of L_z .

The Langevin description has the advantage that unphysical oscillations of the simulation box as observed in other implementations are suppressed (Jakobsen05b). Every time step involves a re-scaling of the dimensions of the simulation box as well as of the positions of the DPD beads. The scaling factor is influenced by the force \mathbf{F}_ϵ and the so-called rise-time of the barostat.

The above-described DPD-VV integration algorithm is upgraded to include the movement of the piston. Now, a difficult interplay between bead and piston velocity emerges which is again solved by an iterative procedure. One consequence of the applied barostat is that the volume of the simulation box is now fluctuating around its initial value V_0 in order to adapt to the instantaneous conditions. The time course of the volume of the simulation box and of the individual box lengths are depicted in Figure 3.3.

Jakobsen's barostat implementation has several advantages. The time required for equilibration as well as correlation times for various system parameters become shorter. A numerical aspect is that one does not need smaller time steps Δt for the integration procedure of the DPD system so that faster and more efficient simulations can be performed. A complete presentation of the individual algorithmic steps are provided in Appendix A.

3.2 DPD membranes

In this final section, we overview basic features of DPD membranes. We show that our model lipids are capable of self-assembling into membranes, a property that is also found for real lipids. In addition, we determine the distribution of water, head and tail beads along the membrane normal and analyse the membrane's height fluctuation.

DPD lipid self-assembly Real lipids in an aqueous environment are able to form membraneous structures like micelles or lipid bilayers. As pointed out earlier, lipid concentration determines whether self-assembly occurs, and if so, the lipids' shape defines the topology of the aggregate.

Figure 3.4 displays the time course of lipid aggregation into a planar membrane, lipid head and tail groups are represented in red and blue, respectively. In the beginning, all lipids are distributed randomly in the simulation box. After a short period, they start to assemble into higher-order structures that are not yet interconnected. With advancing time, the individual subjects begin to fuse, resulting eventually in a planar membrane. Hence, our simple DPD model lipids are able to reproduce *in vivo* behaviour of lipids.

The distribution of the different DPD beads along the membrane normal, i.e. the z axis, is depicted in Figure 3.5. As can be clearly seen, water particles are located above and below the lipid bilayer, the membrane serves hence as an impermeable barrier. The distribution of lipid head particles has two prominent peaks (arrows) symmetric to the membrane midplane ($z = 0$). The distance between these peaks is a measure for the membrane thickness. Finally, lipid tail groups are buried in the middle of the bilayer. The small dip in the tail density profile indicates that the amphiphiles terminate near the bilayer midplane. This demonstrates that a DPD membrane perfectly maintains its integrity.

Membrane surface fluctuations In the introductory chapter about membranes, the general expression for the Fourier spectrum of a fluctuating surface was derived. As a reminder we give again the formula

$$\langle h(\mathbf{q}) \cdot h^*(\mathbf{q}) \rangle = \frac{k_B T}{A(\tau q^2 + \kappa q^4)} \quad (3.11)$$

with A the membrane area, τ and κ the applied tension and the bending rigidity, respectively. In our simulations, we usually assume that $\tau \approx 0$ so that the q^2 term in the previous equation can be neglected.

As a benchmark, we can check whether our DPD model membranes also satisfy the above equation. To this end, we monitor the height fluctuations of a DPD

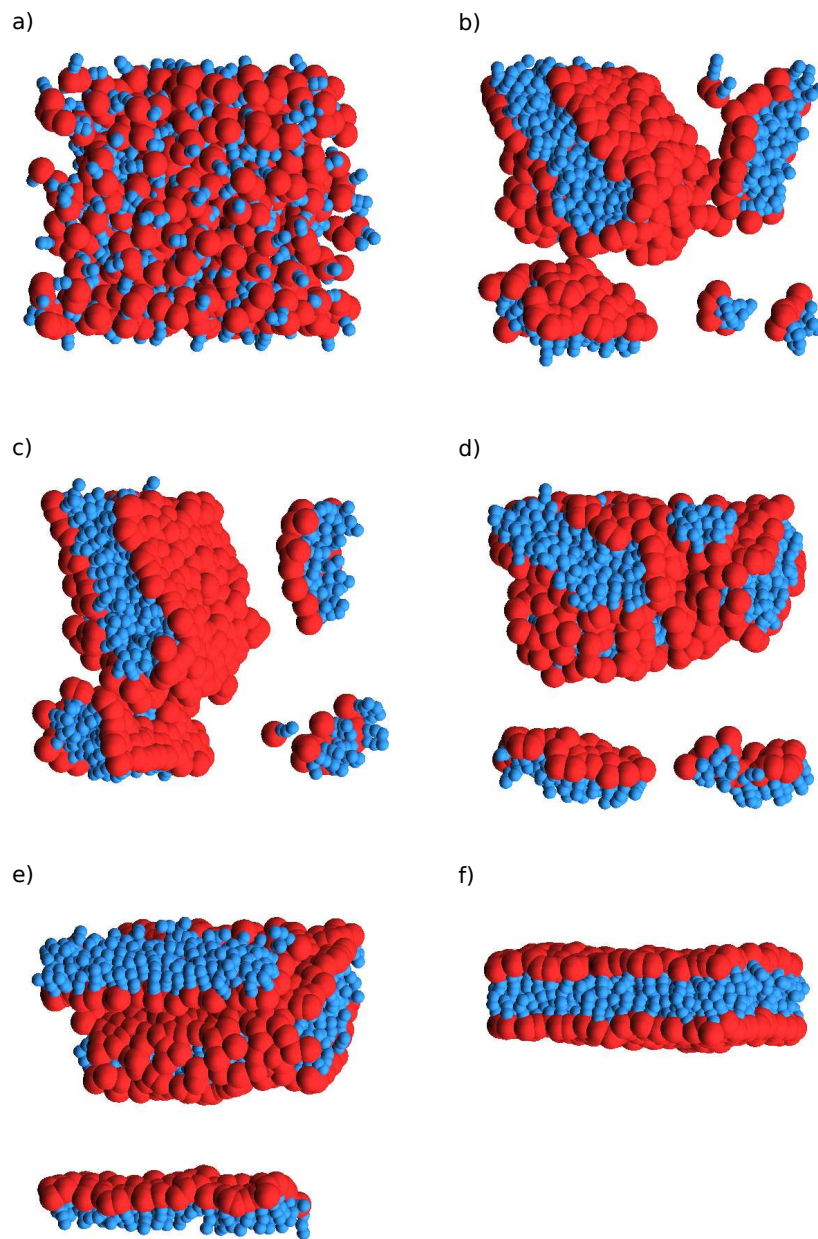


Figure 3.4: *Self-assembly process of lipids in water: an initially randomized ensemble of lipids starts forming higher-order structures like micelles and bilayers when left to their own device. Time course is from top left to bottom right; applied periodic boundary conditions are clearly visible. Red: head groups, blue: tail beads.*

Membrane Simulations

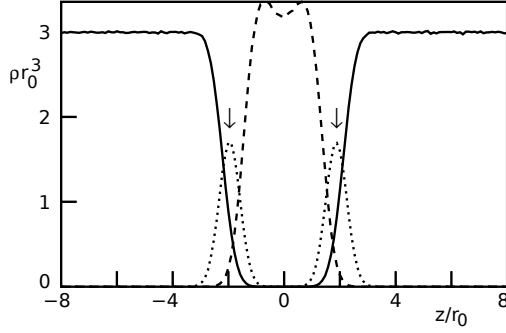


Figure 3.5: Bead number density profiles, ρr_0^3 , for water (solid line), hydrophilic head (dotted line) and hydrophobic tail beads (dashed line). The arrows indicate the average bilayer thickness.

membrane and Fourier transformed the results. The data presented in Figure 3.6 nicely coincides with our expectation. Here, we plotted $\langle h(q)^2 \rangle$ against q^2 which should result in a q^{-2} power law. The accompanying fit (solid line) confirms this prediction for small q -values. At larger wavenumbers q , a cross-over from

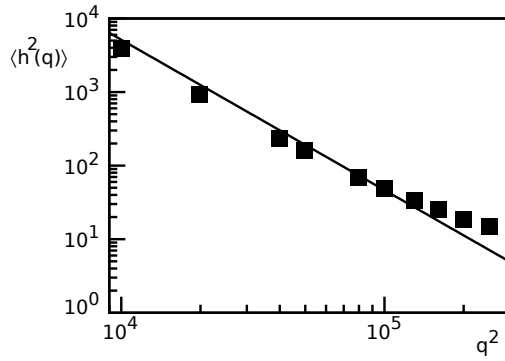


Figure 3.6: Membrane undulations in Fourier space: $\langle h(q)^2 \rangle$ is drawn against q^2 resulting in a power-law behaviour of $\langle h \rangle \propto q^2$ (solid line). Note that both axis are in log-scale and arbitrary units are used.

q^{-4} to q^{-2} behaviour is observed. Although we assumed the membrane to be in a tensionless state, a small tension is still present determining the behaviour at large wavenumbers. Moreover, Equation 3.11 is derived from a continuum theory, our model membranes consist, however, of individual subunits. Therefore, a breakdown of the continuum behaviour at length scales below the bilayer thickness is observable.

Computer simulations are a viable means to investigate complex systems. We have seen that dissipative particle dynamics is a suitable method to study systems on a mesoscopic level. Theoretically predicted events and behaviour are well reproduced rendering DPD a reliable tool to study soft matter and biological systems.

Part II

Results

Chapter 4

The Hydrophobic Mismatch: A universal cellular tool

The present chapter is intended to provide a thorough description of our results induced by *hydrophobic mismatching* (HM) of transmembrane proteins. This structural defect occurs if the thickness of a protein's transmembrane domain (TMD) does not match that of the hydrophobic core of the surrounding lipid bilayer. The membrane protein is thus too long or too short to fit perfectly into the lipid membrane (cf. Figure 4.1).

To study influences of hydrophobic mismatching on the dynamical behaviour of transmembrane proteins, we have performed large-scale computer simulations via dissipative particle dynamics. Our results suggest that hydrophobic mismatching facilitates several intracellular protein-related tasks, for example clustering or demixing of membrane proteins. In addition, being integrated into a lipid bilayer with varying thickness, a transmembrane protein is guided into that part of the lipid bilayer where its HM is minimized. By connecting our findings, we propose a simple, HM-based model of how protein sorting along the secretory pathway may be realized. Related to the latter, we also discuss consequences concerning vesicle formation and the resulting secretory flux.

4.1 Introduction to hydrophobic mismatching

The scenario of hydrophobic mismatching is based on two elementary ingredients: membranes and transmembrane proteins. As pointed out before, membranes define cells and their organelles. According to (Mitra04) membrane thicknesses of organelles along the secretory pathway show slight but distinct differences ranging from 37 to 42 Ångström. A possible explanation for this observation is that different intracellular membranes have different lipid compositions (vanMeer08).

Hydrophobic mismatching

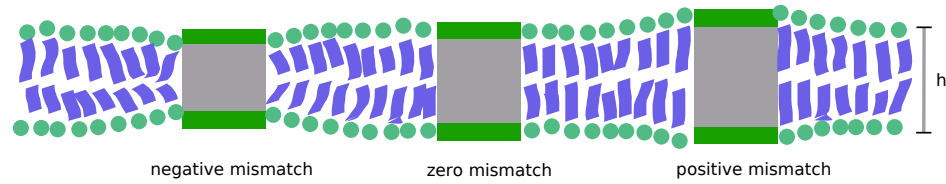


Figure 4.1: *Different cases of hydrophobic mismatching: negative, zero and positive (from left to right). Membrane inclusions affect the membrane thickness h in their direct vicinity. As will be shown later, lipids around membrane proteins are neither stretched nor compressed but rather bend or straighten up in order to shield the hydrophobic part of the protein.*

For example, a high cholesterol content like in the plasma membrane is responsible for an increase in bilayer thickness.

The second ingredient, transmembrane proteins, are abundant in living cells. As already pointed out in former chapters, nearly one third of all endogenous proteins are transmembrane proteins. Their correct function frequently requires a spatial correlation between numerous proteins, i.e. the proteins assemble into higher-order oligomers in order to fulfill their task(s). Traditionally, specific bi-molecular binding events are blamed for this protein aggregation. However, several lines of evidence indicate that unspecific, membrane-mediated interactions also play a major role in these events (Bruinsma96; Simons97; Edidin03) thus relaxing the need for a multitude of fine-tuned interactions.

4.1.1 Historical remarks

In the context of membrane-mediated interactions, the effects of a hydrophobic mismatch has been of particular interest, a detailed review is provided by (Jensen04). In 1976, Marčelja first proposed the existence of lipid-mediated interactions between membrane inclusions (Marčelja76). His molecular-field theoretical results suggest that membrane inclusions may, under ‘favourable circumstances [sic!]’, experience a long-range, lipid-mediated attraction. He traced back the origin of this indirect interaction to local perturbations of the lipid environment in the vicinity of the integral membrane protein. To reduce the perturbed area, membrane proteins are attracted and start to form protein clusters.

The diversity of studies supporting Marčelja’s prediction that hydrophobic mismatching can induce aggregation of transmembrane proteins is numerous. Mouritsen and Bloom employed their ‘mattress model’ to explain lipid-protein interactions (Mouritsen84). Several other authors used mean-field theoretical approaches (Schröder77; Dan93; Dan94) as well as a model based on capillary forces (Kralchevsky95) in support of this hypothesis. Molecular dynamics (Edholm87)

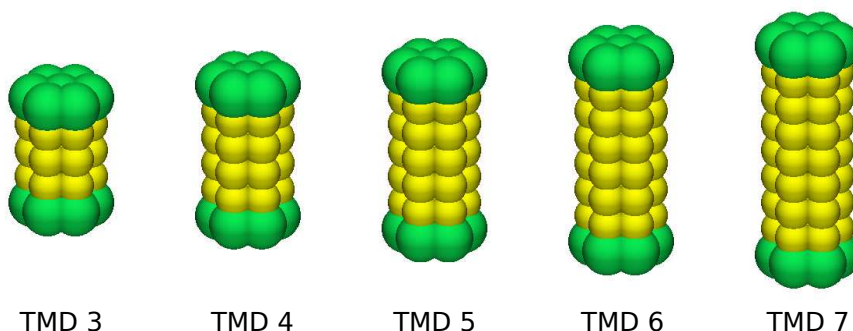


Figure 4.2: *DPD model proteins with different HM are realized by changing the number of transmembrane layers (yellow). In our simulations, proteins with 3, 4, 5, 6 and 7 transmembrane layers exhibit strong negative, negative, negligible, positive and strong positive HM, respectively. Hydrophilic caps are depicted in green and are enhanced for better visibility, transmembrane layers are colored yellow.*

and Monte Carlo (Sintes97) computer simulations corroborate Marčelja's prediction as well.

Although there are many theoretical studies on HM-induced protein clustering, experimental results have remained rare and equivocal in highlighting the pure effects of hydrophobic mismatching (Lewis83; Harroun99). Moreover, it is debatable whether mean-field approaches are capable of providing an appropriate picture of lipid bilayers. These are in fact not two-dimensional continuous fluids but are rather composed of discrete building blocks, lipids and proteins, that have approximately the same size.

Since quantitative experiments are challenging in several aspects, computer simulations allow for a detailed analysis of nano-scale processes on membranes. To elucidate the nature of hydrophobic mismatching and its potential impacts on the dynamical behaviour of transmembrane proteins, dissipative particle dynamics simulations were performed. In the remainder of this chapter, numerical results are presented and implications are thoroughly discussed.

4.2 Clustering of transmembrane proteins due to hydrophobic mismatching

To elucidate the effect of different degrees of hydrophobic mismatching on the aggregation behaviour of transmembrane proteins, a series of computer simulations were performed. Our approach was threefold: i) geometrical effects on the lipid bilayer due to a single embedded protein were analysed. ii) it was tested

Hydrophobic mismatching

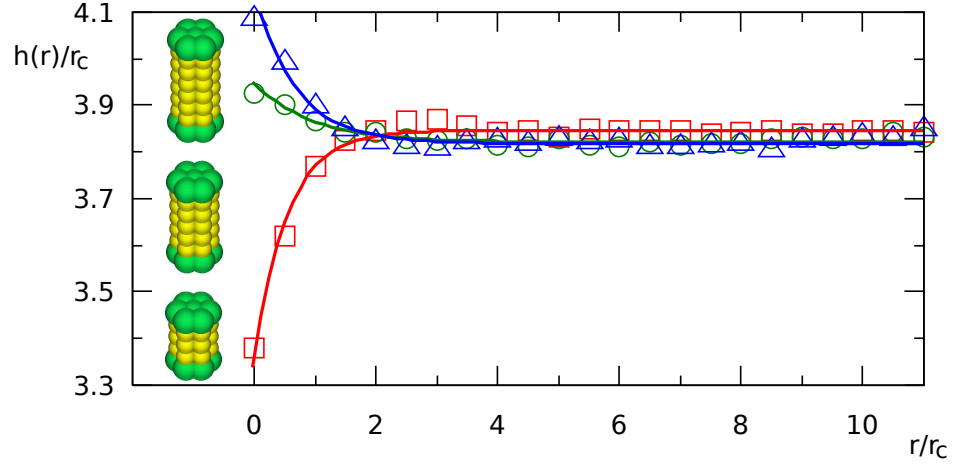


Figure 4.3: Numerically determined membrane thickness profiles $h(r)$ for proteins with three (squares), five (circles) and six (triangles) transmembrane layers. All corresponding profiles are well described by an exponential as theoretically predicted. Insets on the left show the corresponding membrane inclusions.

whether the structural and configurational changes of the lipid bilayer observed in i) really lead to protein attraction. iii) the aggregation behaviour of 30 embedded proteins was monitored, analysed and related to results from ii). Proteins with different length of their transmembrane domain were created as depicted in Figure 4.2. In the following, we denote the number of transmembrane layers by n .

Hydrophobic mismatching disturbs the membrane locally

As already indicated in Figure 4.1, the membrane bilayer around a transmembrane protein is disturbed. The degree of deformation can be characterized by two geometrical quantities, the membrane thickness, h , and the tilt angle of the lipids, ϑ . From the latter entity, an order parameter S can be derived which reflects the configurational state of the lipids. We determined these quantities as a function of the distance from the rim of the protein, i.e. we computed the radial profiles $h(r)$, $\vartheta(r)$ and $S(r)$.

The protein was integrated into a membrane patch of lateral size $L = 20r_c$ to minimize periodic-boundary effects. The different profiles were obtained by drawing concentric rings around the protein center and averaging over all lipids in each annular region.

Figure 4.3 displays the numerically determined membrane thickness profiles $h(r)$

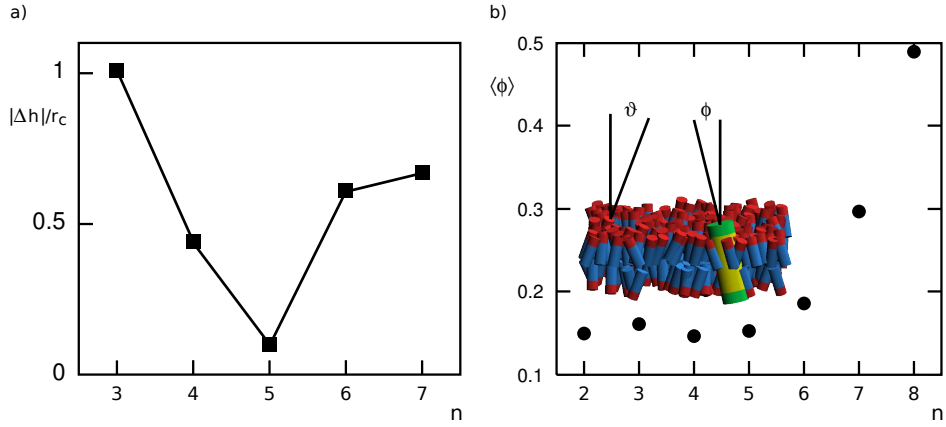


Figure 4.4: a) Absolute value of the hydrophobic mismatch Δh as a function of the number of transmembrane layers n . $|\Delta h|$ exhibits a minimum at $n = 5$ and is nearly constant for larger n . b) The behaviour from a) can be explained by the protein tilt angle $\langle \phi \rangle$ which increases strongly for $n \geq 6$.

for a protein with $n = 3, 5, 6$ transmembrane layers. The shape of the individual profiles share a common property. Far away from the inclusion, $h(r)$ adopts the value of an unperturbed lipid bilayer that is determined in pure membrane simulations as $h_0 \approx 3.84r_c$. Approaching the transmembrane protein alters the membrane thickness. At a distance of about $2r_c$ from the rim of the protein, the membrane thickness either increases ($n = 6$) or decreases ($n = 3$) significantly. This behaviour indicates that the neighboring lipids try to shield the hydrophobic protein core from the surrounding water.

Embedding a membrane protein with five transmembrane layers only yields a slight deviation of the membrane thickness from the unperturbed value h_0 . According to these results, we assign to this protein type a negligible hydrophobic mismatch. Proteins with more or less transmembrane layers are consequently connected with a positive or negative hydrophobic mismatch, respectively.

The simulational membrane thickness profiles (Figure 4.3) are well characterized by an exponential curve

$$h(r) = h_0 + \Delta h \cdot e^{-r/\lambda} \quad (4.1)$$

in agreement with former theoretical predictions (Dan93). Here, Δh reflects the degree of hydrophobic mismatching and λ a characteristic decay length that is in all cases of the same order of magnitude.

The absolute value of Δh shows an interesting course, cf. Figure 4.4a. Starting at a rather large value for proteins with only three transmembrane layers, $|\Delta h|$ decreases steadily until the number of transmembrane layer reaches $n = 5$

Hydrophobic mismatching

where a minimum in hydrophobic mismatch is observed: $\Delta h \approx 0.08$. Increasing the thickness of the transmembrane domain further, enhances the degree of hydrophobic mismatching. However, this increase is not monotonic, i.e. for proteins with even larger transmembrane domains, one does *not* observe a further increase in hydrophobic mismatching. Rather, $|\Delta h|$ settles at an approximately constant value for $n \geq 6$. Based on these finding, our decision to term proteins with five transmembrane layers as ‘neutral’ is further justified.

An explanation for this behaviour is found by inspecting the tilt angle of the proteins with respect to the bilayer normal, ϕ . Proteins with five and less transmembrane layers show a nearly constant tilt angle. Enlarging the protein’s hydrophobic core results in stronger tilted proteins (Figure 4.4b). Thus, it is obviously energetically more favourable to tilt the protein than to stretch the bilayer any further.

We next analysed the orientational character of the membrane lipids. To this end, we computed the radial profile of the lipid tilt angle, $\vartheta(r)$ and derived from this the orientational order parameter $S(r)$ that is defined as follows

$$S(r) = \langle [3\cos^2(\vartheta) - 1] / 2 \rangle$$

S characterizes the local lipid alignment with respect to the bilayer normal. A perfect alignment is indicated by $S = 1$ while a perfect random orientation is reflected by $S = 0$.

In a pure lipid bilayer, the average lipid tilt angle can be estimated from the cylindrical envelope of the lipids. Taking the average area per lipid as $A \approx 1.43/r_c^2$ and a typical lipid length as $\ell \approx 1.8r_c$, the average lipid tilt angle is determined to

$$\langle \vartheta \rangle = \arctan \sqrt{A/(\pi\ell^2)} \approx 0.36$$

Far away from the inclusion, we see a good agreement with this estimate indicating the local character of the membrane deformation. However, $\langle \vartheta \rangle$ deviates significantly in the vicinity of the inclusion, cf. Figure 4.5a. Lipids around an inclusion with a negative HM bend inwards in order to shield the surrounding water. This is in contrast to lipids encircling a positive HM protein. Here, they straighten up to fulfill their protective duty. Finally, a protein with negligible HM hardly affects the lipid tilt angle.

The corresponding order parameter S (Figure 4.5b) corroborates the latter observations. One clearly sees that with decreasing distance r , the order parameter S is near to unity for proteins experiencing a positive hydrophobic mismatch indicating a very good alignment with the bilayer normal. In contrast, lipids around a protein with negative HM are less aligned as reflected by the lower value of $S \approx 0.65$.

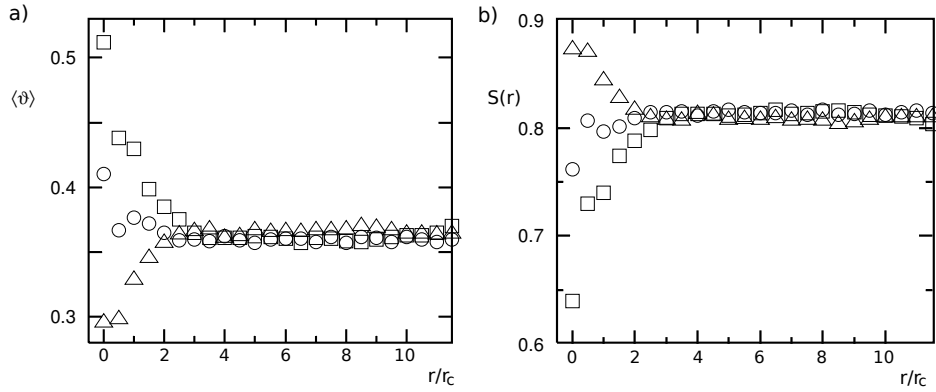


Figure 4.5: Lipid tilt angle $\langle \vartheta \rangle$ (a) and corresponding order parameter S (b). Depending on the thickness of the TMD, the average lipid tilt angle significantly deviates from its bulk value. Positive-HM ($n = 6$) proteins force the lipids to straighten up (triangles) while a negative HM ($n = 3$) induces an inward-bending of the lipids (squares). A negligible mismatch ($n = 5$) does only marginally affect $\langle \vartheta \rangle$ (circles). b) The corresponding order parameter consequently indicates that lipids around a positive-HM protein show a stronger alignment with the bilayer normal compared to other HMs (symbols as in a).

These results suggest that lipids adjacent to a perturbative inclusion have a lower entropy due to their constrained configuration as compared to their mates in an unperturbed bilayer. In the next paragraph, we investigate whether this reduction in entropy is sufficient to induce a clustering of membrane inclusions, similar to the formation of micelles in oil-water mixtures.

Hydrophobic mismatching determines inter-protein sympathy

Theoretical work on the interaction energy between a pair of membrane inclusions has been done previously. Dan et al. (Dan93; Dan94) approach this problem via a mean-field theoretical description. In their work, inclusions are modeled as rigid cylinders integrated into a homogeneous lipid bilayer with zero spontaneous curvature. The interaction energy F per inclusion is equal to the perturbation energy due to its integration into the bilayer. The latter energy depends on the shape of the membrane thickness profile $h(r)$ in-between the inclusions relative to the unperturbed bilayer thickness h_0 , i.e.

$$\delta h(r) = \frac{h(r) - h_0}{h_0} \quad (4.2)$$

Hydrophobic mismatching

The change in energy reflects contributions from stretching (compressibility B) and bending (bending modulus κ) the lipid bilayer and is given by

$$F = 2\pi \int_{r_0}^{r_0+L} dr r \frac{h_0}{v} \left[B \delta h^2(r) + \kappa h_0^2 (\nabla^2 \delta h(r))^2 \right] \quad (4.3)$$

where r_0 is the radius of the inclusion and v denotes the approximate volume per lipid molecule. The integration covers a circular region around an inclusion where L is half the distance between the two inclusions. The equilibrium perturbation profile minimizes the membrane-induced interaction energy; the Euler-Lagrange equation minimizing the interaction energy F thus reads

$$\nabla^4 \delta h = -\frac{B}{\kappa h_0^2} \delta h = -\frac{4}{\rho^4} \delta h \quad \text{with} \quad \rho = \left(\frac{4h_0^2 \kappa}{B} \right)^{1/4} \quad (4.4)$$

where ρ defines a characteristic correlation length of the deformation. Applying the boundary condition that the thickness profile has to match the height of the inclusion at $r = r_0$ further simplifies the latter equation giving

$$F = \frac{2\pi \kappa h_0^3 h}{v} \left[\delta h(r) r \frac{d}{dr} (\nabla^2 \delta h(r)) \right] \quad (4.5)$$

Solving for F and performing a subsequent Taylor expansion, it is possible to determine how the interaction energy depends on the deviation of the membrane thickness directly at the inclusion's rim $h(r_0)$ from its unperturbed value h_0 , i.e. on the hydrophobic mismatch. It follows that

$$F \propto (\delta h(r_0))^2 \quad (4.6)$$

We have to note that the investigation by Dan et al. includes also thoughts how the interaction energy varies if it is dominated by the magnitude of the stretching modulus B . They also treat the integration of cone-shaped membrane inclusions leading to somewhat different results. The interested reader is referred to (Dan93; Dan94).

Our approach to analyse whether the aforementioned decrease in configurational entropy may drive the aggregation of membrane inclusions, is not as elaborate as that of Dan et al. We place two proteins with the same hydrophobic mismatch into a model bilayer. Monitoring the force components along the connection vector between the two inclusions and subsequent integration yields the pair potential that the proteins experience. To scan a reasonable range of hydrophobic mismatches, the number of transmembrane layers varies between $n = 3$ and $n = 7$. Figure 4.6a displays the so-obtained pair potentials $U(r)$ for proteins

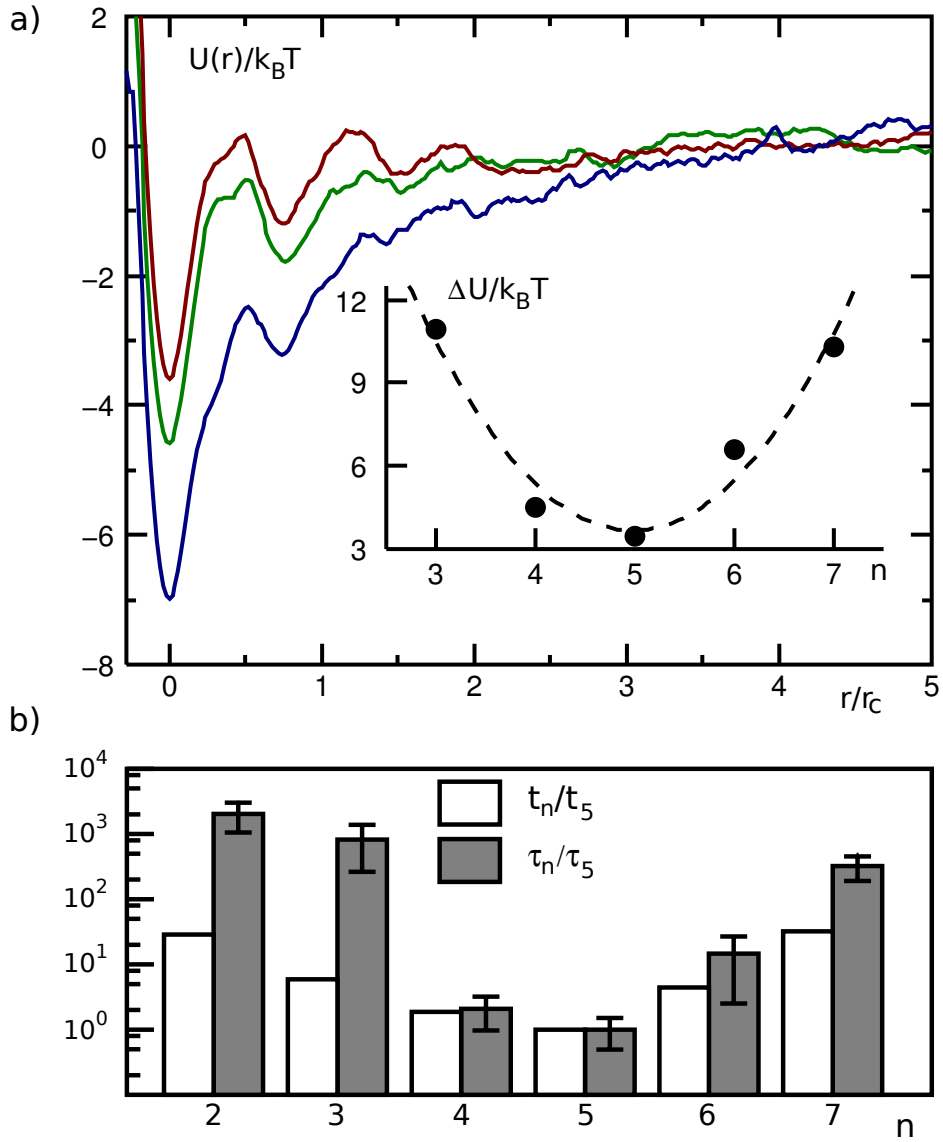


Figure 4.6: a) The mean pair potential between two inclusions with $n = 5, 4, 6$ (from top) shows a minimum for small distances. Inset: The depth of the potential ΔU indicates that dimers with $n \neq 5$ have an increased lifetime. The dashed line highlights the theoretical prediction $\Delta U \propto \Delta_h^2$. The potential curves are shifted so that their minima coincide at $r = 0$. b) The mean dimer lifetime t_n as extracted from the simulations are consistent with the predicted mean-first passage times τ_n derived from $U(r)$. For increasing HM, deviations are observed, presumably because the finite simulation time only yields a lower bound for t_n . Error bars show the variation of τ_n when considering the escape to $2r_c \dots 6r_c$, all time are expressed relative to τ_5 and t_5 , respectively.

Hydrophobic mismatch

with $n = 4, 5, 6$ transmembrane layers. For all cases, the overall shape of these potentials is similar.

Being far apart, the proteins are not able to sense the disturbance of the lipid bilayer. They hence experience a flat potential. With decreasing distance between the proteins, the shape of the pair potential changes significantly. A series of rather shallow minima is followed by a potential well when the two protein are in direct contact.

We further find that the depth of the potential well ΔU shows a nearly quadratic dependence (cf. inset) on the number of transmembrane layers, i.e. on n . The potential well had a minimal depth for proteins with five transmembrane layers, i.e. proteins with a negligible HM. Increasing the hydrophobic mismatch by decreasing or increasing the number of transmembrane layers n yields a quadratic increase in potential depth.

For the sake of completeness, we mention that the envelope of the pair potentials between proteins with three or seven hydrophobic layers are similar to the ones just described here. The only difference is that they now exhibit an even deeper potential well ΔU (cf. inset). The apparent fine structure of all potentials are presumably due to the discrete lipid environment.

The above described pair potentials follow in gross terms previous mean-field predictions (Dan93; Dan94). Moreover, the predicted quadratic dependence of the potential well on the degree of hydrophobic mismatch is also confirmed. Although our simulational model supports the latter two key quantities, we are not able to observe oscillations in the membrane thickness profile as predicted by the same authors. Comparing our results to the capillary force model (Kralchevsky95), we can not confirm the prediction that a negative mismatch induces a stronger attraction than a positive mismatch of comparable degree.

Interestingly, we already observed for a nearly vanishing mismatch ($n = 5$) a transient dimer formation. It is tempting to speculate that in this case not the hydrophobic mismatch but rather the local geometric constraints of the adjacent lipids contribute to the effective attraction.

In part b) of Figure 4.6 the observed dimer lifetimes t_n as extracted from our simulations (white bars) are displayed. Dimers of proteins with five hydrophobic layers have the shortest lifetime while increasing or decreasing the hydrophobic mismatch by changing the number of transmembrane layers resulted in much longer dimer lifetimes. Note that all lifetimes have been normalized to t_5 !

Complementary, we provide the mean-first passage time τ as calculated from the pair potentials (Kramers40), i.e. the time it takes the two protein to escape the potential well and to separate to a certain distance b . τ is determined via the

following formula (Risken96)

$$\tau \propto \int_0^b dr' e^{U(r')} \int_{-\infty}^{r'} dr e^{-U(r)} \quad (4.7)$$

The so-obtained values of τ_n are depicted in Figure 4.6b (gray bars) and normalized to τ_5 . In this case, errorbars reflect the variation in τ if escape to distances $b = 2r_c \dots 6r_c$ is considered.

The mean-first passage times τ_n now exhibit an even stronger increase when the number of transmembrane layers is shifted from the neutral value $n = 5$. The approximate exponential increase of the mean-first passage times also agrees well with theoretical predictions (Kramers40). The discrepancy between τ_n and t_n can be explained by the fact that our simulations are finite. It is thus presumable that our computer simulations are simply too short to cover the whole range of dimer lifetimes.

To conclude this paragraph, we can state that the more pronounced the hydrophobic mismatch, the stronger the resulting lipid-mediated inter-protein attraction. As a consequence, dimer lifetimes with up to $\sim 100 \mu s$ can be observed.

Comparison with the potential of mean force A more elegant way to describe the interaction between a pair of molecules can be done in the framework of the *potential of mean force* (PMF) (Kirkwood35). In general, i.e. a system of N molecules/particles, the potential of mean force w_n determines the force acting on a molecule j in an ensemble of n fixed particles as averaged over all configurations of the remaining $N - n$ molecules. It is given by

$$-\nabla_j w_n = \frac{\int e^{\beta V} (-\nabla_j V) d\mathbf{q}_{n+1} \dots d\mathbf{q}_N}{\int e^{\beta V} d\mathbf{q}_{n+1} \dots d\mathbf{q}_N} \quad (4.8)$$

Here, $\beta = 1/k_B T$, and V is the potential between the particles. Adjusting the above expression to our particular case in which the interaction between two particles (proteins) is to be determined as a function of their mutual distance r , leads to the determination of $w_2(r)$. A more illustrative interpretation of $w_2(r)$ is that it represents the reversible work needed to bring the two particles/proteins from infinity to distance r . In the following, we drop the subscript 2.

According to (Roux95) the potential of mean force along a general coordinate ξ is given by the average distribution function $\langle \rho(\xi) \rangle$

$$w(\xi) = w(\xi^*) - k_B T \ln \left[\frac{\langle \rho(\xi) \rangle}{\langle \rho(\xi^*) \rangle} \right] \quad (4.9)$$

where $w(\xi^*)$ and $\rho(\xi^*)$ are arbitrary reference values. Regarding our problem, ξ is identified by the inter-protein distance r .

Hydrophobic mismatching

Monitoring the potential of mean force or the average distribution function during a straight simulation is nearly impossible. Large energy barriers along the coordinate ξ may prevent an accurate sampling of the configurational space. Therefore, one has to make use of efficient sampling techniques, one of which is *umbrella sampling* (Torrie74). This technique imposes an artificial biasing potential $v(\xi)$ on the system of interest in order to enhance the sampling in the proximity of the chosen value ξ . Since the biasing potential confines the configuration space around the chosen value of ξ , one also speaks of $v(\xi)$ as a ‘window’ potential. To obtain the potential of mean force over the whole range of interest, one usually has to perform a series of biased simulations in each sampling window. A common choice to do this is to use a harmonic potential of the form(Roux95)

$$v(\xi) = v_i(\xi) = \frac{1}{2}k(\xi - \xi_i)^2$$

centered on a set of successive values ξ_i . That means, the potential of the unbiased system V_0 is now complemented by v_i yielding the modified potential

$$V_i(\xi) = V_0(\mathbf{R}) + v_i(\xi) = V_0(\mathbf{R}) + \frac{1}{2}k(\xi - \xi_i)^2 \quad (4.10)$$

where \mathbf{R} represents the coordinates of all particles in the system. The result of this method is a biased distribution function $\rho_i(\xi)$ for each sampling window i . Eventually these have to be unbiased and combined to obtain the final estimate of the potential of mean force w . A crucial point here, is the choice of the amplitude of the harmonic potential k which has to be selected in such a way that consecutive windows overlap. Otherwise, a correct recombination of the individual biased distribution functions to the unbiased total distribution function $\rho_{ub}(\xi)$ is not feasible.

In order to join the biased distribution functions $\rho_i(\xi)$, the weighted histogram analysis method (WHAM) is used (Kumar92). Solving the coupled WHAM equations then yields the unbiased distribution function over the whole range of interest. The WHAM equations read

$$e^{f_i/k_B T} = \int \rho_{ub}(\xi) e^{-v_i(\xi)/k_B T} d\xi \quad (4.11)$$

$$\rho_{ub}(\xi) = \frac{\sum_i n_i \rho_i(\xi)}{\sum_j n_j e^{-(v_j(\xi) - f_j)/k_B T}} \quad (4.12)$$

The parameter f_i is the (initially) unknown free energy in each window due to the biasing potential, n_i is the number of samples in the i -th window, the summation occurs over the total number of sampling windows N_W . Starting from an initial guess of the f_i 's, the above equations are solved self-consistently until

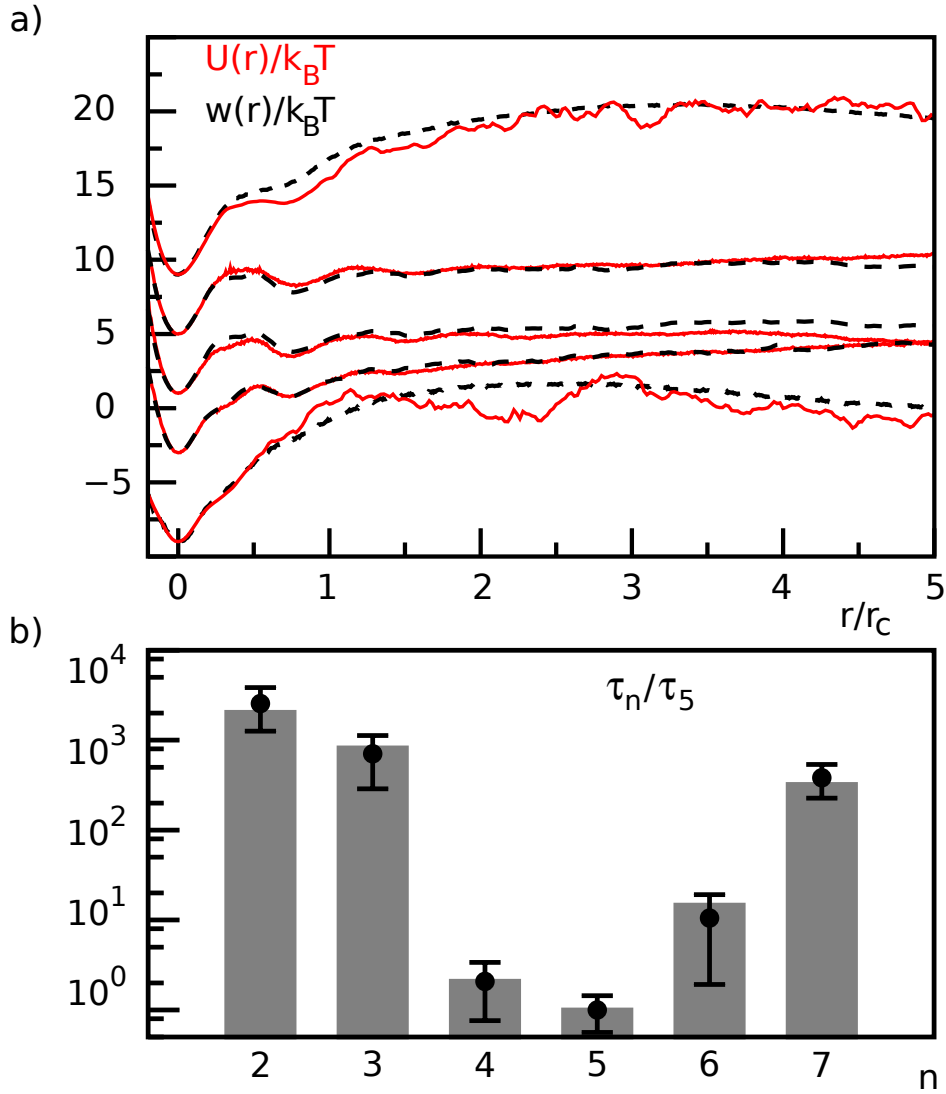


Figure 4.7: a) Comparison of the potential of mean force $w(r)$ (black dashed lines) with the pair potential $U(r)$ (red solid lines) for $n = 3, 4, 5, 6, 7$ transmembrane layers (from top). All potentials have been shifted for better visibility. b) The mean-first passage times as calculated from the PMFs (circles with errorbars) and the pair potentials (grey bars) coincide for all hydrophobic mismatches.

Hydrophobic mismatching

convergence is reached. Subsequently, the unbiased total distribution function serves to determine the potential of mean force by using Equation 4.9. Restricting the potential of mean force to evolve towards zero at large distances, the PMF is given by

$$w(\xi) = -k_B T \ln(\rho_{ub}(\xi)) \quad (4.13)$$

To compare the pair potentials $U(r)$ obtained by the simple integration of force components, we performed also extensive free energy calculations on our system by using umbrella sampling. Following the approach of (deMeyer08), we chose to impose a harmonic biasing potential with amplitude $k = 10k_B T$ on our DPD system with two proteins; the i -th sampling window was centered around

$$\xi_i = \xi_0 + i\Delta\xi \quad \text{with} \quad \Delta\xi = 0.2r_c$$

The coordinate ξ was identified with the distance of the proteins' center of mass. Figure 4.7a compares the potential of mean force $w(r)$ with the pair potentials $U(r)$ for different hydrophobic mismatches. The potentials of mean force $w(r)$ have in general a smoother shape than the corresponding pair potentials $U(r)$. This qualitative property is best highlighted for proteins pairs with strong negative/positive mismatch (top and bottom graphs). In addition, the enhanced sampling process prevents the PMFs from fluctuating at larger protein separations. In the region of the potential well, the two potentials coincide.

The only experimentally accessible observable, the mean-first passage times τ_n , as calculated from the potential of mean force, are in perfect agreement with the former derived values of τ_n , see Figure 4.7b. Although the calculation of the potential of mean force via umbrella sampling is more elaborate than a simple integration of force components, the results and the derived physical observables do not differ.

Hydrophobic mismatching drives protein clustering

To test whether a larger hydrophobic mismatch also leads to a stronger protein clustering, further large-scale simulations were performed. We now inserted 30 transmembrane proteins with equal HM into a homogeneous lipid bilayer of lateral size $L = 50r_c$. The protein density in this scenario is in agreement with estimates of physiological values that are of the order of 10^4 proteins per μm^2 . Qualitative and quantitative data is presented enhancing and supporting previous results.

The left column in Figure 4.8 shows characteristic snapshots of the large-scale simulations of proteins with negative, negligible and positive hydrophobic mismatch (from top). As can be seen in the top and bottom picture, proteins with a non-vanishing hydrophobic mismatch display indeed a strong clustering behaviour. Among few monomers, higher-order oligomers are abundant for both

negative ($n = 4$) and positive ($n = 6$) hydrophobic mismatch. Inspection of the whole time series does not reveal any coalescence of proteins into one large aggregate. We rather observe a dynamic attachment and detachment of single monomers from larger aggregates as well as merging of higher-order oligomers. In contrast, proteins with negligible mismatch ($n = 5$) are not able to form clusters. Here, a dispersed distribution of mainly monomers and single dimers are seen, trimers are rare and not very stable. The latter result thus confirms our previous observation that these dimers have a very limited lifetime.

To support these qualitative momentary pictures, we determined the time-averaged cluster size distribution $P(m)$ for different hydrophobic mismatches. Here, m denotes the number of proteins in an individual cluster. In order to obtain this distribution, we impose a square lattice in the xy -plane on the lipid membrane. Hence, the position of each protein can be assigned a site (i, j) on the lattice. To avoid multiple occupied lattice sites, we vary the grid constant until each protein resides at exclusively one lattice point. The result of this procedure is interpreted as a matrix C whose entries c_{ij} state whether the corresponding lattice site is occupied by a protein ($c_{ij} = 1$) or not ($c_{ij} = 0$). Subsequently, the Hoshen-Kopelman algorithm (Hoshen76) is used to analyse this occupancy matrix and to determine number and size of existent protein clusters.

The right column in Figure 4.8 displays the cluster size distribution for proteins with $n = 4, 5$ and 6 transmembrane domains (from top). One striking property of $P(m)$ for proteins with a negligible hydrophobic mismatch, i.e. $n = 5$, is that it vanishes for $m > 5$. Hence, protein clusters consisting of more than five membrane inclusions are not existent during the whole simulation time. In addition, the vast majority of proteins is available in the monomeric state, accompanied by few dimers and trimers.

This is in contrast to protein ensembles that experience a hydrophobic mismatch. Although the corresponding cluster size distributions show great abundance of monomers as well (top and bottom graph), oligomers with more than five proteins are also likely to exist. In addition, the probability to observe smaller clusters ($m = 2, 3, 4, 5$) is enhanced compared to the case of a negligible hydrophobic mismatch.

The increased probability to observe single monomers in all cases can be explained by the properties of the Hoshen-Kopelman algorithm. This algorithm only takes into account nearest neighbor sites for its cluster analysis. That means, two diagonally separated proteins are not recognized as a dimer, but rather as two individual monomers. Additionally, aggregates that cross the periodic boundaries are also not recognized as a whole, but the individual fragments are analysed separately. Hence, the number of smaller cluster (especially monomers) is overestimated at the expense of higher-order oligomers. Nevertheless, $P(m)$ proves to be a suitable measure to characterize the protein ensemble in gross terms. It

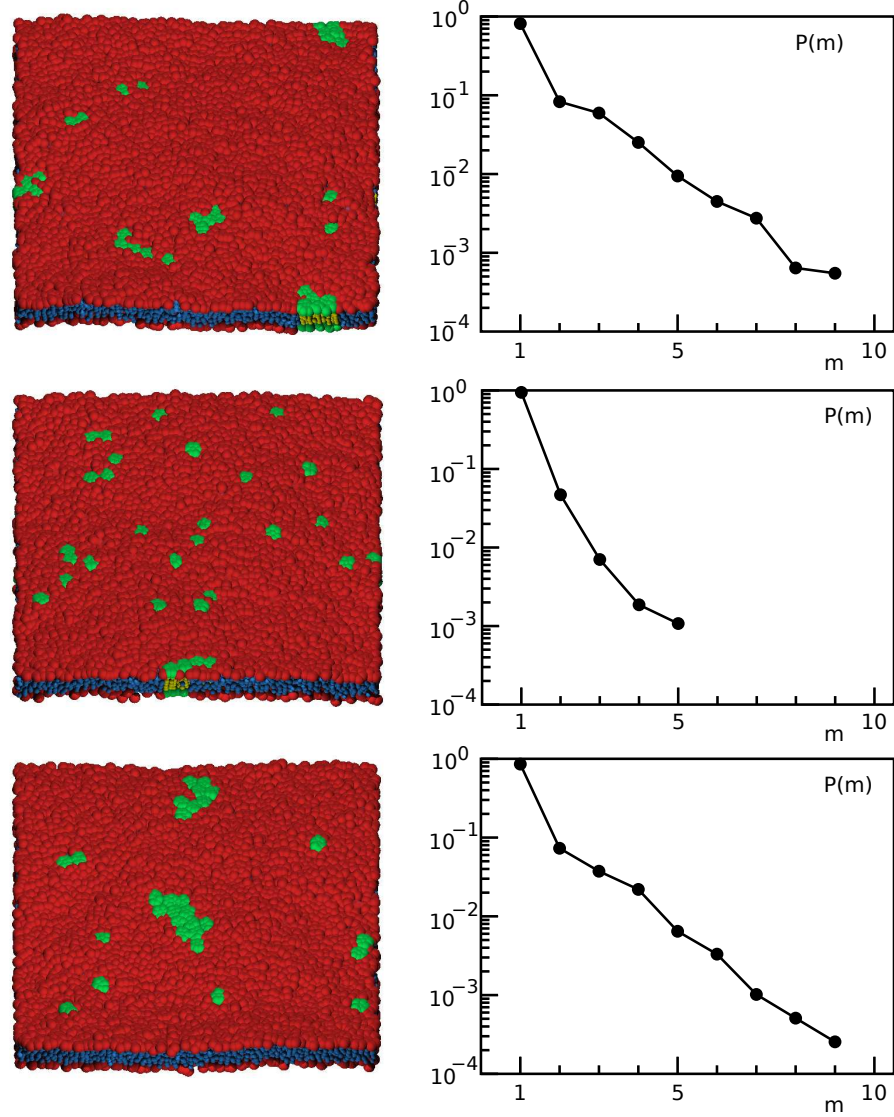


Figure 4.8: Left column: membrane configuration after $\approx 10^6$ time steps for proteins (green) with negative, negligible and positive HM (from top). These snapshots indicate that a non-vanishing HM indeed drives cluster formation. Lipids are colored red (heads) and blue (tails). Right column: cluster size distribution $P(m)$ as derived from the simulations. While clusters with more than five proteins are not observed for proteins with negligible HM, the probability to observe such higher-order oligomers is increased for non-vanishing HM.

also clearly indicates that proteins with a non-vanishing hydrophobic mismatch are more prone to aggregate compared to proteins that are nearly flush with the surrounding membrane.

Estimation of the cluster size distribution Determining the cluster size distribution of the previously described large-scale simulations turns out to be challenging. Although the Hoshen-Kopelman algorithm gives a rough approximation of the cluster size distribution for rather small systems, one is usually interested in the behaviour of larger systems. Here, the prohibitively large computation time impedes the derivation of the cluster size distribution. We therefore considered the following model to estimate the number of m -clusters, p_m , in a system of M point-like proteins.

$$\frac{dp_m}{dt} = \frac{R}{2} \sum_{i=1}^{m-1} p_i p_{m-i} (1 + \delta_{i,m-i}) - R \sum_{i=1}^{M-m} p_m p_i (1 + \delta_{i,m}) + J_m \quad (4.14)$$

The first and second term account for the gain and loss of m -clusters, respectively, due to the diffusively driven aggregation of two clusters. The corresponding aggregation rate R can be derived as follows: according to Saffman and Delbrück (Saffman75), the diffusion coefficient D of membrane inclusions depends only marginally on their size. Consequently, one may refer to R as the inverse diffusive search time on a membrane of lateral size L which finally gives $R = D/L^2$. The last term in Equation 4.14, J_m , describes the loss of single proteins from the rim of a cluster and is given by

$$\begin{aligned} J_1 &= \gamma \sqrt{8} p_2 + \gamma \sum_{k=3}^M \sqrt{k} p_k \\ J_m &= \gamma \left(\sqrt{m+1} p_{m+1} - \sqrt{m} p_m \right) \quad 1 < m < M \\ J_M &= -\gamma \sqrt{M} p_M \end{aligned} \quad (4.15)$$

The evaporation rate γ is identified with the inverse observed dimer lifetime t , i.e. $\gamma = 1/t$. For the sake of simplicity, we do not take into account three-body events, i.e. the aggregation of or the breakup into three individual clusters, respectively. It is of further note that the total number of proteins

$$\sum_m p(m)m = M$$

is conserved under the dynamics of Equation 4.14. In contrast, the number of protein clusters $\sum_m p(m)$ is not conserved.

Hydrophobic mismatch

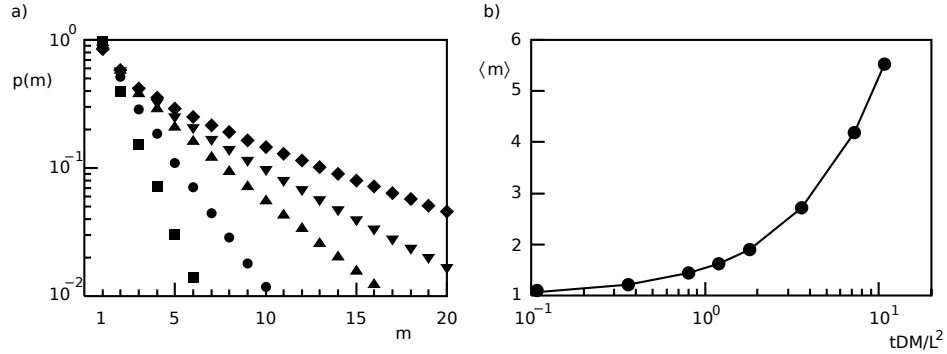


Figure 4.9: a) The cluster size distribution $p(m)$ (Equation 4.14) for $tDM/L^2 = 0.1, 0.36, 1.8, 3.6, 7.2$ (squares, circles, triangles, inverted triangles, diamonds) underlines the existence of larger clusters for increasing hydrophobic mismatch. b) The mean cluster size $\langle m \rangle$ as derived from a) also increases with increasing mismatch.

The numerically obtained values for t and D were now used to calculate the steady-state cluster size distribution for different values of the ratio DMt/L^2 , that is for different hydrophobic mismatch. As depicted in Figure 4.9a, the simple model predicts that higher-order oligomers of up to 10mers are likely to exist for large hydrophobic mismatch. The monotonic rise of the mean cluster size $\langle m \rangle$ also supports this prediction (cf. Figure 4.9b).

Moreover, a relatively large amount of free monomers and dimers is to be expected for every tested value of DMt/L^2 . This scenario is unfortunately not observed in our simulations. A reason for this discrepancy can result from our assumption that dimers and larger cluster are equally stable which may be an oversimplification. However, given the simplicity of the dynamical model, Equation 4.14 can be expected to actually underestimate the mean cluster size by overestimating the number of free monomers. Nevertheless, this simple model is a valuable tool to determine a lower boundary for the mean cluster size.

Summarizing so far, we can state that the conditions for membrane protein clustering, which is a frequent and often vital phenomenon in living cells, can be relaxed by the protein's hydrophobic mismatch with the surrounding membrane. A reduction in configurational entropy of the lipids surrounding the protein is responsible for a long-ranged, lipid-mediated inter-protein attraction. Protein dimers formed by this mechanism can already be stable entities, larger clusters appear to be even more persistent. The distinctive tendency to form protein aggregates can be connected with such 'imperfect' membrane proteins.

4.3 Segregation of transmembrane proteins via hydrophobic mismatching

Connected to the results described above, the question whether hydrophobic mismatching also allows for a differential de-mixing of proteins according to their hydrophobic mismatch arises. For this purpose, we modified the large-scale simulations of the previous section in the following way. Instead of including 30 identical proteins, the number of transmembrane domains of half of the proteins are changed in the same manner resulting in a binary mixture of transmembrane proteins. In the following, we refer to the different protein species as A and B , respectively. Here, we focus on the question whether a HM-dependent protein segregation is observable, and we discuss qualitative and quantitative results.

4.3.1 Analysis of protein co-localization

One crucial aspect regarding protein de-mixing is the spatial correlation between proteins of different species. To elucidate the temporal and spatial segregation behaviour of a binary protein mixture, we analysed time series of simulation snapshots and performed statistical analysis on the co-localization patterns of proteins. In our simulations, we included every possible combination of two protein species with different number of transmembrane layers n from the set $\{3, 4, 5, 6, 7\}$.

Despite the tremendous numerical effort, we restrict ourselves to discussing three central cases. The first case represents compositions of proteins with the same type of mismatch, i.e. positive (negative) and strong positive (negative) mismatch, respectively. Second, one has mixtures of proteins with opposing hydrophobic mismatch. Finally, one can combine proteins with negligible and non-vanishing HM. In the following, we denote a mixture of proteins with n and m hydrophobic layers as $\text{TMD}_{n/m}$. We remind the reader that proteins with five hydrophobic layers possess a nearly vanishing mismatch, increasing or decreasing the variable n results in a positive or negative mismatch, respectively.

A quantitative analysis was performed by making use of the so-called pair cross correlation function (PCCF) (Stoyan95). This function can be used to characterize whether an ensemble of particles of different types exhibit co-localization. Basically, the PCCF provides ratios of local particle densities to their global density. Consider a binary mixture of particles: around each particle of the first type, concentric circles are drawn. The local density of particles of the second type is now determined in each annular region and the ratio with the global second-type particle density is calculated which gives the pair cross-correlation function dependent on distance. The PCCF indicates at which inter-protein distances a

Hydrophobic mismatching

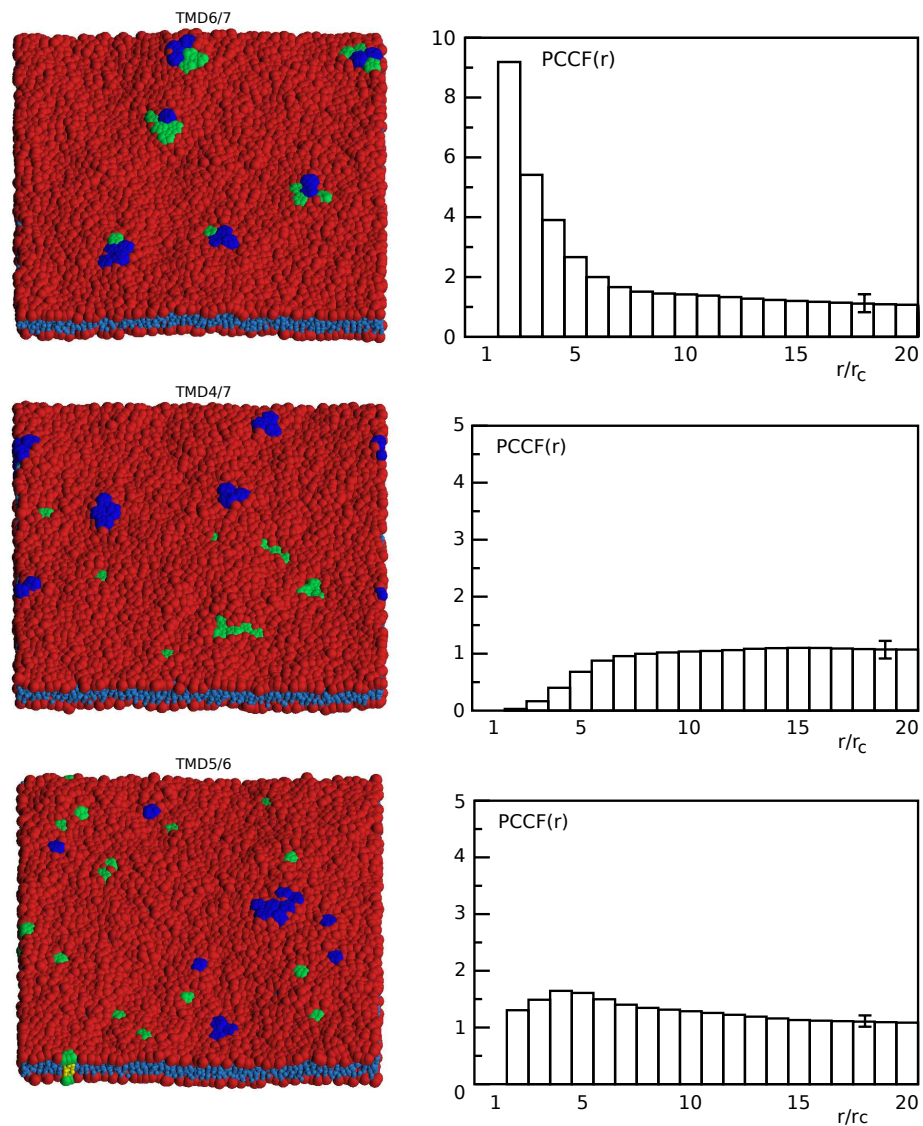


Figure 4.10: Snapshots of binary protein mixtures (left) and corresponding pair cross correlations functions (right). While snapshots of TMD4/7 (middle) and TMD5/6 (bottom) mixtures show a distinct protein segregation, TMD6/7 (top) mixtures do not. The instantaneous pictures are supported by the PCCFs that are averaged over the whole simulation time. The errorbars in the single plots indicate the mean error of data points. Lipids are colored red (head) and light-blue (tails), shorter proteins are colored green, larger in blue. Note the different scales in the PCCF plots!

local change in particle density is observed serving as a means to identify particle co-localization. One has to note that the PCCF does not change if the roles of first and second particles are exchanged. Following this construction, the PCCF approaches unity if $r \rightarrow \infty$.

Representative snapshots of the spatial protein distribution for different binary protein mixtures and the corresponding pair cross correlation functions are provided in the left and right column of Figure 4.10, respectively. The corresponding protein mixture are TMD6/7, TMD4/7 and TMD5/6 (from top).

One striking property of the uppermost snapshot is a pronounced co-localization of the two protein species. One observes six distinct hetero-oligomers of roughly the same size that appear to be evenly distributed in the lipid bilayer. A qualitatively similar picture is found when inspecting a protein composition where both species exhibit a negative mismatch, i.e. TMD3/4. Hetero-oligomers are exclusively observed, negating the answer of a possible protein segregation, at least in these scenarios.

The corresponding PCCFs exhibit a very prominent peak for small inter-protein distances. The local density is in these cases more than 10-fold increased compared to its global value indicating a strong protein co-localization. The PCCF thus supports the qualitative snapshot.

In contrast to the latter case, a binary mixture of proteins with opposite HM clearly displays a differential separation. A representative example is given in the middle row of Figure 4.10 which shows the distribution of proteins with negative ($n = 4$, green) and positive mismatch ($n = 7$, blue). Homo-oligomers of both protein types are present exhibiting a distinct spatial separation between each other.

The PCCF in this case is nearly zero for small distances and approaches its limiting value for increasing values of r . This behaviour clearly proves that proteins with different types of mismatch repel each other and are prone to attract alike proteins. As before, similar mixtures, e.g a TMD4/6 or TMD3/6 protein composition, behave in the same way.

The bottom row is reserved for the last possible case. Proteins with negligible HM are mixed with proteins with a non-vanishing HM. In our notation, the snapshot shows a TMD5/6 protein mixture. We can now observe a third scenario: inclusions with five transmembrane layers are spatially dispersed while their counterparts with six hydrophobic layers aggregate. Interestingly, hetero-oligomers are not present although some proteins of different types are in close proximity. One can conclude that the tiny positive HM of proteins with $n = 5$ does really not affect their dynamics.

The associated PCCF exhibits a maximal change in local protein density for $r \approx 5r_c$ but then steadily levels off for increasing inter-protein distances. The mentioned peak confirms that proteins of different type show a certain proximity

Hydrophobic mismatching

that can not yet be interpreted as a clustering effect. It is noteworthy that all protein compositions of the last kind follow the described behaviour.

A general observation we have made is that the default behaviour of our DPD model proteins did not change when they were part of a binary protein mixture. Proteins with a non-vanishing hydrophobic mismatch were prone to cluster while proteins with negligible HM were not. In addition, the continuous formation and disintegration of protein clusters persist as well.

To conclude, we can state that HM-induced protein segregation is observed if hydrophobic mismatching is sufficiently different. Proteins with similar HMs co-localize into hetero-oligomers while proteins with opposite HMs separate. The default protein behaviour, i.e. HM-induced clustering, as described in the preceding section is conserved.

4.4 Hydrophobic mismatching as a lipid environment sensor

In this section we explore the commonly anticipated protein partitioning to that part of a lipid bilayer that yields the least hydrophobic mismatch. To this end a heterogeneous membrane was set up via two lipid species of different length that are expected to induce a spontaneous lipid segregation. The formation of co-existing lipid phases with different thicknesses has been reported for a variety of ternary lipid mixtures (Veatch05) and it is assumed to also occur on cellular membranes.

4.4.1 Lipid phase separation in membranes

Typical biomembranes have a very heterogeneous character, they usually accommodate a plethora of different lipid molecules. To model the potentially different lipid composition we made the following approach: consistent with previous simulations, the lower membrane leaflet accommodated exclusively short lipids while the upper leaflet was a 1:1 mixture of short and long lipids. Short and long lipids correspond here to HT_3 and HT_6 lipids, respectively. This binary lipid mixture already has the ability to spontaneously phase separate. However, to allow for a more efficient phase separation, we slightly increased the repulsion parameter between the different lipid head groups to $\mathcal{A} = 30k_B T$. We have to note that this alteration did only accelerate the phase separation process but did neither affect nor modify the subsequent results. In contrast to previous simulations, we now provided the lipids with a stronger bending rigidity that has the positive effect that membrane inclusions with five hydrophobic layers are now nearly perfectly

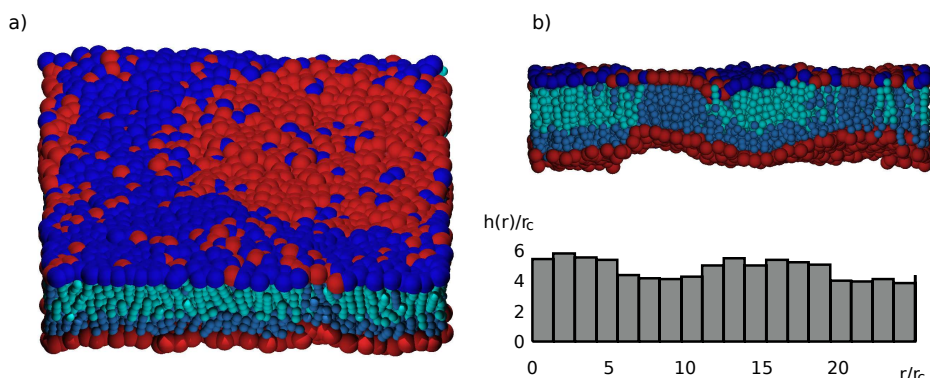


Figure 4.11: a) A lipid bilayer composed of different kinds of lipids shows a lipid phase separation. Here, half of the short lipids (HT_3) in the upper leaflet were replaced by long lipids (HT_6), resulting in a membrane with non-uniform thickness. Short lipids are colored red (head) and light-blue (tails), long lipids are blue (head) and cyan (tails). b) The cross-section through such a lipid bilayer clearly displays the variations in membrane thickness due to the mixed lipid composition. The corresponding thickness profile is shown below. Color coding as in a), for reasons of illustration, the snapshots a) and b) were taken at different times.

flush with a pure HT_3 bilayer (see below for details).

In Figure 4.11a) a nice lipid phase separation is visible, the head groups of short and long lipids are colored red and blue, respectively. Two large areas with predominantly short or long lipids are observed in which single lipids of the other kind are occasionally dispersed. At the front edge one can also recognize the tail beads of the different lipids that are colored light-blue (short) and cyan (long). In part b) of Figure 4.11, a cross section through such a heterogeneous membrane is shown. Here, membrane domains of different thickness are clearly visible. Below, the corresponding membrane thickness profile is shown underlining the existence of membrane sectors with varying thickness. Note that for reasons of better visibility the snapshot in b) was taken at a different time point as that in a).

4.4.2 Proteins try to minimize their HM

After establishing an equilibrated lipid membrane with varying thickness, we investigated the partitioning behaviour of transmembrane proteins with different hydrophobic mismatches. For this purpose, we removed a bunch of lipids from the membrane, filled the void with a single protein and, after a second equilibration period, monitored the distribution of short and long lipids in a circle of radius $4r_c$ around the center of the integrated protein as a function of time. Our

Hydrophobic mismatching

n=4		n=5		n=6	
Δ_s	Δ_l	Δ_s	Δ_l	Δ_s	Δ_l
$-0.51r_c$	$-1.68r_c$	$-0.03r_c$	$-1.14r_c$	$0.51r_c$	$-0.47r_c$
\rightarrow thin region		\rightarrow thin region		\rightarrow thick region	

Table 4.1: *Hydrophobic mismatches Δ_s and Δ_l for proteins with $n = 4, 5, 6$ transmembrane layers. The proteins are expected to migrate to that region of the lipid bilayer where their HM is minimized. Consequently, proteins with four or five hydrophobic layers prefer the thin part of the heterogeneous membrane while proteins with six transmembrane layers rather partition into the thicker bilayer region.*

aim was to check whether hydrophobic mismatching may guide a transmembrane protein into the lipid phase where its HM is smallest.

The presence of short and long lipids in the upper leaflet is responsible that the hydrophobic mismatch of an embedded protein is now dependent on the protein's lateral position. Being exclusively surrounded by short lipids or long lipids yields different degrees of hydrophobic mismatching we term Δ_s and Δ_l , respectively. The degree of HM can be measured via the difference between the (corresponding) unperturbed bilayer thickness and the bilayer thickness at the boundary of the embedded protein. Table 4.1 summarizes these values for proteins with $n = 4, 5, 6$ transmembrane layers as well as the membrane region the proteins are expected to partition into.

By construction, proteins with four hydrophobic layers experience a negative HM in both lipid phases. However, the degree of HM in the thin bilayer region ($\Delta_s = -0.51r_c$) is considerably smaller than that in the thicker part of the lipid bilayer ($\Delta_l = -1.68r_c$) predicting that such proteins are preferably found surrounded by short lipids. In fact, pictures from the corresponding steady-state configuration confirm this prediction (cf. Figure 4.12a) The protein (green) is floating in a sea of short lipids (red) being well-separated from the long lipids (blue).

Additional support is provided by the time-averaged lipid distribution in a circle of radius $4r_c$ around the protein: short lipids constitute nearly 90% of the total number of lipids in this region, long lipids only represent a small minority.

The situation does not change when comparing the different HM values for a protein with $n = 5$ transmembrane layers. Since this kind of proteins shows a nearly vanishing HM in the domain of short lipids, $\Delta_s = -0.03r_c$, it is no surprise that these proteins also diffuse into this domain and avoid – due to the

rather large value of $\Delta_I = -1.14r_c$ – being located in the complementary region. Again, the time-averaged lipid distribution supports the accompanying snapshot (Figure 4.12 b).

Opposite results are found for proteins with six hydrophobic layers. To minimize its HM, the protein now migrates into the part of the lipid bilayer where long lipids determine the membrane thickness. However, the competition between the two HMs is now not as unfair as compared to the previous cases: the values of $\Delta_s = 0.51r_c$ and $\Delta_I = -0.47r_c$ differ only by about 10% and it is remarkable that this small difference is obviously sufficient to guide the protein to the right part of the membrane, i.e. the part where the protein's HM is minimized. This finding is also reflected in characteristic snapshots and the associated lipid distribution that are depicted in part c) of Figure 4.12.

These results demonstrate that proteins diffusively partition into the lipid phase with the smallest hydrophobic mismatch. A similar behaviour can be expected if lipid bilayers with symmetric leaflets are considered. A remarkable property is that the navigational skills connected to a protein's HM are very sensitive since differences in HM of about 10% are already distinguishable. It is therefore conceivable that a complete demixing and partitioning of ternary and even more complex protein mixtures is possible.

It is worth noting that our simulational results support previous experimental data. Ronchi et al. (Ronchi08) created mutations of transmembrane proteins with different lengths of the transmembrane domain. They interpreted the observed altered partitioning behaviour as being due to the change in hydrophobic mismatch.

4.5 Protein sorting by hydrophobic mismatching

Transport of transmembrane proteins along the secretory pathway is mediated by different means. While anterograde cargo molecules are exported from the ER at specialized domains (ER exit sites) via COPII vesicles, unfolded and ER-resident proteins are retained. At the level of the Golgi apparatus, cargo proteins and Golgi-resident enzymes are sorted differentially into distinct cisternae by means of the COPI machinery. As a consequence, Golgi enzymes have been observed to show gradient-like distributions across the Golgi stack in steady-state (Rabouille95). Indeed, stationary, non-uniform distributions of a plethora of transmembrane proteins occur throughout the secretory pathway, that is from the ER via the Golgi complex to the plasma membrane.

To solve the riddle of how transmembrane proteins determine their correct localization, two models have been proposed. The kin recognition hypothesis (Nilsson93) invokes the (temporary) formation of larger hetero-oligomers due

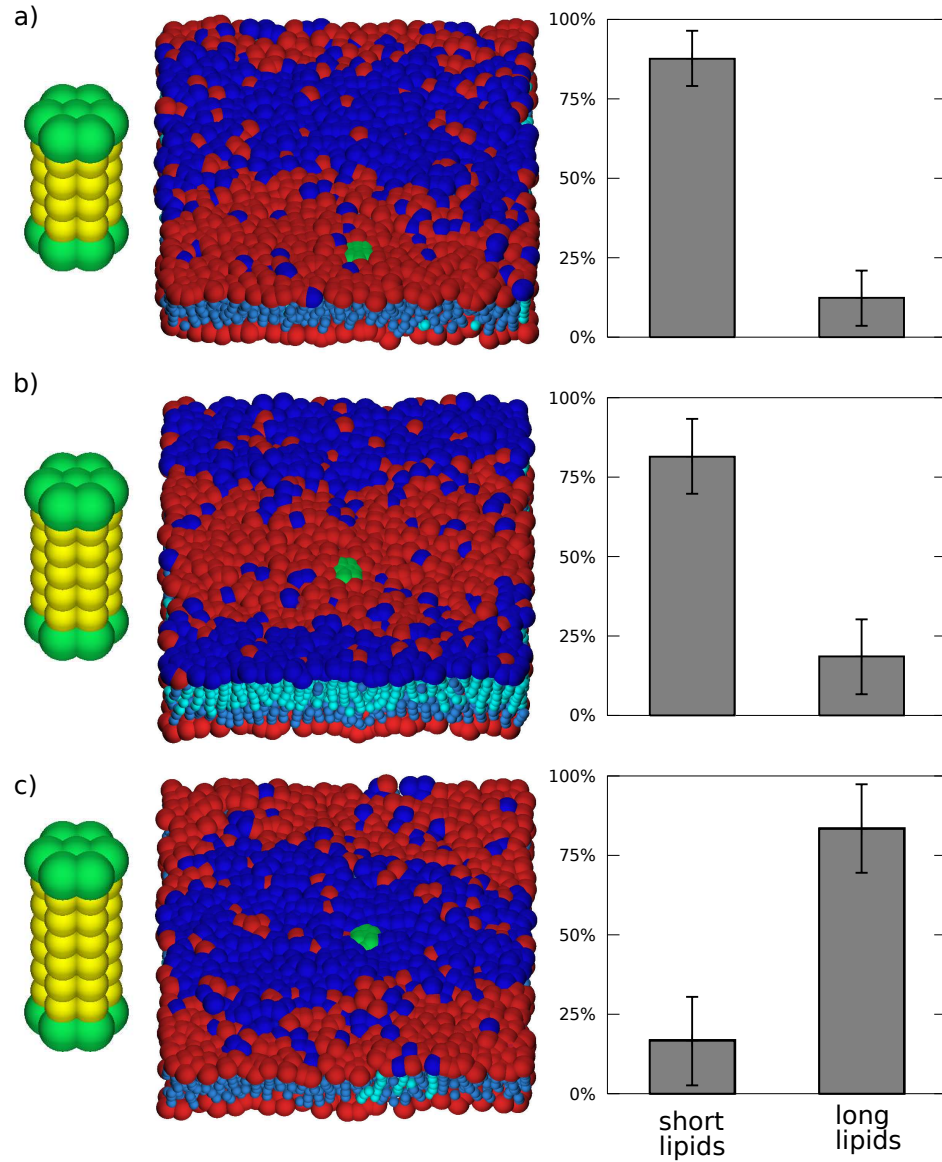


Figure 4.12: Pictures of proteins with $n = 4, 5, 6$ hydrophobic layers (from top) and representative snapshots of their steady-state configuration in a phase-separated lipid bilayer (lipid color coding as in Figure 4.11, proteins are colored green). Proteins with four or five transmembrane layers partition with high preference into the thin membrane domain while thicker proteins prefer the complementary domain. This is also reflected by the steady-state fraction of short and long lipids in the vicinity (radius of $4r_c$) of the embedded protein.

to specific motifs in the stalk and transmembrane region of the proteins. The resulting complexes are thus simply too large to enter transport vesicles and hence do not leave their compartment. This is in contrast to the membrane thickness model (Bretscher93).

According to the latter hypothesis, the length of a protein's transmembrane domain is the essential factor in correct protein localization. The TMD acts as a probe sensing the varying lipid thickness along the secretory pathway (Mitra04). The journey of the protein stops if the TMD matches best the local lipid environment. It is important to note that both models are not mutually exclusive and that both have been supported experimentally (Nilsson94; Munro95).

The key role of the length of the transmembrane domain was recognized as early as 1984 by Mouritsen & Bloom in their innovative 'mattress model' of lipid bilayers (Mouritsen84). Here, the retention of an integral membrane protein, whose TMD is either too long or too short compared to the surrounding lipid bilayer, is energetically unfavourable. We have seen in Section 4.4, that this difference triggers the diffusional partitioning of integral proteins into membrane domains yielding a smaller hydrophobic mismatch.

Moreover, TMD-dependent protein partitioning was either directly observed or indirectly derived in recent experiments corroborating the major role of the hydrophobic mismatch in the protein sorting process (Abrami08; Patterson08; Ronchi08).

A simple model for protein sorting

On the one hand, it is easy to imagine that an integral protein scans its local host membrane for more appropriate domains. On the other hand, a comprehensive explanation of the protein's ability to feel that a remote organelle may provide an environment with a smaller HM is lacking. In other words: how do proteins regulate their transport towards organelles with a more suitable lipid environment? How do bunches of chemical compounds orchestrate the sophisticated sorting machinery in such a way that they reach their proper destination?

Bearing in mind the different HM-related effects on the dynamical behaviour of transmembrane proteins, in particular protein clustering and segregation, we offer a model of how these phenomena may contribute to intracellular protein sorting and trafficking (cf. sketch in Figure 4.13).

Engulfing membranes of organelles along the secretory pathway show slightly different thicknesses reflecting varying contents of cholesterol and sphingolipids (vanMeer08). A given transmembrane protein may thus experience alternating hydrophobic mismatches during its odyssey along the secretory pathway. How this may help the protein to find its proper destination is now described.

As an example, a newly synthesized Golgi-resident glycosylation enzyme may feel

Hydrophobic mismatching

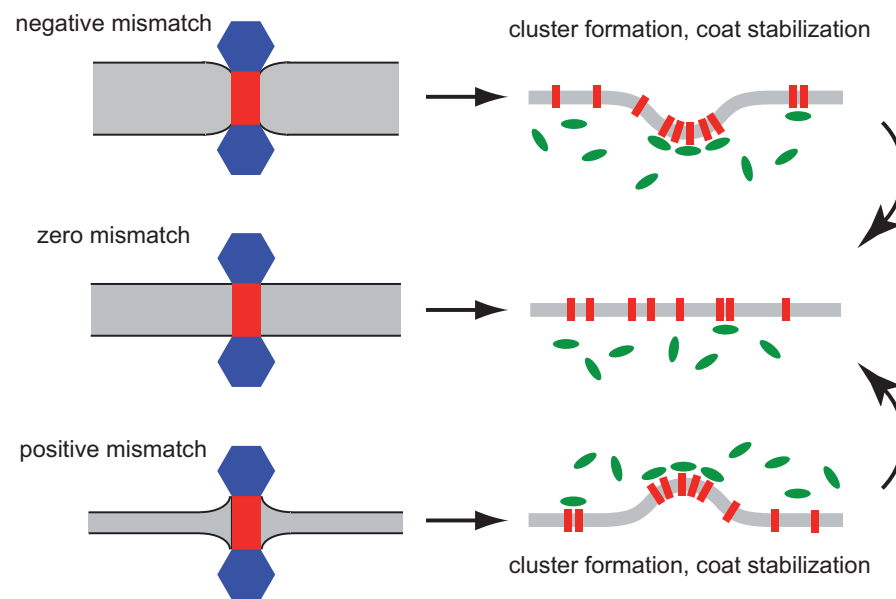


Figure 4.13: Model of how hydrophobic mismatching may facilitate transport of transmembrane proteins. If a HM (top: negative, bottom: positive) exists, clustering of transmembrane proteins is observed. These clusters can modulate the turnover rate of coat components (green ellipses) that shape an emerging vesicle at the locus of the protein cluster. This vesicle will be transported to a nearby compartment with a different membrane thickness where the protein may not experience a hydrophobic mismatch anymore (middle).

the surrounding ER membrane as too thin. Due to the positive hydrophobic mismatch, protein clusters emerge that are able to alter the local turnover rate of COPII proteins (Forster06), facilitating in this way the formation of COPII transport vesicles. The protein, and many other cargo, is packed into these transport vesicles that are released from the ER membrane.

After budding-off, the vesicle travels toward the Golgi apparatus and eventually fuses with the cis-most cisterna. Here, the present lipid environment may match well the desire of the transported protein, it does experience no or only a small hydrophobic mismatch. Consequently, the protein is not very prone to aggregate with like proteins.

However, cisternal maturation and lipid metabolism may soon lead to an increase in bilayer thickness resulting in a negative mismatch. Again, protein clusters start to emerge that now invoke and modulate the COPI machinery (Lanoix01; Weiß03b) for retrograde transport. In doing so, the protein escapes this unpleasant situation and tries to find a cisterna with a more appropriate lipid composition.

The ability to recognize different coat complexes may be mediated by specific cytoplasmic sequences attached to the corresponding transmembrane protein (Nilsson89). The problem of whether the two involved compartments, the ER and the Golgi apparatus, are able to conserve a distinct chemical identity during bi-directional transport, was resolved by a generic mechanism developed by Heinrich & Rapoport (Heinrich05).

One has to note that cisternal maturation is not a compulsory ingredient in the above described scenario. It is inevitable that proteins enter a transport vesicle that accidentally migrates towards an, regarding hydrophobic mismatching, even worse compartment. The vesicular transport model may then help to retrieve mislocalized proteins.

4.5.1 Numerical implementation of the sorting hypothesis

Given the above described simple model for protein sorting, one may ask for a simple implementation. In support of our model, further Monte Carlo (MC) simulations were performed in which the formation and loading of transport vesicles were modeled. We first give a short summary of the MC simulations and continue then with their results.

Monte Carlo simulations of vesicle formation

To simulate the effect of hydrophobic mismatching on vesicle formation and the steady-state secretory flux, we use lattice Monte Carlo simulations. Cargo and attached coat proteins are subject to diffusional motion on a 50×50 square

Hydrophobic mismatching

lattice with lattice constant $\Delta x = 10nm$. The diffusion coefficients of cargo and coat particles are set to $D_{crg} = 0.5\mu m^2/s$ and $D_{ct} = 0.25\mu m^2/s$, respectively. As open boundary conditions are used, a diffusive flux between the lattice boundaries and an external particle bath has to be implemented in order to guarantee a more or less constant particle density. For this purpose, we follow the approach given in (Geyer04; Gorba04). The time increment is set to $\Delta t = 40\mu s$. The so-established Monte Carlo lattice has approximately the size of a single ER exit site at which secretory COPII vesicles emerge.

The motion of cargo and coat particles is modeled via the blind ant algorithm (Majid84), i.e. particles are permitted to leave a lattice site with probability

$$P_{diff} = 4D\Delta t/\Delta x^2$$

towards one of the four neighboring sites. The parameter D is a wildcard for either D_{crg} or D_{ct} . An oligomeric size $M = 1, 2, 4, 8, 16$ is assigned to cargo particles, mimicking protein clusters of size M resulting from HM-induced attraction between individual proteins. According to the Saffman-Delbrück relation (Saffman75), diffusion of membrane inclusions depends only weakly on their size. Therefore, and for reasons of simplicity, we do not vary cargo diffusion coefficients with oligomeric size.

Coat proteins adsorb to and detach from individual lattice sites with rates k_A and k_D , respectively. As these rates can be regulated by the present amount of cargo (Lanoix01; Forster06), we choose the following relation

$$k_A = k_A^0 \cdot 1.09^{M-1} \quad \text{and} \quad k_D = k_D^0 \cdot 0.93^{M-1} \quad (4.16)$$

Consistent with previous reports, the values for the default attach- and detachment rates are chosen to be $k_D^0 = 10k_A^0 = 0.4/s$ yielding a typical residence time of COPII components in the range of a few seconds. In addition, adsorbed coat particles are allowed to irreversibly capture a single cargo particle (having multiplicity M) residing at the same grid point. Captured cargo follows the associated coat in its diffusion.

The diffusion of adsorbed coat particles is extended with an intrinsic aggregation ability. The tendency to aggregate is to stimulate the formation of bud-like structures representing transport intermediates of COPII type. According to the blind ant algorithm, for each site a direct neighbor site is randomly chosen. An exchange of the coat-contents of this pair of lattice sites occurs with probability

$$P_{MC} = P_{diff} \cdot \min\{1, \exp(-\Delta E/k_B T)\}$$

The first term simply accounts for the diffusional step whereas the second term involves the difference in compositional energy ΔE and the standard Metropolis

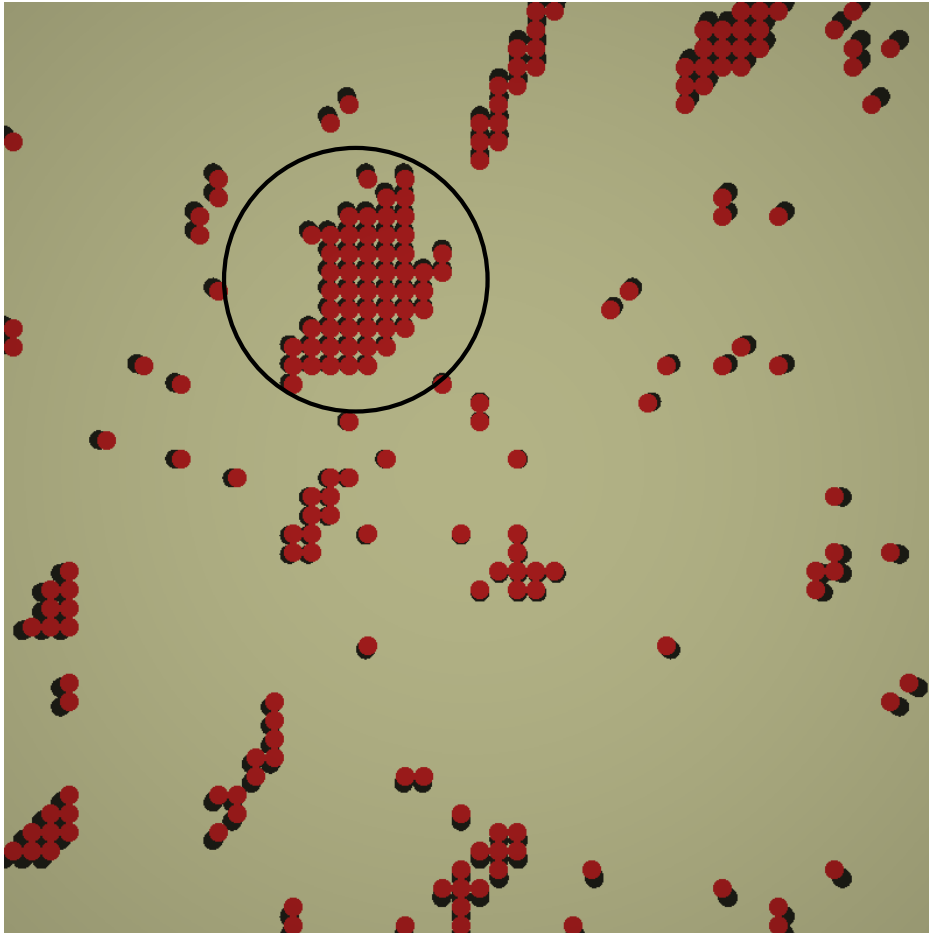


Figure 4.14: *Typical lattice configuration directly before a budding event: the encircled aggregate of coat particles (red circles) accommodates 55 coat particles and exhibits a more or less roundish shape. The underlying lattice is not drawn as are the diffusing cargo proteins. One can further recognize a couple of potential seeds for subsequent transport vesicles.*

Hydrophobic mismatching

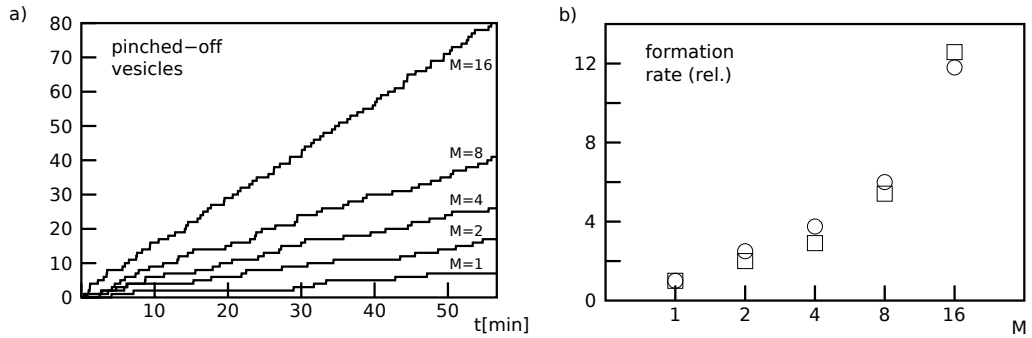


Figure 4.15: a) The number of produced vesicles increases with increasing oligomeric size of cargo proteins. b) The relative vesicle budding rates increase strongly with the oligomeric size. An amplification of up to tenfold is observed. Circles represent data from an exponential modulation of the exchange rates, squares from a linear modulation type.

criterion where ΔE depends on the individual binding energy we set to $\varepsilon = 2k_B T$. Coat contents are thus preferably exchanged if their swap creates an energetically more favorable configuration.

Larger assemblies of coat particles are interpreted as primers of COPII transport vesicles and are identified by using the Hoshen-Kopelman algorithm (Hoshen76). To bud off, these assemblies are restricted to incorporate more than 50 coat particles *and* to display a more or less roundish shape. An aggregate is assumed roundish if the average number of direct neighbors occupied with coat exceeds the value 3.3. The numerical value of 50 coat particles is adopted from experimental studies on the structure of these vesicular carriers (Stagg06)

To have a fair comparison, we fix the total (average) amount of cargo proteins on the lattice to $\langle N_P \rangle = 2500$, meaning that the number of cargo clusters is on average $\langle N_P \rangle / M$. Figure 4.14 displays a typical lattice configuration directly before a budding event.

We monitor for $T = 4000s$ real time several quantities, including number, size and cargo content of formed vesicles for different oligomeric sizes M . From the total number of produced vesicles, we derive via simple linearization the rate with which vesicles are released from our model ER lattice. As a benchmark, we first inspect the budding rate for monomeric cargo. Here, 9 pinched-off vesicles are observed yielding a budding rate of 0.13 vesicles per minute. Figure 4.15 displays the total number of produced vesicles and the derived budding rates normalized to the monomeric case.

For all oligomeric sizes M , an increase in the number of pinched-off vesicles is observed resulting in a likewise increase of the budding rates. While the bud-

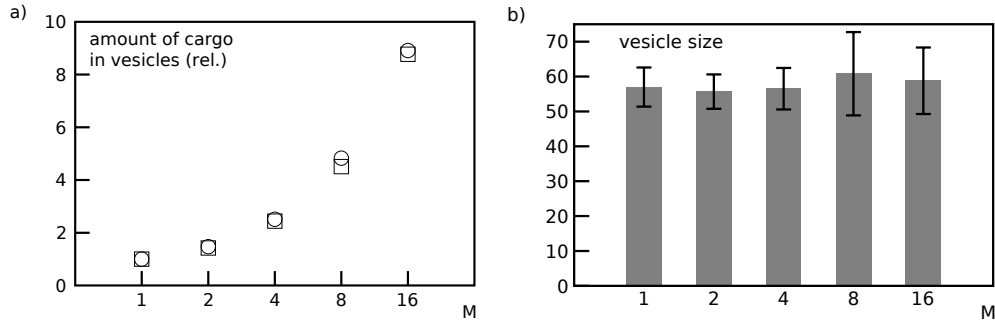


Figure 4.16: a) The relative amount of cargo is greatly amplified for increasing oligomeric size M . For $M = 1$ the basal amount of cargo is 112. Data is presented for an exponential (circles) and a linear (squares) modulation type of the exchange rates. b) The average size of transport vesicles nearly stays constant and is consistent with previous reports on the structure of the COPII complex.

ding rate for monomeric and dimeric cargo nearly coincides, it steeply increases when M is increased beyond $M = 4$. For $M = 16$, the largest oligomeric size considered here, the budding rate is more than tenfold compared to the case of monomeric cargo. Thus, a tremendous amplification in vesicle formation and hence membrane flux is observed if the oligomeric size M is varied.

We next inspected the amount of transported cargo for varying multiplicity M . The basal amount of cargo if monomers are present on the lattice is 112 cargo units per vesicle. The transport capacity steadily increases showing a maximal amplification of a factor of 9 for $M = 16$ (see Figure 4.16a).

The assembled coat patches from which vesicles are thought to emerge have on average the same size for all oligomeric multiplicities M . In fact, this is a direct consequence from our simulation model. We determine the average vesicle size to be roughly 56 ± 6 coat particles (cf. Figure 4.16b).

To investigate the robustness of our numerical data, we chose to alter the coat's attachment and detachment rate in a linear instead of an exponential manner according to

$$k_A = k_A^0 \cdot (1.02 - M \cdot 0.05) \quad \text{and} \quad k_D = k_D^0 \cdot (0.83 + M \cdot 0.19)$$

Although the numerical values in the upper equation do seem quite arbitrary, they are chosen in such a way to approximate the exponentially modulated exchange rates for the limiting values of M . This change did not result in significant deviations from the above results. Solely the budding for $M = 16$ showed a slightly larger value, values for transported cargo and vesicle size was not altered. Data for this modulation type is depicted in Figures 4.15b and 4.16a.

Hydrophobic mismatching

M	N_M	$B_M[1/min]$	B_M/B_0	C_M	C_M/C_0	size
1	9	0.13	1.0	112	1.00	57
2	17	0.26	2.0	165	1.47	55
4	26	0.45	3.5	281	2.51	56
8	41	0.69	5.3	542	4.83	60
16	81	1.45	10.6	998	8.91	58

Table 4.2: Summary of numerical values for $D_{ct} = 0.25\mu m^2/s$ and an exponential modulation of attachment and detachment rate. The entries correspond to (from left to right): oligomeric size, total number of produced vesicles, absolute budding rate, relative budding rate, absolute amount of cargo, relative amount of cargo and vesicle size.

During a third simulation series, the diffusion coefficient for coat particles was lowered to $D_{ct} = 0.1\mu m^2/s$. Again, a steady increase in budding rates and transported amount of cargo with oligomeric size was observed irrespective of the modulation type (exponential or linear). However, the basal flux with these settings was unphysiologically low. Table 4.2 summarizes the numerical data for $D_{ct} = 0.25\mu m^2/s$ and the exponential modulation of the exchange rates. The above presented results thus support the hypothesis that protein clustering originating from hydrophobic mismatching can stimulate and enhance the secretory flux in terms of membrane and transported cargo proteins. This improvement originates from the ability of cargo proteins to alter the local turnover rate of coat components. It is therefore conceivable that proteins can arrange for a nearby formation of transport intermediates to shuttle to a remote organelle.

Chapter 5

Diffusion of oligomers

In the preceding chapter we discussed that hydrophobic mismatching of trans-membrane proteins stimulates oligomerization/clustering. The resulting protein clusters are very dynamic entities displaying a constant exchange of single proteins with the host membrane and diffusively driven aggregation with other clusters. Indeed, the formation of higher-order structures is a frequent process of trans-membrane proteins facilitating their function and helping to assume proper sub-cellular localization (Schuck04; Park04). However, oligomerization alters the diffusion properties of the participating individual proteins. Our aim in this chapter is to analyse the diffusion behaviour of protein complexes that are the result of an oligomerization process.

Before we concentrate on our simulational setup, we briefly summarize how diffusion processes can be described mathematically and present key quantities that help to characterize diffusional motion.

5.1 Diffusion in a nutshell

The thermally driven motion of a particle in solution is non-directional and stochastic. The irregularity in its movement is due to thermal random kicks by the solvent molecules and the path of the suspended particle can be classified as a random walk. In the simplest case, a one dimensional random walk, a tracer particle moves a distance δx to the left or to the right during a certain time interval Δt . Usually, the probability for a step to the left or to the right is assumed to be equal and denoted by $p = 1/2$. The probability to find the tracer particle after n time steps k steps remote from its starting point is given by a binomial distribution whose general formula reads

$$B(p, n, k) = \binom{n}{k} p^k (1 - p)^{n-k} \quad \text{with} \quad \binom{n}{k} = \frac{n!}{k!(n-k)!} \quad (5.1)$$

Diffusion of oligomers

The mean and variance of $B(p, n, k)$ are $\mu = np$ and $\sigma^2 = np(1-p)$, respectively. In the limit of $n \rightarrow \infty$, $p \rightarrow 0$ and μ finite, the binomial distribution converges to a Gaussian, or normal, distribution. Incorporating a random walk's character into the latter description, one arrives at the following formula to find the tracer particle at time $t > 0$ a distance x remote from its starting point

$$P(x, t) = \frac{1}{(4\pi Dt)^{-d/2}} \cdot e^{-\frac{x^2}{4Dt}} \quad (5.2)$$

Here, we already accounted for the Euclidean dimension d of the space in which the random walk is embedded in. The parameter D is the *diffusion coefficient* of the tracer particle; its unit is $\left[\frac{\text{length}^2}{\text{time}}\right]$. It is a measure of the mobility of the tracer particle that is determined by the temperature T and the viscosity η of the solvent. The *Einstein-Stokes* equation relates the diffusion coefficient D of a spherical body (radius R) to temperature, viscosity and particle size as (Einstein05)

$$D = \frac{k_B T}{6\pi\eta R} \quad (5.3)$$

Another way to obtain Equation 5.2 is to interpret diffusing particles from a macroscopic point of view. Their stochastic motion leads to the balancing of particle gradients. Fick's first law (Fick55) describes the particle flux \mathbf{j} that originates from a concentration gradient ∇C as

$$\mathbf{j} = -D \cdot \nabla C$$

Here, the factor D also denotes the diffusion coefficient. Combining the latter equation with the continuity equation (mass conservation) $\partial_t C = -\nabla \cdot \mathbf{j}$ gives the diffusion equation (Fick's second law)

$$\partial_t C = D \nabla^2 C \quad (5.4)$$

The solution to this second-order partial differential equation is given by its Green's function or propagator. The special initial condition $C(0, 0) = \delta(0, 0)$ possesses the following propagator of the diffusion equation

$$C(x, t) = \frac{1}{(4\pi Dt)^{-d/2}} \cdot e^{-\frac{x^2}{4Dt}} \quad (5.5)$$

Hence, the time evolution of the δ -distribution is given by a Gaussian propagator. It is identical to Equation 5.2 thus connecting the spreading of particle concentration with the diffusion of a single tracer.

Coming back to the probability distribution, Figure 5.1 displays $P(x, t)$ at different times t with the initial condition $P_0 = \delta(t)$. One clearly sees that the

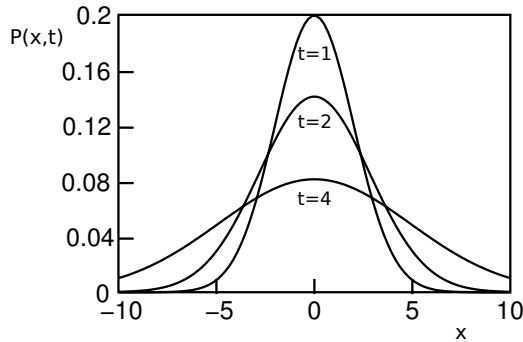


Figure 5.1: One-dimensional probability distribution $P(x, t)$ for different times t . The diffusion coefficient was set to $D = 4$, the initial condition was $P(0, 0) = \delta$. The probability to find the tracer particle remote from the origin increases with time.

probability to find the tracer particle remote from the origin increases for later times t .

Since $P(x, t)$ is a probability distribution, one is usually interested in its first and second moment of the spatial variable x , i.e. its mean and variance, respectively. These can be computed easily and read

$$\langle x \rangle = 0 \quad \text{and} \quad \langle x^2 \rangle = 2Dt \quad (5.6)$$

Associated with diffusional motion, the second moment is also termed *mean-square displacement* (MSD) and increases, for normal diffusion, linearly with time. A more general form of the mean-square displacement involves an additional parameter α that is a measure for the degree of anomaly of the diffusion process. The expression for the second moment changes accordingly to

$$\langle x^2 \rangle = 2Dt^\alpha$$

A diffusion process is termed anomalous if the parameter α deviates from unity. If $\alpha < 1$ the motion is called *sub-diffusive* while for $\alpha > 1$ it is termed *super-diffusive*. $\alpha = 1$ reproduces normal diffusion behaviour. We note here that anomalous diffusion processes can, in general, not be described by a Gaussian propagator (Metzler00; Bouchaud90).

Random processes responsible for sub-diffusion can be grouped into two categories: those that are associated with stationary increments and those that arise from non-stationary increments. Examples from the first category are fractional Brownian motion (fBM) or percolation, while a continuous time random walk (CTRW) falls into the second class (Szymanski09). As a consequence, a CTRW shows a weak ergodicity breaking.

5.1.1 Diffusion of membrane inclusions

Being integrated into a lipid bilayer, membrane inclusions perform two-dimensional diffusion. In the last chapter we have seen that hydrophobic mismatching can

Diffusion of oligomers

lead to a pronounced protein aggregation. While the origins of protein oligomerization can be manifold, it is beyond question that the shape of the emerging oligomer determines distinct biophysical properties like the diffusion coefficient D .

Experiments have used the diffusion coefficient to characterize the oligomeric state of proteins (Cole96) as the diffusion coefficient depends on the radius R of the oligomers. However, diffusion in a membrane does not yield the simple relation $D \propto 1/R$ found for bulk solutions. Instead, a logarithmic dependence of D on R is found (Saffman75) for radii $R \lesssim 10nm$

$$D = \frac{k_B T (\ln [h\eta_m/(R\eta_c)] - \gamma)}{4\pi\eta_m h} \quad (5.7)$$

Here, h is the membrane thickness, R the lateral radius of the membrane inclusion, $\gamma \approx 0.5772$ is Euler's constant, and η_m, η_c are the viscosities of the membrane and the adjacent fluid, respectively. Recent computer simulations found that the above expression is valid for small radii and turns into a power-law behaviour for larger values of R (Guigas06).

In addition, the shape of the oligomer may not be circular but may rather have the shape of a (branched) polymer (cf. Figure 5.2). This further complicates the interpretation of measured diffusion coefficients in terms of an oligomeric radius. Furthermore, recent studies frequently report that diffusion on cellular membranes exhibits an anomalous characteristic (Schutz97; Weiß03a). To be precise, membrane inclusions show sub-diffusive behaviour, that is the mean-square displacement grows qualitatively slower than for normal diffusion.

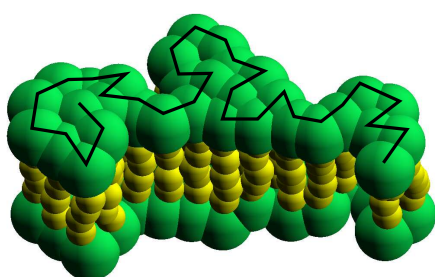


Figure 5.2: Model of a linear oligomer consisting of 32 monomers with five transmembrane layers (yellow). Hydrophilic groups are colored green and enhanced for better visibility, the solid line highlights the random coil conformation.

A suitable approach to this problem is to interpret the oligomeric entities as linear polymers with their sub-units being individual proteins. The dynamics of polymers is described by Rouse or Zimm theory (cf. Chapter 2). We therefore summarize theoretical predictions for the motion of polymers in two dimensions, before we continue with the presentation of our results.

5.1.2 Diffusion properties of polymers

Chapter 2 introduced Rouse and Zimm theory as two models that describe the dynamics of polymers. The difference between the models is that the Rouse model neglects hydrodynamic interactions while the Zimm model takes these explicitly into account. Consequently, different scaling laws for important quantities are obtained. Furthermore, the scaling behaviour is not exclusively dependent on the theoretical description but is also influenced by the dimension of the Euclidean space the polymer is embedded in.

The parameters we are mainly interested in are the mean-square displacement of the individual monomers as well as of the polymer's center of mass and, connected to the latter, the apparent diffusion coefficient of the center of mass. In the following, we denote these quantities by $\langle \Delta x^2 \rangle$, $\langle \Delta x_{cm}^2 \rangle$ and D_{cm} , respectively. In addition, the radius of gyration, R_g , also occurs in the subsequent discussion. In the dilute limit the diffusion coefficient of the center of mass and the radius of gyration follow a scaling behaviour

$$D_{cm} \propto N^{-\nu_D} \quad \text{and} \quad R_g^2 \propto N^{2\nu} \quad (5.8)$$

Here, N denotes the number of monomeric subunits. The Flory exponent ν involves the Euclidean dimension d and is given by

$$\nu = \frac{3}{2 + d}$$

An important result of the Zimm model is that, in two dimensions, the center of mass diffusion coefficient is expected to be independent of the polymer size, i.e. $\nu_D = 0$. In contrast, Rouse theory predicts a pure reciprocal dependence of the center of mass diffusion coefficient on the degree of polymerization, that is, $\nu_D = 1$. The latter relation is valid in two and in three dimensions. Moreover, the scaling exponent of the two-dimensional radius of gyration is $\nu = 3/4$, irrespective of the chosen model.

Rouse and Zimm theory also provide a prediction of the scaling for the mean-square displacement of the individual monomers. In the limit of $t \rightarrow \infty$, the monomer MSD is expected to show normal diffusion behaviour in both models. This is reasonable since after a certain time the movement of the individual monomers defines the center of mass motion that always grows linearly in time, i.e. shows normal diffusion.

At shorter times, the scaling of monomer mean-square displacement does depend on the chosen polymer model. Neglecting hydrodynamics leads to a dependence of the scaling on the fractal dimension (d_f) of the polymer while taking into account hydrodynamic interaction results in a Euclidean dimension-dependent

Diffusion of oligomers

	$D_{cm} \propto N^{-\nu_D}$	$R_g \propto N^\nu$	$\langle \Delta x^2 \rangle \propto t^\alpha$
Rouse	$\nu_D = 1$	$\nu = 3/4$	$\alpha = 3/5$
Zimm	$\nu_D = 0$	$\nu = 3/4$	$\alpha = 1$

Table 5.1: *Scaling behaviour for the center of mass diffusion coefficient D_{cm} , the radius of gyration R_g and the monomer MSD $\langle \Delta x^2 \rangle$ as predicted by Rouse and Zimm theory in two dimensions.*

(d) scaling behaviour (Zilman98). The numerical values of the scaling exponent α in two dimensions are given by

$$\alpha = \begin{cases} 2/(2 + d_f) & = & 3/5 & \text{Rouse} \\ 2/d & = & 1 & \text{Zimm} \end{cases} \quad (5.9)$$

Hence, Rouse behaviour leads to a distinct sub-diffusive character of the monomer motion while the Zimm model predicts the monomers to diffuse normally. Table 5.1 summarizes the scaling behaviour of the various quantities in two dimensions. Although these theoretical predictions are supported by various computer simulations, experiments with single- and double-stranded DNA have led to differing results concerning the question which polymer theory is most appropriate to describe the diffusing DNA polymer (Maier98; Shusterman04). Making matters worse, even computer simulations come to varying results regarding the scaling of the center of mass diffusion coefficient. While some authors support $\nu_D = 0$ (Falck03), others predict even a breakdown of the scaling behaviour (Shannon97) in two dimensions. Thus, the question whether Rouse or Zimm theory is applicable to these cases remains unsolved.

5.2 Dynamics of oligomers

Trying to resolve the above mentioned inconsistency, we apply dissipative particle dynamics computer simulations to model oligomers integrated into lipid membranes. The motion of the oligomeric complexes is thoroughly analysed and the results are compared with theoretical predictions.

5.2.1 Simulational setup

Following the spirit of the last chapter, we model oligomers of different size and with different hydrophobic mismatch, the latter may account for the now permanent connection between the individual proteins. In other words, a model

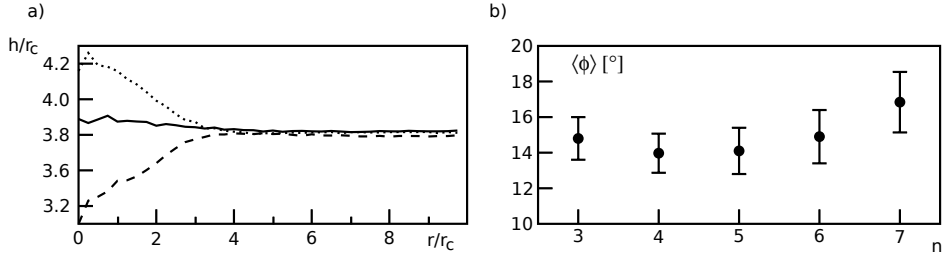


Figure 5.3: a) Membrane thickness profile as a function of the distance from the center of mass of an oligomer of size $N = 16$ for different hydrophobic mismatches $n = 4, 5, 6$ (dashed, solid, dotted line). b) The oligomer tilt angle hardly varies with the number of transmembrane beads n .

protein is represented as a linear chain of n hydrophobic beads completed on each end with a single hydrophilic bead. Oligomers are obtained by linking these monomer prototypes by lateral harmonic bonds. Figure 5.2 displays such a model oligomer with $n = 5$ transmembrane parts and a total of 32 protein monomers. These oligomers are embedded into a fully-hydrated homogeneous lipid bilayer made of HT_3 lipids and their diffusional motion is recorded.

Simulations are carried out for different hydrophobic mismatches, i.e. different numbers n of hydrophobic DPD beads. Similar to the last chapter, we choose $n = 4, 5, 6$, i.e. oligomers with negative, negligible and positive mismatch, respectively. Oligomers of size $N = 4, 8, 16, 32$ are used to investigate the scaling behaviour of the center of mass diffusion coefficient. The lateral size of the simulation box is set to $L = 20r_c$, in case of $N = 32$ the size is set to $L = 25r_c$. After an equilibration period, data is collected for 1.5×10^6 DPD time units from which mean-square displacements and diffusion coefficients are calculated.

Mismatch and tilt of oligomers

At first, we tested whether our model oligomer follow a similar hydrophobic mismatching behaviour as the hexagonal protein described in the last chapter. To this end, we analysed the average membrane thickness dependent on the distance from the oligomer's center of mass. Figure 5.3a displays the radial thickness profile for oligomers of size $N = 16$ and varying hydrophobic mismatch.

Far away from the center of mass, the membrane thickness adopts its unperturbed value for all hydrophobic mismatches. At a critical distance of $r^* \approx 4r_c$, the presence of the integrated oligomer starts to influence the thickness of the lipid bilayer. One observes a compression or a stretching of the membrane thickness for oligomers with negative or positive hydrophobic mismatch, respectively.

Diffusion of oligomers

As before, an oligomer with $n = 5$ hydrophobic beads hardly influences the membrane thickness. The integration of oligomers of larger or smaller size N only affected the critical distance below which the membrane experienced a deformation. As expected, r^* increases with increasing oligomeric size.

Inspecting the oligomer tilt angle $\langle\phi\rangle$ with respect to the bilayer normal surprisingly reveals that all oligomers are nearly upright integrated into the lipid bilayer. One observes a slightly increased tilt angle for oligomers with $n = 7$ transmembrane beads, but it is by far not as pronounced as compared to the case of hexagonal proteins. The decreased tendency to tilt may be connected with the lacking lateral bending rigidity. The absence of the latter provides the oligomers with a certain flexibility, in contrast to the extremely rigid protein hexagons from the preceding chapter.

We conclude, that our model oligomers display the expected dependence of their hydrophobic mismatch on the size of their transmembrane domain. An important point here is that the oligomers are not as rigid as hexagonal proteins preventing their tilting with respect to the bilayer normal.

Oligomeric radius of gyration

As stated above, the radius of gyration of a two-dimensional polymer exhibits a scaling dependence on the polymer size that is given by

$$R_g \propto N^{3/4}$$

This relation is valid for both, the Zimm and the Rouse model. To check whether our DPD oligomers also show the latter scaling if one projects the monomer coordinates onto the xy plane, we calculated the corresponding two-dimensional radius of gyration for different degrees of oligomerization and for different hydrophobic mismatches. These results are depicted in Figure 5.4.

As expected, the radius of gyration increases with increasing oligomer size N irrespective of the number of transmembrane beads n . However, the scaling of R_g varies with the hydrophobic mismatch. Oligomers with $n = 4, 6$ exhibit a weaker scaling than their counterparts with $n = 5$ which is supported by a power-law fit. For $n = 4, 6$ the numerically obtained value of the scaling exponent is $\nu \approx 0.55$ while for $n = 5$ one finds $\nu = 0.66$ which is close to the theoretical value of $3/4$.

The significant deviations observed for oligomers with $n = 4, 6$ can be traced back to their non-vanishing hydrophobic mismatch. Bearing in mind that proteins with a hydrophobic mismatch aggregate in order to minimize the contact surface with the lipid environment, the oligomers behave in the same way. Hence, one cannot regard these oligomers as random coils but they rather approach the molten

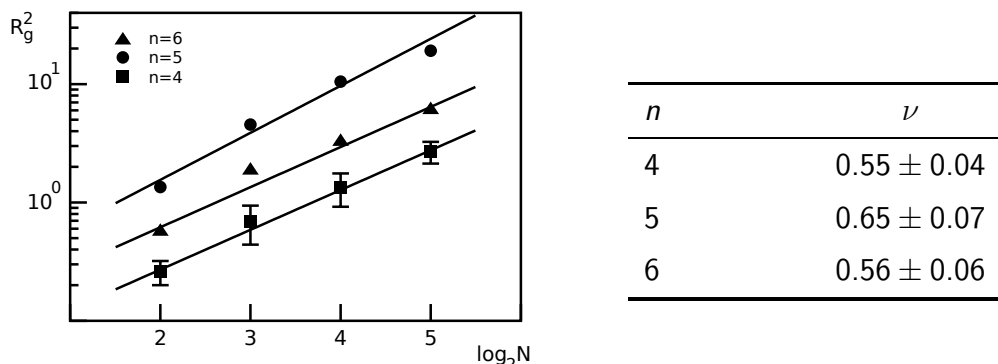


Figure 5.4: Squared radius of gyration (left) and corresponding scaling exponent as obtained by a power-law fit (right). While the scaling exponent for oligomers with a negligible HM is very close to the theoretically predicted value of $\nu = 3/4$, deviations are observed for oligomers with non-vanishing HM. Data for $n = 6$ and $n = 5$ have been shifted by a factor of 2 and 5 for better visibility; errorbars for $n = 5, 6$ are of symbol size.

globule state. Consequently, the scaling behaviour of the radius of gyration has to change.

The numerical fit with which the scaling exponent was determined included all calculated values of R_g and the corresponding errors. Taking into account that statistics get worse with increasing oligomer size, one could have also excluded the values of $N = 32$ from the fitting range. Adjusting the power-law in this way yields an increase of the scaling exponent for all n and a perfect agreement with the theoretical value for $n = 5$ (data not shown).

Having discussed static variables, we now address the dynamics of the oligomers and their individual subunits. We calculate the two-dimensional mean square displacement of the monomers, $\langle \Delta x^2 \rangle$, and that of the oligomer's center of mass, $\langle \Delta x_{cm}^2 \rangle$. From the latter quantity, we derive the diffusion coefficient and test whether it exhibits Rouse or Zimm scaling behaviour.

5.2.2 Diffusive motion of oligomers

To experimentally probe the dynamical state of intracellular macromolecules, fluorescence techniques like FRAP (fluorescence recovery after photo-bleaching (Axelrod76)) or FCS (fluorescence correlation spectroscopy (Magde72)) are usually the methods of choice. They offer an elegant way to determine quantitative information such as diffusion coefficients, average concentrations or chemical reaction rates. A nice introduction to FCS and its applications is given by Schwille et al. (Schwille09).

Regarding the problem of sub-diffusive behaviour of oligomers, it is worth noting

Diffusion of oligomers

that these fluorescence techniques monitor the diffusional properties of the individual proteins rather than the properties of the oligomeric entity. Consequently, a first point is to probe the diffusional motion of the single monomers. The mean-square displacement of the individual monomers $\langle \Delta x^2(t) \rangle$ is calculated as a time and ensemble average according to the following formula

$$\langle \Delta x^2(t) \rangle = \frac{1}{N} \sum_i \sum_t [x_i(t_0) - x_i(t_0 + t)]^2 \quad (5.10)$$

The combination of a time and ensemble average has the major advantage that the resulting MSD curves are very smooth, i.e. they do hardly fluctuate as compared to an ordinary ensemble average. For the calculation of the mean square displacement only the hydrophilic parts at the top and bottom of the oligomer are taken into account. This is justified by the fact that fluorescent probes that are used to monitor the dynamics of transmembrane proteins are exclusively attached at these regions, i.e. no fluorescence signal is emitted from within the lipid bilayer. Indeed, including the hydrophobic transmembrane beads in the analysis of the mean-square displacement does not alter the numerical results.

Monomer diffusion

A common way to visualize MSD data is to divide out the leading order in time, that means

$$\langle \Delta x^2(t) \rangle \longrightarrow \langle \Delta x^2(t) \rangle / t \quad \Rightarrow \quad \langle \Delta x^2 \rangle / t \propto t^{\alpha-1}$$

This reduced data is now better suited to resolve a bunch of MSD curves and to highlight any value $\alpha \neq 1$ of the anomaly index. The scaling exponent is now assumed to be $\alpha - 1$. Figure 5.5 displays snapshots of oligomers with $n = 4, 5, 6$ and $N = 32$ (left column), and the reduced MSD data for different oligomeric size N (right column).

Inspecting the reduced MSD curves of the individual monomers, one can distinguish two temporal regimes that are characterized by different shapes of the MSD curves. The first regime is restricted to $t \lesssim 10^3$, the reduced MSD data show here a pronounced sub-diffusive character as is visible by the slope of the curve in the double-logarithmic plot. Thus, the monomer motion indicates Rouse-like behaviour that is characterized by sub-diffusion (cf. Table 5.1) in contrast to Zimm-like behaviour. Interestingly, the length of the time interval in which the monomers show sub-diffusion hardly varies with the oligomer's size or its hydrophobic mismatch (cf. Figure 5.5, dotted line). Presumably, the investigated values of N are too small to highlight a dependence on the oligomer size at these time scales.

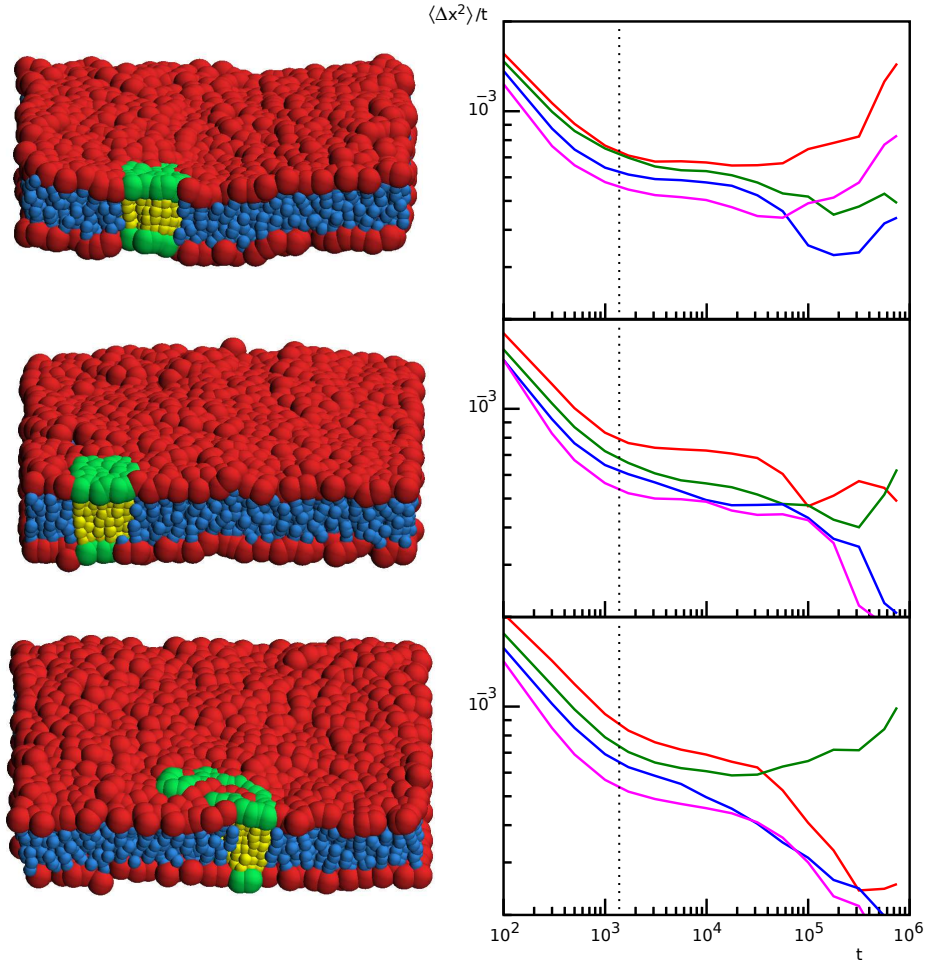
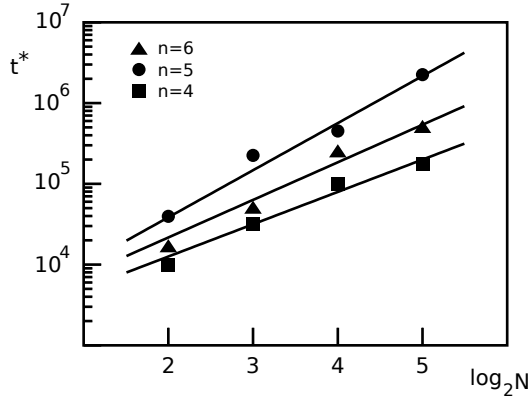


Figure 5.5: Left: snapshots of oligomers of size $N = 32$ and with $n = 4, 5, 6$ hydrophobic transmembrane beads (from top). Right: reduced monomer MSD curves (DPD units) for $N = 4, 8, 16$ and 32 (red, green, blue, magenta) and n as denoted on the right. The dotted vertical line approximates the boundary between the two temporal regimes. In the left column, lipids are colored red (head) and blue (tail), hydrophilic parts of oligomers are colored green, transmembrane beads in yellow. Note the various oligomer configurations! All units in the right column are intrinsic DPD units.

Diffusion of oligomers



n	β
4	1.32 ± 0.16
5	1.93 ± 0.28
6	1.54 ± 0.30

Figure 5.6: The time t^* after which monomeric motion is indistinguishable from center of mass motion increases with oligomeric size N . A power-law fit reveals that the scaling of t^* varies with hydrophobic mismatch n . For better visibility, data for $n = 6$ (triangles) and $n = 5$ (circles) have been shifted by a factor of 1.5 and 4, respectively.

In the second regime, the slope of the reduced MSD curves varies continually until it eventually settles at $\alpha \approx 1$. This is reasonable since, when time increases, the monomeric mean-square displacement approaches and finally coincides with that of the center of mass. To approximate the time point t^* at which center of mass motion is dominated by monomeric diffusion, we calculated the relative difference δ between the mean-square displacement of the monomers and of the center of mass

$$\delta(t) = \frac{|\langle \Delta x^2 \rangle - \langle \Delta x_{cm}^2 \rangle|}{\langle \Delta x_{cm}^2 \rangle}$$

The time t^* was taken to be that time point at which the relative difference is smaller than 10%, i.e. $\delta(t^*) \leq 0.1$. We have to admit that this procedure yields only a very rough estimate of t^* and the uncertainties in t^* are very large. Nevertheless, it provides evidence that the transition from individual monomeric motion to collective center of mass motion is shifted to later times if the size of the oligomer is increased. Moreover, a power-law fit underlines that a negligible HM is responsible for a stronger dependence on the oligomeric size compared to a positive or negative HM. Figure 5.6 depicts the individual curves for t^* dependent on the hydrophobic mismatch, the adjacent table summarizes the scaling exponents as obtained by a power-law fit, $t^* \propto N^\beta$.

Table 5.2 summarizes the numerically obtained values of the anomaly index α in the various temporal regimes for all investigated size N and all hydrophobic mismatches n . The numerical values of α in the time interval in which individual monomer motion dominates the shape of the MSD curves are almost exclusively near to $\alpha = 2/3$. Oligomers of size $N = 32$ with negligible and posi-

HM	oligomeric size N			
$n = 4$	4	8	16	32
α	0.67(1)	0.68(2)	0.64(3)	0.63(3)
	0.99(1)	0.93(1)	0.91(1)	0.95(1)
$n = 5$	4	8	16	32
α	0.65(1)	0.64(2)	0.62(3)	0.54(4)
	0.92(1)	0.92(1)	0.92(1)	0.95(1)
$n = 6$	4	8	16	32
α	0.66(1)	0.64(2)	0.62(3)	0.57(4)
	0.86(1)	0.96(1)	0.84(1)	0.90(1)

Table 5.2: *The scaling exponent of the monomer MSD displays a transition from sub-diffusive behaviour ($\alpha < 1$) at short times to normal diffusion ($\alpha \approx 1$) at later times. The anomaly index α in each time interval does interestingly depend only marginally on the kind of hydrophobic mismatch (n) and on the degree of oligomerization (N).*

tive hydrophobic mismatch show slightly smaller values that are around $1/2$. A systematic change of α with oligomer size N or hydrophobic mismatch n is not observed.

Surprisingly, small oligomers, i.e. $N = 4, 8$, show the same degree of anomaly in their diffusional motion as their larger counterparts. This is somewhat counter-intuitive; especially for $N = 4$ one would have expected a value of α closer to unity since these oligomers are to be most likely related to single monomers.

To conclude the part on monomeric diffusion, our simulational data show a distinct sub-diffusive behaviour of the mean-square displacement of the individual monomers at short time scales. The degree of anomaly hardly varies with oligomeric size N and the number of hydrophobic transmembrane beads n : $\alpha \approx 0.55 - 0.67$. The observation of sub-diffusion indicates that the individual oligomers show Rouse behaviour, Zimm-like motion is not observed. At longer times, the monomeric MSD curves evolve into collective center of mass motion. The larger the oligomer, the longer this transient regime.

Center of mass diffusion

The analysis of the center of mass diffusion is also based on the corresponding mean-square displacement curves. Data for the center of mass mean-square

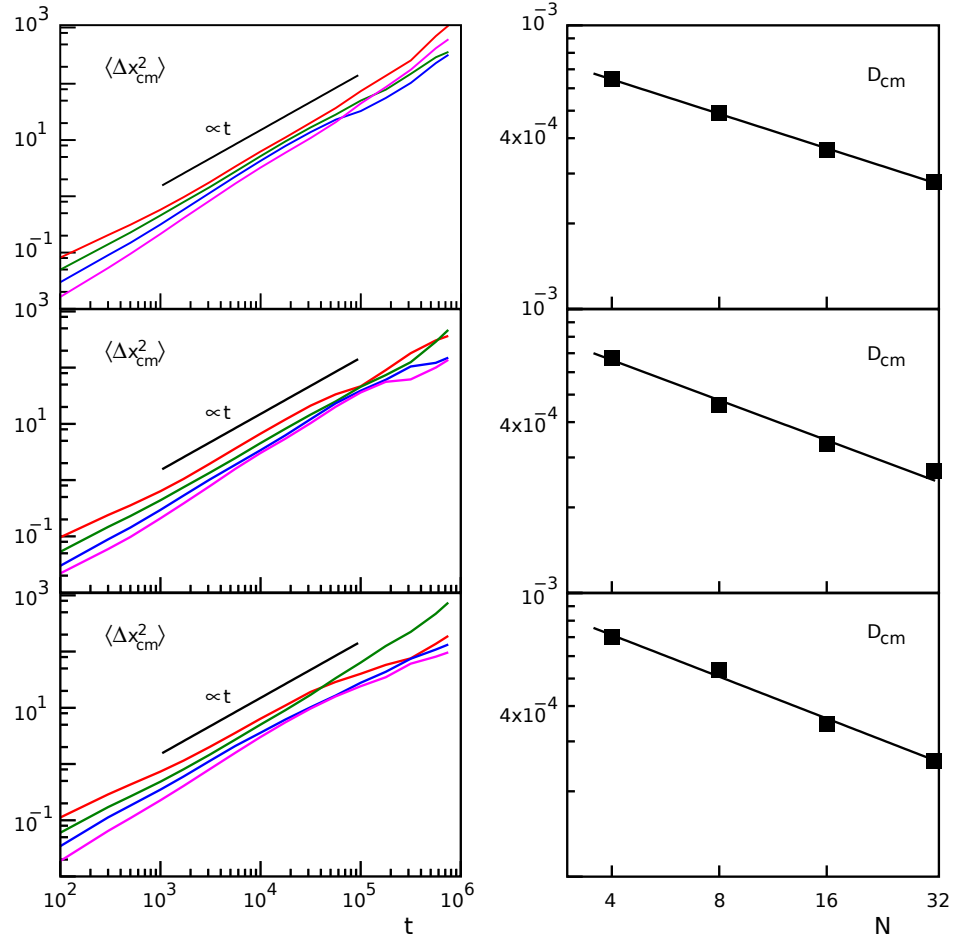


Figure 5.7: Left: mean-square displacement of the center of mass, $\langle \Delta x_{cm}^2 \rangle$, of oligomers with $n = 4, 5, 6$ transmembrane layers (from top). The curves in the individual plots represent the MSD for different oligomeric size $N = 4, 8, 16, 32$ (red, green, blue, magenta). The solid, black curves represent a linear reference function. Right: the linear form of the center of mass MSD curves allows to derive a diffusion coefficient that exhibits a power-law dependence on the oligomeric size N . Note the double-logarithmic plot style!

HM	oligomeric size N				ν_D
	4	8	16	32	
$n = 4$	1.07(3)	1.00(1)	1.02(1)	1.06(3)	0.42(3)
$n = 5$	0.98(2)	1.00(1)	0.99(1)	1.01(2)	0.47(4)
$n = 6$	0.95(2)	1.03(2)	0.97(2)	1.03(2)	0.49(4)

Table 5.3: *The mean-square displacement of the oligomers' center of mass always exhibits normal diffusion behaviour as indicated by $\alpha \simeq 1$. The derived diffusion coefficient is well described by a power-law with exponent ν_D (most right column) whose value is nearly universal.*

displacement for oligomers of different size N and different hydrophobic mismatch is presented in the left column of Figure 5.7. Comparing the monitored MSD curves with a linear function (black, solid line) suggests that the center of mass is diffusing normally. Fitting a power-law

$$\langle \Delta x_{cm}^2 \rangle \propto t^\alpha$$

to the simulational data corroborates this visual assumption. The various values for the scaling exponent α are all very close to unity indicating normal diffusion behaviour. This universal behaviour is in perfect agreement with theoretical predictions. Table 5.3 summarizes the results of the individual fits. Here, the range of the power-law fit was not restricted to a certain interval but rather covered the whole time interval.

Given the fact that the center of mass diffuses normally, one can derive an apparent diffusion coefficient from the MSD curves. Since for normal diffusion, equation 5.6 holds, the diffusion coefficient D_{cm} is calculated by adjusting a linear function to the numerically obtained mean-square displacements. By plotting D_{cm} against the oligomeric size N in double-logarithmic style (cf. Figure 5.7 right column), one recognizes that the diffusion coefficient follows again a power-law (cf. Equation 5.8)

$$D_{cm} \propto N^{-\nu_D}$$

Apparently, the diffusion coefficient of the center of mass is dependent on the oligomeric size N . This is in contradiction to the Zimm model that predicts a size-independent diffusion constant in two dimensions, i.e. $\nu_D = 0$. However,

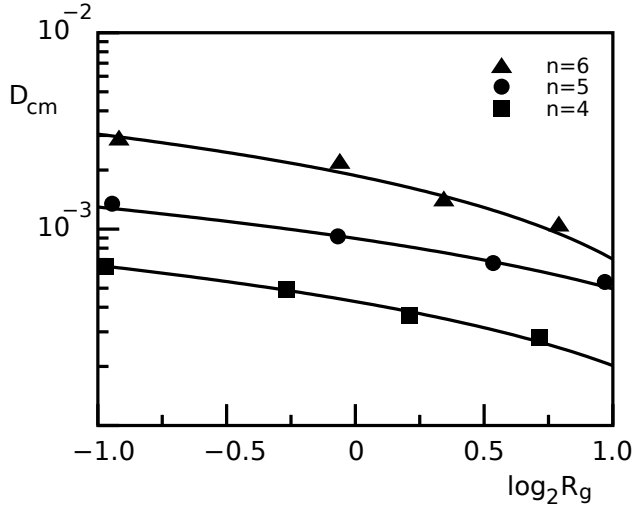


Figure 5.8: Center of mass diffusion coefficient as a function of the radius of gyration. The data is in good agreement with the theoretical prediction of Equation 5.11. Note that, for better visibility, the data for $n = 5$ and $n = 6$ have been shifted by a factor of 2 and 4, respectively.

fitting the data to a power-law, the predicted value of the Rouse model, $\nu_D = 1$, is obtained neither. Rather, a value of $\nu_D \approx 1/2$ is found. Consequently, the observed behaviour reflected by the scaling of the center of mass diffusion coefficient is more Rouse-like. The numerical values for ν_D are given in the most-right column of Table 5.3 for various hydrophobic mismatch.

Interestingly, all values of ν_D are close to the three-dimensional value of ν_D as predicted by the Zimm model. Whether this finding is a pure coincidence or whether numerical artifacts are responsible for this result cannot be fully answered. A possible error source could be the two-dimensional projection of the dynamical data. Besides, finite-size effects may also play a role.

The latter point was investigated in Reference (Punkkinen05). Here, the authors relate the center of mass diffusion coefficient and the radius of gyration in consideration of the (finite) system length L .

$$D_{cm} \propto \ln(L/R_g) \quad (5.11)$$

They argue that this logarithmic dependence is equivalent to a vanishing value of ν_D , i.e. the center of mass diffusion coefficient obey Zimm theory. Plotting our numerical values of D_{cm} against the radius of gyration and fitting the above expression to our data is in good agreement with the theoretical prediction of Equation 5.11. Figure 5.8 displays D_{cm} as a function of R_g for different hydrophobic mismatches.

Since we used different system sizes to derive the various values of the center of mass diffusion coefficient, we included the system length L as an additional fit parameter. The values of L obtained by the different fits hardly varies, justifying our procedure. We now have a second interpretation of the center of mass diffusion coefficient. According to the last evaluations, D_{cm} now reflects Zimm-

like behaviour, in contrast to our previous analysis. Combined with the sub-diffusive character of the monomer motion, the problem whether these oligomeric entities are to be treated with Rouse or Zimm theory seems gotten worse. Possible solutions to definitely determine the character of the oligomer motion in two dimensions are to model the system of interest by either a Langevin equation or by a two-dimensional DPD setup. However, both approaches have their drawbacks. On the one hand, the Langevin approach does not include hydrodynamic interactions which is to exclude Zimm-like behaviour. On the other hand, although a two-dimensional DPD implementation accounts for proper hydrodynamics, it is doubtful whether the correct dynamics can be reproduced since the Navier-Stokes equation is divergent in two-dimensions.

Chapter 6

Polymer translocation through a nanopore

In this chapter, we shift our focus from lipid membranes and transmembrane proteins to another large class of macromolecules in living cells, namely polymers. In particular, we discuss the process of a polymer translocating through a small pore. Such an event occurs frequently in living cells. Prominent examples are DNA/RNA translocation through nuclear pores (Kohler07) or polypeptide translocation through the translocon (Rapoport07). These events are not restricted to endogenous processes. Some viruses, like Hepatitis-C virus, replicate in protective cavities formed by intracellular membranes (Appel06; Moradpour07). The escape of the newly synthesized viral genome from these replication complexes is also such a translocation event.

Besides, polymer translocation also plays an important role in laboratory techniques like polymer fractionation by gel permeation chromatography (DeGennes99). During the past years, an increasing number of elaborate experimental and theoretical approaches have been applied to elucidate the physics of the translocation process under various conditions (Meller03; Dekker07; Muthukumar07; Kolomeisky08).

In the following, we discuss the effect of solvent conditions on the translocation behaviour of a polymer through a nanopore. Changing the solvent condition on one side of the pore accelerates and drives the translocation process. After a short description of how our simulations are set up and a brief summary of theoretical predictions concerning translocation times, results for biased polymer translocation are presented.

6.1 Basic setup

This section describes the membrane-polymer system we use to investigate the translocation process. The DPD formalism is applied to model a simple but though appropriate membrane model and is also used to construct the translocating polymer.

Membrane model In contrast to the previous chapters in which a membrane is modeled as two opposing leaflets consisting of individual lipids, a simpler, more coarse-grained, approach is chosen in the present chapter. A single leaflet of the separating membrane is described by a lattice of inter-connected single DPD beads. To connect both leaflets as well as individual beads in each leaflet harmonic bonds of the following form are used

$$U_h(\mathbf{r}_{i,i+1}) = \frac{k_h}{2} \cdot (|\mathbf{r}_{i,i+1}| - \ell_0)^2 \quad (6.1)$$

The amplitude of the harmonic potential is set to $k_h = 100k_B T$ and the equilibrium distance to $\ell_0 = 0.45r_c$ where r_c is the default DPD cut-off radius. To account for a membrane's inherent stiffness, an additional bending potential is imposed in lateral direction via

$$U_b(\mathbf{r}_{i-1}, \mathbf{r}_i, \mathbf{r}_{i+1}) = k_b \cdot [1 - \cos(\phi)] \quad (6.2)$$

with $k_b = 10k_B T$ and

$$\cos(\phi) = \frac{\mathbf{r}_{i-1,i} \cdot \mathbf{r}_{i,i+1}}{|\mathbf{r}_{i-1,i}| |\mathbf{r}_{i,i+1}|}$$

This implementation is appropriate in several aspects: first, it does not permit movement of bulk DPD beads along the membrane normal, i.e. it represents an impermeable barrier; second, it behaves like a real surface since it exhibits the theoretically predicted q^{-4} scaling of its undulations; third and last, it reduces the computational complexity to a minimum.

In order to facilitate the translocation of a polymer chain across the membrane barrier, a nanopore is integrated in terms of 'ghost beads'. These phantoms only interact with their neighboring membrane beads and are otherwise given a vanishing interaction with all other beads. They are thus exclusively subject to structural forces, i.e. harmonic and bending potential, that establish the separating membrane. The pore is represented by a 3×3 square of 'ghost beads' resulting in a pore diameter of roughly $2r_c$.

Polymer model A polymer in our DPD description is obtained by simply connecting single DPD beads to a linear polymer chain. DPD beads are tethered

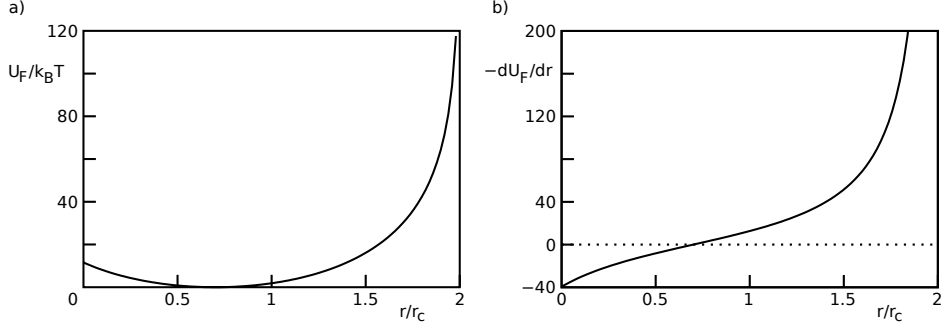


Figure 6.1: a) FENE potential U_F used to connect single DPD beads to create a polymer. Note that U_F is not symmetric to its equilibrium distance. b) Force derived from U_F . For small and intermediate distances r , the force is approximately linear in r while it grows drastically for larger distances. The parameters k_F and l are chosen as described in the text.

by finite extensible nonlinear elastic (FENE) bonds that are derived from the potential (Jiang07)

$$U_F(\mathbf{r}_{i,i+1}) = -\frac{k_F (2r_c - l)^2}{2} \cdot \ln \left[1 - \left(\frac{|\mathbf{r}_{i,i+1}| - l}{2r_c - l} \right)^2 \right] \quad (6.3)$$

Here, the strength of the FENE bonds is set to $k_F = 40k_B T$, the corresponding equilibrium distance adopts the value $l = 0.7r_c$. A chart of U_F is provided by Figure 6.1. As can be clearly seen, U_F is not symmetric with respect to its equilibrium value l like common harmonic potentials. Instead, it grows drastically if two monomers are too far apart. The force derived from the FENE potential exhibits an approximate linear force-distance relationship for small and intermediate separations. For large values of r , it grows disproportionately strong avoiding a too large spatial separation between consecutive polymer beads.

Simulation procedure Following the standard DPD formulation, the interaction cut-off radius r_c , the bead mass m and the thermostat temperature are set to unity. Parameters for noise and dissipation are set to $\sigma = 3$ and $\gamma = 4.5$, respectively. According to our setup, all beads can be classified as either solvent (S) or monomer beads (M). The default value of the repulsion parameter between these bead types is set to $\mathcal{A}_{SS} = \mathcal{A}_{MS} = \mathcal{A}_{MM} = 25$. To probe a forced translocation process, \mathcal{A}_{MS} is varied. We address this point later.

A velocity Verlet integration scheme is used to evolve the equations of motion in time with the time increment $\Delta t = 0.04$. The size of the simulation box is

adjusted to the polymer size N to minimize influences resulting from the periodic boundary conditions.

In a first simulation series, we determine static properties and compare them to polymer theory, cf. Chapter 2. To this end we do not include a separating membrane and monitor only a polymer in solution. The results from this series serves to optimize the simulation settings for a second sequence. Now, the simulation box consists of two reservoirs separated by a polymerized membrane as described above. Changing the repulsive interaction between monomer and solvent particles in one reservoir leads to a driven polymer translocation. We continue by presenting numerical results for static polymer properties and complete the chapter with a section covering the translocation process through a narrow pore.

6.2 Static polymer properties

Basic static properties of our DPD polymer model are discussed in this section. We first explore the scaling behaviour of the radius of gyration, R_g , under different solvent conditions. Subsequently, we consider how simulations investigating a translocation process are in our framework implemented best and how possible artifacts are minimized.

6.2.1 Polymers under different solvent conditions

As pointed out in the introductory chapter on membranes and polymers, the best way to describe the size of a general polymer containing N monomers is the radius of gyration R_g . As a reminder, we repeat its definition

$$R_g^2 = \frac{1}{N} \sum_{i=1}^N (\mathbf{R}_i - \mathbf{R}_{CM})^2 \quad \text{with} \quad \mathbf{R}_{CM} = \frac{1}{N} \sum_{i=1}^N \mathbf{R}_i \quad (6.4)$$

The \mathbf{R}_i 's are the coordinates of the individual monomers and \mathbf{R}_{CM} the corresponding center of mass. According to Flory theory, the squared radius of gyration exhibits a distinct scaling behaviour on the polymer size that reads

$$R_g^2 \propto N^{2\nu} \quad (6.5)$$

The Flory exponent ν is a measure for the excluded volume effect due to the finite size of the single monomers. It also depends on the quality of the solvent the polymer is floating in and it reduces with decreasing solvent quality. Limiting values in three dimensions are $\nu \approx 3/5$ for good solvents and $\nu = 1/3$ for poor solvents.

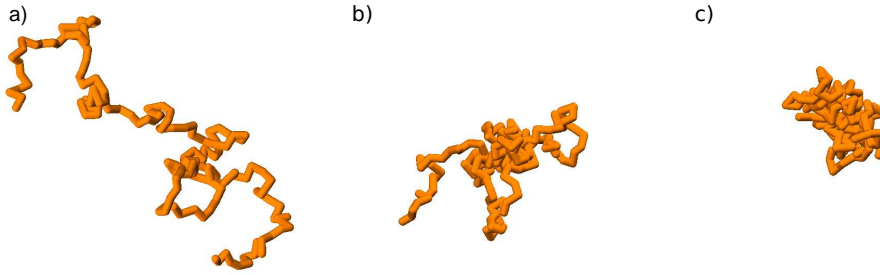


Figure 6.2: *Effect of different solvent qualities on the global shape of a polymer. a) Reference state of a polymer ($N = 150$) in good solvent. In b) and c), repulsion between solvent and monomer particles is increased by 10% and 20%, respectively. A transition to the molten globule state is observed.*

To determine the scaling behaviour of R_g , a single polymer of different length N in solution is simulated. The polymer is placed in a spiral configuration around the center of simulation box. The dimensions of the simulation box are chosen in such a way that the polymer is not able to feel itself due to applied periodic boundary conditions. Polymers of up to a size of $N = 100$ are placed in a box of edge length $L = 25r_c$, an edge length of $L = 35r_c$ is used for larger polymers. Thus, our simulation settings correspond to a dilute polymer solution to which Flory theory can be applied.

Equation 6.5 tells us that a polymer can in large parts ($\approx 70\%$) be enclosed by a sphere of radius R_g , a poor solvent reduces this radius. Figure 6.2 visualizes the effect of different solvent conditions on the global configuration of the polymer chain. To obtain solvents of different quality, we increased the default repulsion between monomer and solvent particles by an amount ΔA .

In part a) of Figure 6.2, the repulsion between monomer particles and solvent particles is set to the default value $\mathcal{A}_0 = 25$. The polymer exhibits a rather extended shape, monomers that are far apart along the chain are also remote in space. One has to note that the polymer can nevertheless adopt more crumpled states. However, the polymer strives to assume entropically preferred conformations. Increasing the repulsion between monomers and solvent by 10% yields a distinct decrease in polymer size (see Figure 6.2b). The shape of the polymer is similar to a loose crumpled thread. Further amplifying the aversion between the two particle types, i.e. $\Delta A = 20\%$, results in a breakdown of the polymer into the so-called *molten globule* state (see Figure 6.2c). Interactions of monomers with many bond lengths in between become unavoidable, the polymer now resembles a ball of wool.

To describe the polymer behaviour in different solvent conditions quantitatively,

the squared radius of gyration R_g^2 is calculated and drawn against the polymer size N . This data is depicted in Figure 6.3a. In good solvent conditions, we observe a scaling of the radius of gyration $R_g \propto N^\nu$ with $\nu = 0.61 \pm 0.02$. This value is consistent with the theoretical predictions of a Flory polymer (Doi01). A reduction in solvent quality by increasing \mathcal{A}_{MS} by ΔA results in a more and more shallow scaling of R_g . Eventually, the polymer chain reaches the molten globule state with a limiting scaling exponent of $\nu = 1/3$. The dependence of the scaling exponent ν on solvent quality is depicted in Figure 6.3b.

A thorough inspection of how the scaling exponent varies with increasing polymer-solvent repulsion reveals that for $\Delta A = 20\%$, ν drops below the limiting value $1/3$. This artifact arises from the soft core nature of the DPD beads: DPD beads can overlap and can consequently adopt more confined conformations compared to (real) hard-core polymer systems.

This part shows that a DPD polymer is able to confidently reproduce the theoretically predicted polymer behaviour. We continue with the description of how our polymer simulations are optimized in order to avoid undesired artifacts arising, for example, from periodic boundary conditions.

6.2.2 Optimization of the reference system

In this section, we describe how the simulational setup for monitoring translocation events is chosen. Key parameters are the size of the simulation box and the equilibration period that is chosen to avoid unwanted correlations between polymer configurations.

Calibrating the size of the simulation box The applied simulation box length to calculate the scaling behaviour of the radius of gyration was chosen in a very conservative manner. The large numerical value impedes any interaction between monomers arising from periodic boundary conditions. As can be derived from Figure 6.3a, a polymer of size $N = 200$ has a radius of gyration of $R_g \approx 7r_c$ under good solvent conditions. Therefore, an edge length of $L = 35r_c$ is definitely sufficient to avoid periodic boundary effects.

A disadvantage of these huge sizes is that the time for a single simulation step increases drastically. Our goal is thus to find a balance between minimizing finite-size effects and maximal computational speed-up. Therefore, we decide to enlarge the box size in the direction of the translocation, i.e. normal to the separating membrane, and to keep it as small as possible in the lateral directions. Appropriate and reasonable choices for the normal and lateral sizes are $L_\perp = 5 \cdot R_g$ and $L_\parallel = 3 \cdot R_g$, respectively. The fact that the polymer migrates mainly in normal direction justifies the smaller box size in lateral direction. Compared to a cubic

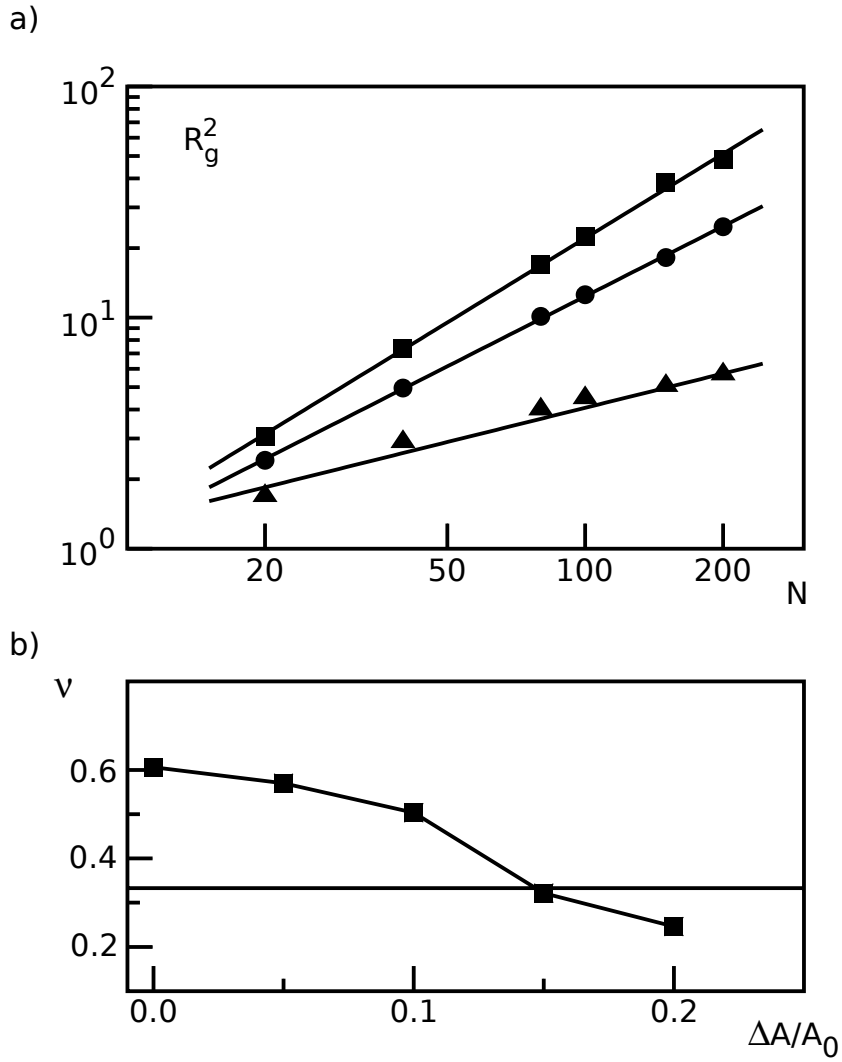


Figure 6.3: a) The radius of gyration of a flexible polymer of length N in good solvent conditions scales as $R_g \propto N^\nu$ with $\nu = 0.61$ (squares). Increasing the solvent-polymer interaction by ΔA yields a weaker scaling of R_g (circles: $\Delta A = 10\%$, triangles: $\Delta A = 20\%$). b) The scaling exponent ν decreases with decreasing solvent quality. Its limiting value is $\nu = 1/3$ (solid line). Errorbars in a) and b) have symbol size, the line between data points in b) serves as a guide for the eye.

Polymer Translocation

box with edge length $L = 4 \cdot R_g$, the latter cuboid geometry is approximately 1.5-fold faster.

Selection on an appropriate equilibration time In order to avoid correlations between different initial configurations of the translocation process (cf. next section), we determine first the (inherent) auto-correlation of the squared radius of gyration and derive from these results the time after which a new, statistically independent polymer conformation is reached. The auto-correlation function $AC_X(t)$ of a time series of a quantity X is given by

$$AC_X(t) = \frac{\langle X_0 X_t \rangle - \mu_X^2}{\sigma_X^2} \quad (6.6)$$

Here, μ_X and σ_X^2 denote the mean and variance of the stochastic variable X , respectively. When normalized in this way, the auto-correlation function is 1 at $t = 0$ and decays to zero as $t \rightarrow \infty$. For systems in equilibrium like the one studied here, $AC_X(t)$ is expected to show an exponential decay (Landau05) with the characteristic, or relaxation, time τ_X

$$AC_X(t) = \exp\left(-\frac{t}{\tau_X}\right) \quad (6.7)$$

The index X already indicates that different quantities X can have different characteristic times τ_X . In Figure 6.4a, auto-correlation functions of R_g^2 for polymers with $N = 100, 150$ and 200 are shown. As can be seen, a larger polymer size leads to a longer relaxation time τ . The solid lines represent exponential fits to the data giving various values of τ . The deviations of $AC(t)$ around zero at large values of t are due to the finite observation time of R_g^2 .

The fitted values of τ are drawn against N in Figure 6.4b. Again, the characteristics of the relaxation time can be described by a power-law, $\tau \propto N^\beta$ with $\beta = 1.79 \pm 0.03$. The scaling exponent of the relaxation time, β , is linked to the Flory exponent of the radius of gyration, ν . Rouse theory predicts a scaling of the relaxation time as $\tau \propto N^{1+2\nu}$ while Zimm theory expects a faster relaxation time as determined by $\tau \propto N^{3\nu}$. Utilizing the above derived value of $\nu = 0.61 \pm 0.01$, it becomes evident that Zimm theory seems to be the adequate description for this system rather than Rouse theory. In conclusion, we can state that the applied DPD implementation of a polymer in solution reproduces very well static polymer properties as predicted by Zimm theory.

As a consequence, we choose an equilibration time of $T_{eq} = 2\tau$ between monitoring consecutive translocation events. Combined with the former derived values of the lateral and vertical size of the simulation box, the chosen value of T_{eq} guarantees that every translocation event is statistically independent from all

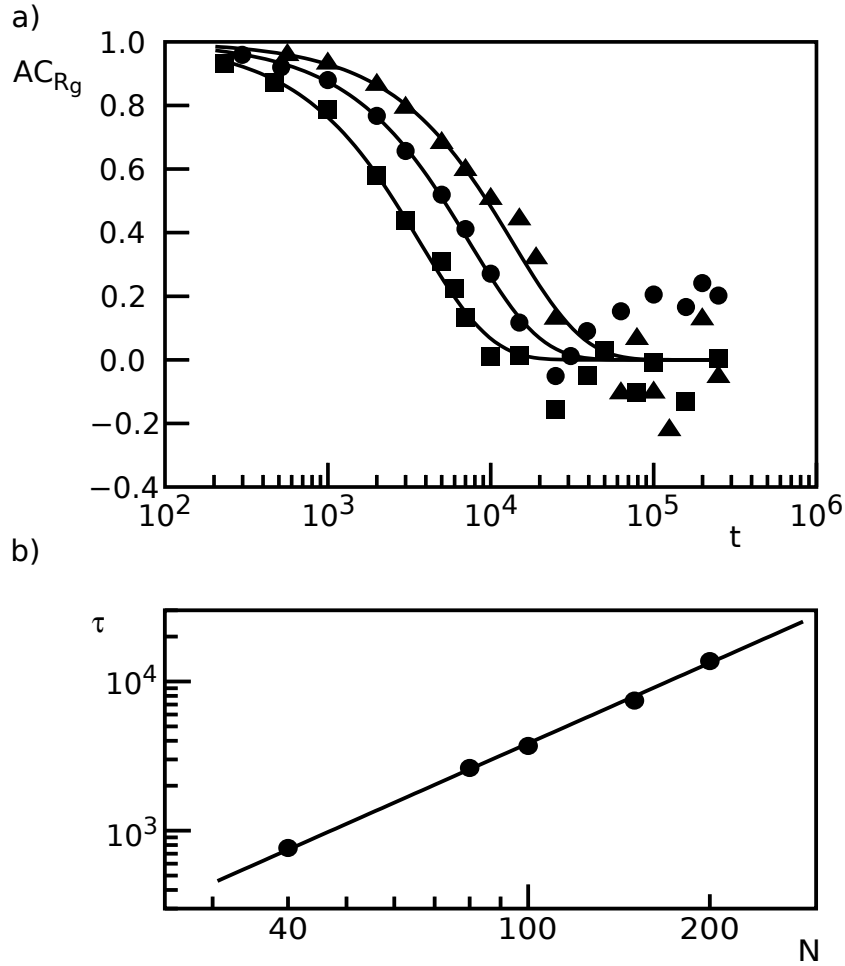


Figure 6.4: a) Auto-correlation functions of R_g^2 for a polymer of size 100 (squares), 150 (circles) and 200 (triangles). The solid lines are exponential decay curves fitted to the numerical data. b) Relaxation time τ as a function of polymer size N obtained by fitting the auto-correlation curves with an exponential decay. The dependence of τ on N follows a power-law, $\tau \propto N^\beta$ with $\beta = 1.79 \pm 0.03$ (solid line) and is in agreement with Zimm theory.

others. In the next section, we explore how solvent quality affects the translocation behaviour of a polymer chain through a nanopore.

6.3 Translocating polymers

In the preceding section, static polymer properties and their different scaling behaviours were discussed. We now turn our attention to the dynamics of a polymer translocating through a narrow pore.

Data acquisition The initial setup of the membrane-polymer system is as follows: the separating membrane is placed symmetrically around $L_{\perp}/2$ with the pore in its central position. The two central monomer beads are placed inside the pore and during equilibration fixed to the pore via harmonic springs. To prevent unwanted crossing of monomers during the equilibration periods, the pore is additionally closed by turning ghost beads into real membrane beads. After equilibration, the polymer is released and the pore opens to monitor the translocation process. Data acquisition includes spatial coordinates of monomer and membrane beads and the translocation state of the polymer. To determine the latter quantity, absolute coordinates of membrane and polymer beads have to be used in order to circumvent artifacts of the periodic boundary conditions. A polymer is considered to have passed the pore if all polymer beads are left or right of the center of mass of the pore. Before monitoring a subsequent translocation event, the system is equilibrated again as described above. Consequently, several hundred translocation events in a single simulation run with ever different initial configurations are recorded.

Figure 6.5 displays the initial (a) and final (b) state of a polymer consisting of $N = 150$ monomers. As can be clearly seen, contact of polymer beads with ‘poor’ solvent results in a confined globular state of the polymer chain. On the ‘good’ solvent side, the polymer adopts an extended and swollen configuration.

6.3.1 Unbiased translocation

Before we are going to discuss results for the biased polymer translocation, we would like to spend a few words on unbiased translocation events. According to our setup, a polymer of size N is initially placed in a state in which the number of monomers m on each side of the pore is equal. The free energy F in this state can be expressed as (Muthukumar99)

$$F = c_1 \ln(m) + c_2 \ln(N - m) + m\Delta\mu \quad (6.8)$$

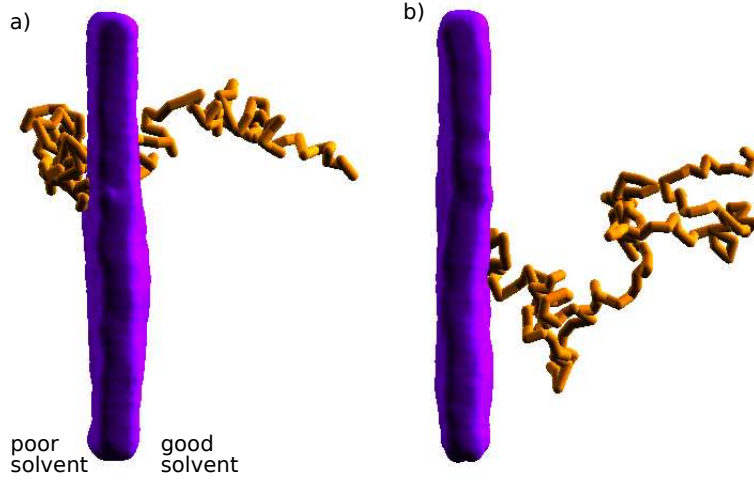


Figure 6.5: a) Polymer of size $N = 150$ right before pore opening and beginning of translocation. On the poor solvent side, repulsion between monomers and solvent is increased by $\Delta A = 20\%$ leading to a collapse of the polymer chain. b) The polymer migrates towards the good solvent side on which an entropically more advantageous conformation is adopted.

The factors $c_{1,2}$ depend on conformational statistics on each side, $\Delta\mu$ is the difference in chemical potential between the two reservoirs. In case of an undriven system, i.e. no difference in solvent on both sides, $c_1 = c_2$ and $\Delta\mu = 0$. Thus, F exhibits a free energy barrier symmetric in m/N . This symmetry means that a translocation of the polymer to the left or to the right is equally likely. Indeed, we observe for unbiased translocations that on average 50% of the polymers migrate to the left and the other half are finally found in the right reservoir.

Next, we inspect the behaviour of the polymer's translocation time T_t through the nanopore. Interestingly, the Flory exponent ν has been predicted to influence the scaling of the translocation time if hydrodynamic interactions are disregarded. According to (Kolomeisky08; Chuang01) the translocation time follows $T_t \propto N^\beta$, $\beta = 1 + 2\nu$, i.e. it shows the same behaviour as the relaxation time τ in Rouse theory. However, a basic ingredient of DPD simulations is that they take into account hydrodynamic interactions. We therefore tested whether this scaling is altered for Zimm polymers and how it is influenced by solvent quality. Figure 6.6 displays numerical results of the unbiased translocation time for different solvent qualities. At good solvent quality, the scaling exponent is determined to be $\beta = 2.22 \pm 0.06$. This value perfectly coincides with the theoretical prediction of the Rouse model that gives with $\nu = 0.61$ a value of $\beta = 1 + 2\nu = 2.22$. Consequently, hydrodynamic interactions do not seem to influence the translo-

Polymer Translocation

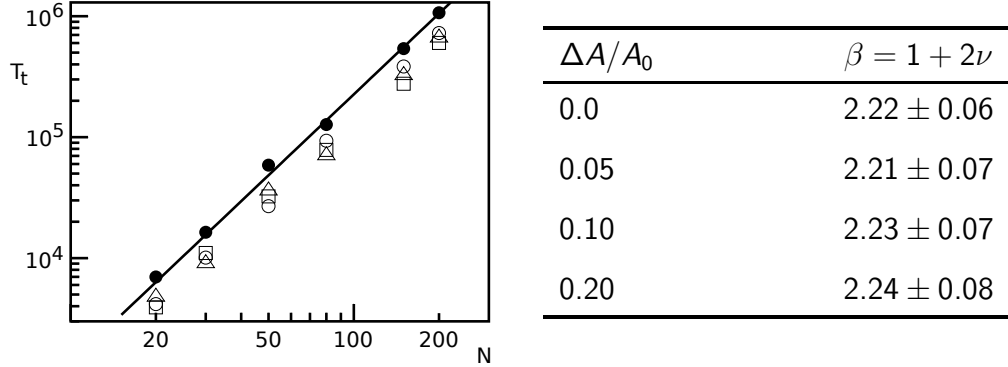


Figure 6.6: Unbiased translocation time T_t (left) and corresponding scaling exponent β (right). Under good solvent conditions, T_t scales like $N^{2.22}$ (filled circles, solid line; data shifted by factor 1.5 for better visibility). Increasing the polymer-solvent repulsion (open symbols) does hardly change the numerical value of β (cf. right table).

cation process as long as the pore is small enough.

What happens if one symmetrically changes the solvent quality on both sides of the pore? Surprisingly, the scaling of T_t does not change when the interaction between monomer and solvent particles is increased by $\Delta A/A_0 = 0.05, 0.1, 0.2$ in each reservoir. This observation is in strong contradiction to the scaling of the radius of gyration R_g under different solvent conditions (cf. Figure 6.3). Assuming the polymer's relaxation time τ to be the dominant time scale in the translocation process, one might have expected a change in the scaling of T_t .

A possible explanation for the latter observation can be derived by exploring the extreme case of a translocating rod polymer. The diffusive translocation of a rod-like polymer is characterized by $\beta = 2$. This in turn means that the scaling of T_t cannot be smaller than this limiting value. In addition, the polymer has to adopt configurations that allow to pass the pore. This constraint reduces the number of possible polymer chain conformations. Consequently, the chain entropy decreases and an entropic barrier is set up (Muthukumar01). The incorporation of this effect results in the following scaling of the translocation time, $T_t \propto N^{1+2\nu} N^{1-\mu}$ with $\mu = 0.68$ (Dubbeldam07). Interpreting the diffusive passage through the pore as the dominant time scale, the latter expression reduces to $T_t \propto N^2 N^{1-\mu}$ giving $\beta \approx 2.3$ independent of the Flory exponent ν . The so-obtained value does not coincide perfectly with our numerical value but is close to it. The present deviation may result from the fact that the size of the nanopore here is not as small as to allow only the successive passage of single polymer segments. Hence, a larger configuration space is available increasing chain entropy that presumably lowers μ .

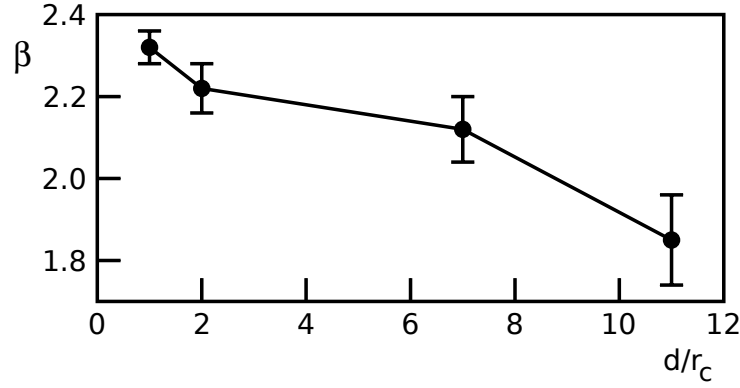


Figure 6.7: The scaling exponent β of the translocation time displays a turnover from Rouse to Zimm dynamics when the pore diameter d is increased. Lines between data points serve as guides for the eye.

Dependence of T_t on pore size To complement this part on unbiased translocation, we provide data of how the scaling of the translocation time changes if the pore diameter (d) is increased. For a pore diameter of $d = 1r_c$, the above derived scaling of the translocation time coincides perfectly with our numerical observation, i.e. $\beta = 2.32 \pm 0.05$. Increasing the pore size yields a systematic decrease of the scaling exponent towards $\beta = 1.8$ which is consistent with Zimm theory (cf. Figure 6.7). Increasing the pore size thus leads to a turnover from Rouse to Zimm behaviour in which the scaling exponent is expected to be $\beta = 3\nu \approx 1.83$. Now, more and more solvent particles are dragged with the polymer chain whereas a smaller pore size is able to impede this collective motion.

6.3.2 Biased translocation

The next aim in our study is to investigate a biased translocation process. To this end, we change the solvent quality on one side of the pore. In particular, we increase the polymer-solvent repulsion in one reservoir by $\Delta A > 0$, i.e. $\mathcal{A}_{MS} = (25 + \Delta A)k_B T$, while \mathcal{A}_{MS} is not altered in the other partial volume. The conformation of the polymer right before opening of the pore and begin of the translocation process is now as depicted in Figure 6.5. The part of the polymer on the side of poor solvent is coiled up and occupies less space than its counterpart on the other, the good-solvent, side. Consequently, the expression for the free energy, Equation 6.8, becomes asymmetric in m/N as shown in Figure 6.8 The course in F is now downhill from the reservoir with poor solvent towards the reservoir with good solvent. That means that the polymer chain is preferably

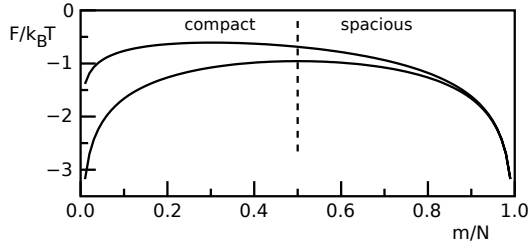


Figure 6.8: Free energy F for asymmetric (upper curve) and symmetric (lower curve) solvent qualities. While the free energy is symmetric in m/N in the latter case, F shows a downhill course when the pore connects two reservoirs with different solvents. Note that the

difference in chemical potential is set to zero. The terms ‘compact’ and ‘spacious’ indicate the reservoir with poor and good solvent respectively.

migrating towards the good-solvent side. For the sake of simplicity, we assume that the difference in chemical potential between the two solvent reservoirs is zero, $\Delta\mu = 0$. This is a valid assumption since the chemical potential difference between the two solvents can be neglected in zeroth order approximation. Hence, the migration is solely driven by conformational statistics in both regions.

Increasing ΔA decreases T_t

Increasing the solvent-polymer repulsion by ΔA results in an acceleration of the translocation and in a reduction of the scaling exponent β of the translocation time. Starting from $\beta \approx 2.22$ observed for the unbiased translocation, β decreases steadily. Figure 6.9 displays the observed translocation time for varying $\Delta A/A_0$ (part a) and the numerically fitted scaling exponent β as a function of $\Delta A/A_0$.

It is remarkable that a change in \mathcal{A}_{MS} as small as $\Delta A/A_0 = 5\%$ already yields a drastic drop in the scaling exponent from its default value 2.22 to $\beta \approx 1.34 \pm 0.12$. Increasing the repulsion further, one observes an approaching of the scaling exponent towards unity, i.e. the translocation time is now directly proportional to the polymer size N . Indeed, the limiting value $\beta = 1$ reflects the translocation behaviour of a polymer that is assumed to be permanently relaxed. Including the polymer relaxation resulting from the entropic barrier at the entrance of the pore (see above), one may estimate a minimal value of the scaling exponent of the translocation time as $\beta = 1 + 1 - \mu^1$. Admittedly, giving an exact numerical value for this approximation is rather crude since the entropic term μ can be expected to be influenced by a variety of factors like the size of the pore or the increment ΔA . In the case where the pore is so small that only a single polymer segment at a time is able to pass the pore, one can set $\mu = 0.68$ (cf. above) and hence, $\beta = 1 + 1 - 0.68 = 1.32$ can be interpreted as an upper limit of the scaling exponent.

¹Do not mix up the entropic term μ with the chemical potential.

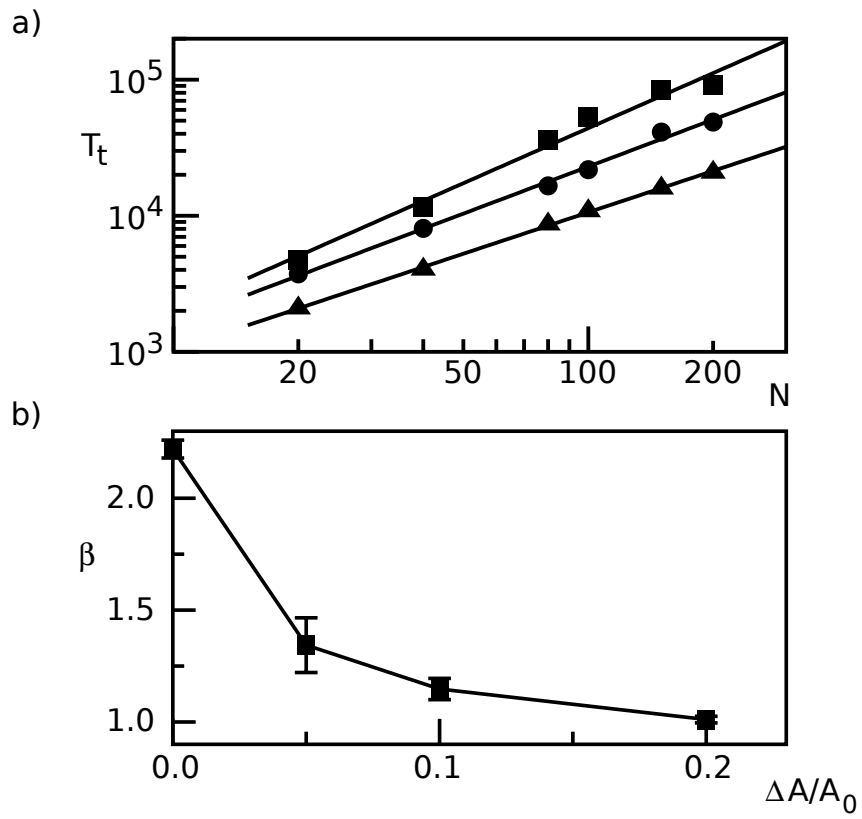


Figure 6.9: Monitored translocation times T_t (a) and corresponding scaling exponents β as obtained by a fit (b). Data points in a) indicate an increase by $\Delta A/A_0 = 5\%$, 10% and 20% (squares, circles, triangles). The lines in b) are guides for the eye.

Polymer Translocation

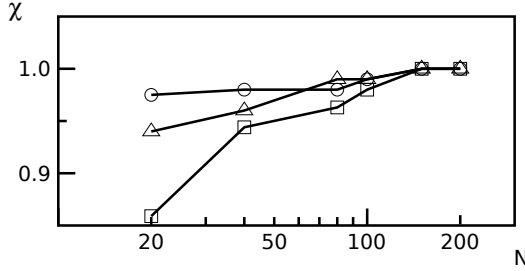


Figure 6.10: *Polymers move preferably towards the good solvent side as indicated by $\chi = 1$. The sympathy for good solvent increases with decreasing poor solvent quality. Data points are for $\Delta A/A_0 = 5\%, 10\%$ and 20% (squares, triangles, circles).*

Besides an accelerated translocation, almost all polymers move towards the good solvent side. To evaluate this observation, we assign each translocation event a binary-valued variable χ . Reaching the poor solvent side is equivalent with $\chi = 0$ while translocation into the good-solvent reservoir results in $\chi = 1$. The average value of χ for different poor solvent qualities is shown in Figure 6.10. Decreasing the poor solvent quality results in an almost exclusive migration towards the reservoir with good solvent. Short polymers, i.e. $N = 20, 40$, are most likely to cross the free energy barrier in the uphill direction, though this behaviour disappears with increasing $\Delta A/A_0$.

Mimicking poor solvent by decreasing monomer repulsion Another possibility to alter the solvent quality can be done by decreasing the repulsive force between individual monomers. This has recently been realized in a Langevin dynamics study (Wei07), i.e. an approach that does not explicitly take into account hydrodynamic interactions. In contrast to the results presented above, this study finds a preferred movement of the polymer towards the poor solvent reservoir. Modifying the solvent quality by decreasing monomer repulsion in our DPD setup, i.e. $\mathcal{A}_{MM} = A_0 - \Delta A$, $\Delta A > 0$, we also find a preferred migration towards the poor solvent reservoir. In addition, the scaling behaviour of the various entities (R_g , T_t etc) develops similar for decreasing monomer-monomer repulsion: ν and β exhibit both a reduction when ΔA is increased. It is of great importance to note that decreasing inter-monomer repulsion does not reflect a bad solvent though. Rather, it mimics attractive monomer interaction as induced by the presence of, for example, ions.

Conclusion

The focus of this chapter was on the unbiased and biased translocation of a polymer through a narrow pore connecting two solvent reservoirs. The key quantity was the translocation time T_t that was assumed to obey a scaling law dependent on the polymer size N : $T_t \propto N^\beta$.

Varying the solvent quality in both reservoirs from good to poor solvent did

surprisingly not affect the scaling exponent β . This can be due to an entropic barrier at the entrance of the pore.

Decreasing the solvent quality by increasing the repulsion between solvent and polymer particles in only one reservoir yielded a preferential translocation towards the good-solvent reservoir. Now, a reduction of the scaling exponent β with decreasing solvent quality was observed. Interestingly, a change in solvent quality by only 5% accelerated the translocation time from $\beta = 2.22$ to $\beta = 1.35$.

Mimicking poor solvent by decreasing monomer-monomer repulsion resulted in a translocation towards the poor solvent side, a result that is contrasted by free energy calculations and entropical arguments. Consequently, this type of modification is not appropriate to model poor solvent conditions. It rather creates a milieu change inducing intra-polymer attractions.

The accelerated translocation may play a role during the reproduction of a virus. Newly synthesized viral RNA has to leave its replication cavity through a narrow hole. A different pH inside the replication cavity may create a poor solvent thus triggering the escape of the nascent viral RNA. Another possible scenario is that the entropic pressure inside the cavity becomes too large resulting in a quick exit.

Chapter 7

Summary & Outlook

Summary

Computer simulations are a viable means to investigate soft matter and biological systems. Their application is especially useful to explore intracellular macromolecules whose sizes are beyond the diffraction limit of light and whose dynamics is thus not accurately observable. A broad class of computer simulations are mesoscopic simulation techniques that act above the level of atomistic detail but still below the threshold to a continuum picture. One major advantage of their mesoscopic character is that these simulations are able to address effects resulting from generic mechanisms, i.e. their results can readily be interpreted in a general framework. One of these mesoscopic techniques is dissipative particle dynamics (DPD) originally invented to study hydrodynamic phenomena. Shortly after its introduction, its application was extended to soft matter systems as well. With DPD, it is possible to explore soft matter systems on length and time scales that are orders of magnitude larger than full-atomistic simulations. In this work, we addressed the dynamical behaviour of intracellular macromolecules like proteins and polymers via dissipative particle dynamics. Our aim was to elucidate physical mechanisms governing their motion.

In the first part, we concentrated on the motion of transmembrane proteins. In particular, we were interested in the effect of how a hydrophobic mismatch with the surrounding lipid bilayer alters the dynamics and the collective behaviour of transmembrane proteins. Former mean-field theoretical studies have shown that hydrophobic mismatching may under favourable circumstances induce inter-protein attraction.

We found that proteins that are either too long or too short to fit perfectly into the surrounding membrane disturb the lipids' configuration in their vicinity sustainably leading to a reduction in configurational entropy. This entropy decrease is in all cases sufficient to induce a long-ranged, lipid-mediated inter-

Summary & Outlook

protein attraction. We found that, in agreement with former theoretical studies, the strength of the attraction depends quadratically on the degree of hydrophobic mismatch yielding (theoretically) an exponential increase in the lifetime of a protein dimer. Further, large-scale simulations confirmed the assumption that hydrophobic mismatching drives protein clustering. The simulationally observed and the – by a simple model – estimated cluster size distribution show qualitatively the same course: the larger the degree of hydrophobic mismatch, the more likely the occurrence of higher-order clusters.

In the next step, we analysed whether a hydrophobic mismatch also accounts for a differential protein sorting. We could affirm this question by further large-scale simulations in a qualitative as well as in a quantitative manner. Connected to the last point is the problem of protein partitioning. Recent experimental studies have shown that a protein integrated into a membrane with non-uniform thickness, diffuses to that membrane region where its hydrophobic mismatch is smallest. Setting up a two-phase bilayer and embedding proteins with different mismatches, we could observe a diffusively partitioning of the single proteins into that part of the membrane where their hydrophobic mismatch was minimized. Therefore, we can state that hydrophobic mismatching acts as a very sensitive protein guide.

Combining the previous results, we developed a simple, HM-based model of how protein sorting may be organized in living cells. Since protein sorting is a self-organized process, there has to be molecular regulations that tell the proteins where to go, or where not to stay. According to the last results, proteins tend to minimize their hydrophobic mismatch. We thus propose that HM-based protein clustering triggers the formation of transport vesicles that shuttle the proteins to a remote membrane where the lipid environment matches their desire, i.e. they do not experience a hydrophobic mismatch. However, changes in the lipid environment or the accidental escape from the preferred membrane results again in clustering and protein re-distribution. The numerical implementation of the outlined hypothesis confirmed the main points in our model, that are an enhanced vesicle formation and, connected to the latter, an increase in protein and membrane flux.

By treating a protein complex diffusing in a membrane and created by an oligomerization process as a two-dimensional polymer, we tried to resolve the dynamics of the single proteins (monomers) and the complex as a whole. Key quantities here were the mean-square displacement of the individual monomers and of the center of mass; since the latter is expected to show normal diffusion, an apparent center of mass diffusion coefficient can also be derived. Our main concern was whether oligomerization is able to qualitatively impede the motion of the single monomers and if so, which polymer model, i.e. Rouse or Zimm theory, is best applicable to this situation. Our result reflect that the monomer motion

is sub-diffusive which is an argument for Rouse theory. However, the resultant diffusion coefficient of the center of mass exhibit a scaling between Rouse and Zimm theory. An additional analysis supported Zimm theory. Our initial question whether oligomerization induces sub-diffusion could be confirmed. The problem whether an oligomeric complex is best described by Rouse or Zimm theory is still to be decided.

The last chapter of this work was dedicated to the translocation of a polymer through a narrow pore. In a first simulation part, we confirmed that our DPD model is suitable to describe polymers in dilute solution. To this end, we monitored static polymer properties like the radius of gyration dependent on the quality of the solvent the polymer is floating in. The second part was to determine the dynamical behaviour during translocation. For unbiased translocation, we found that the translocation time did not vary with the solvent conditions. Biased translocation was realized by decreasing the solvent quality on one side of the pore. An acceleration of the translocation time accompanied by a reduction of its scaling with the polymer length is the consequence. In living cells, a poor solvent may be due to a different pH-value, a temperature shift or the presence of molecular chaperones.

Outlook

With the ever-growing computational power, simulations become more and more useful, since the restriction to small systems vanishes. A step towards larger systems and longer time scales is always appreciated as more realistic scenarios can be created and artifacts, e.g. finite size effects, are reduced. Hence, a further improvement is certainly the development of parallel algorithms, in particular for DPD simulations. Similar approaches have recently been developed for molecular dynamics simulations of large bio-molecules (Phillips05). However, a parallel implementation for DPD simulations is still lacking.

Possible programming environments could be the MPI (message parsing interface) specification (Gropp95) that enables the communication between nodes on a computing cluster. A limiting factor here could be the time that it takes the different nodes to communicate, and the memory organization of the MPI environment.

A second possibility is to use the numerous graphics processing units (GPU) available on ordinary video cards. Several computationally intensive problems like Fast-Fourier transformation (FFT), matrix decomposition or N-body problems have been successfully performed on graphic cards. An appropriate realization is the CUDA (compute unified device architecture) programming environment provided by the nVIDIA company (www.nvidia.com). In terms of memory architecture and organization, CUDA seems to be better suited for parallel DPD

Summary & Outlook

simulations compared to the MPI environment. The development of a parallel DPD implementation with CUDA is currently in progress.

A possible application of a parallel DPD version could be to investigate the formation of lipid droplets, small monolayer-bound entities that serve as intracellular storage depots for neutral lipids. The bio-genesis of these organelles is highly-debated, light and electron microscopy techniques are not able to provide detailed, dynamical pictures impeding the finding of a common interpretation of the formation process. Computer simulation would certainly help to solve this riddle.

Regarding experimental work, there are also possible future studies. Of great importance would definitely be experiments that unequivocally confirm the hypothesis that hydrophobic mismatching drives the formation of protein clusters. Since such a scenario is rather difficult to establish *in vivo*, several *in vitro* systems prove promising to address this question. Among the latter systems are giant unilamellar vesicles (GUV) or model bilayers. Admittedly, the main obstacle would be the synthesis of membrane proteins that experience almost no specific molecular interactions with their counterparts. Whether the latter requirement is feasible, is better to be investigated by biochemists and not by physicists.

Another point that is worth addressing experimentally is the proposed sorting model. Interesting issues are whether secretory transport could be enhanced or completely stalled by introducing proteins with different hydrophobic mismatches. However, here one is not able to use *in vitro* systems and thus approaches in living cells has to be developed.

Finally, we believe that a living cell is by far too complex as that approaches from a single natural scientific discipline is able to answer all questions in a qualitative and quantitative manner. Rather, an interdisciplinary approach is most promising to address and to solve problems emerging in the life sciences.

Part III

Appendix

Appendix A

Integration schemes

The numerical integration of the equations of motion in our DPD simulations is based on a velocity-Verlet algorithm. This applies for both, the NVT ensemble and the NpT ensemble. As we have already given the integration scheme of the NVT ensemble in the main text, we here provide only the algorithm that is used to integrate the NpT ensemble.

A.1 Integrating the NpT ensemble

Usually, data acquisition during our simulations is preceded by the equilibration of the system of interest. Except for the simulations exploring polymer translocation, we use a barostat to obtain a (almost) tensionless membrane. We choose to implement the barostat method developed by Jakobsen (Jakobsen05a). This implementation has the advantage that equilibration of the DPD system happens faster and one does not need larger time steps Δt .

Jakobsen's implementation involves the edge lengths of the simulation box, ϵ , as three additional degrees of freedom. These serve as a piston to keep the pressure constant. The piston's mass is denoted by W and its velocity \mathbf{v}_ϵ . Its motion is described by a Langevin equation and governed by a force \mathbf{F}_ϵ that integrates different properties like the difference from the instantaneous to the target pressure, for example. Additional auxiliary variables are needed to construct the entire integration algorithm that reads

1. $\mathbf{v}_\epsilon'' \leftarrow \mathbf{v}_\epsilon', \mathbf{v}_\epsilon' \leftarrow \mathbf{v}_\epsilon, \epsilon' \leftarrow \epsilon$
2. $\mathbf{v}_i \leftarrow \mathbf{v}_i + \frac{1}{2} \frac{1}{m} \left[(\mathbf{F}_i^C + \mathbf{F}_i^D - 2\mathbf{v}_\epsilon \mathbf{v}_i) \Delta t + \mathbf{F}_i^R \sqrt{\Delta t} \right]$
3. $\mathbf{v}_\epsilon \leftarrow \mathbf{v}_\epsilon + \frac{1}{2} \frac{\mathbf{F}_\epsilon}{W} \Delta t, \epsilon \leftarrow \epsilon + \mathbf{v}_\epsilon \Delta t$

Integration schemes

4. $\mathbf{x}_i \leftarrow (\mathbf{x}_i + \mathbf{v}_i \Delta t) \cdot \exp(\epsilon - \epsilon')$
5. Update the volume \mathcal{V} !
6. Update the forces \mathbf{F}^C , \mathbf{F}^D and \mathbf{F}^R !
7. Find the pressure $\mathcal{P} = \frac{1}{d\mathcal{V}} \left[\sum_i \frac{\mathbf{p}_i^2}{m} + \sum_i \mathbf{F}_i^C \cdot \mathbf{x}_i \right]$
8. $\tilde{\mathbf{v}}_i \leftarrow \mathbf{v}_i, \tilde{v}_\epsilon \leftarrow v_\epsilon$
9. Initial guess of v_ϵ : $v_\epsilon \leftarrow v_\epsilon'' + 2 \frac{F_\epsilon}{W} \Delta t$
- 10a. $\mathbf{v}_i \leftarrow \frac{1}{1+v_\epsilon \Delta t} \left[\exp(\epsilon - \epsilon') \tilde{\mathbf{v}}_i + \frac{1}{2} \frac{1}{m} (\mathbf{F}_i^C + \mathbf{F}_i^D) \Delta t + \mathbf{F}_i^R \sqrt{\Delta t} \right]$
- 10b. Compute \mathbf{F}_ϵ !
- 10c. $v_\epsilon \leftarrow \tilde{v}_\epsilon + \frac{1}{2} \frac{F_\epsilon}{W} \Delta t$
11. Update dissipative forces \mathbf{F}^D !

Steps 10a, b, c are repeated until convergence occurs which is typically achieved after five to ten cycles. For the iteration, one does not need to calculate the default DPD forces. This is quite suitable since their calculation is one of the most time-consuming parts of the algorithm. To calculate the pressure (step 7), different contributions have to be taken into account. The sum over the product of the conservative forces and the position vectors is the virial contribution. One has to note that in the limit $W \rightarrow \infty$, the above algorithm is identical to the velocity-Verlet algorithm.

Appendix B

List of DPD parameters

B.1 Parameters for the NVT and NpT ensemble

The following table summarizes the default values for simulating a fully-hydrated DPD membrane in the NVT ensemble. Parameter values that deviate from this standard setup are mentioned in the main text. The kinetic temperature $k_B T$, the DPD bead mass m and the critical radius r_c act as reference parameters, all other parameters are expressed in units of these.

general parameters	
integration time increment Δt	0.01
kinetic temperature $k_B T$	1.0
DPD bead mass m	1.0
critical radius r_c	1.0
particle density ρ_p	3.0
lipid area density ρ_l	1.43
strength of dissipative force γ	4.5
strength of random force σ	3.0
repulsion between like particles A_{**}	25.0
repulsion between water and head beads A_{WH}	25.0
repulsion between water and tail beads A_{WT}	200.0
lipid bending rigidity k_b	10.0
harmonic force amplitude between lipid beads k_h	100.0
equilibrium distance of harmonic force ℓ_0	0.45

List of DPD parameters

Additional parameters to implement the barostat are presented below. A key quantity is the mass of the piston W , that is given by (Jakobsen05a)

$$W = dNk_B T \tau_p^2$$

where d is the Euclidean dimension, N the total number of particles, $k_B T$ the kinetic temperature and τ_p the rise time of the barostat, respectively. With this choice, the remaining parameters read

barostat parameters	
target pressure P_0	23.649
barostat rise time τ_p	2.0
strength of barostat dissipation γ_p	5.0
strength of barostat random force σ_p	$\sigma_p^2 = 2\gamma_p W k_B T$

The target pressure P_0 is usually set to the pressure of a pure water box.

B.2 Conversion to SI units

In principal, one can extract an intrinsic time scale t_0 from the DPD parameters r_c , $k_B T$ and m via

$$t_0 = \sqrt{mr_c^2/k_B T}$$

Another possibility that we used here is to calibrate the integration time increment Δt via a typical membrane thickness and the lipid's diffusion coefficient. In SI units that means:

$$r_c = 1nm \quad \text{and} \quad \Delta t \approx 80ps$$

Given these relations, every DPD quantity can be readily converted from intrinsic DPD values to meaningful SI units. Thus, 10^6 integration cycles correspond to

$$t_{SI} = 10^6 \Delta t = 10^6 \cdot 80 \cdot 10^{-12} = 80\mu s$$

Bibliography

- [Abrami08] Abrami L, Kunz B, Iacovache I and van der Goot F. Palmitoylation and ubiquitination regulate exit of the Wnt signaling protein LRP6 from the endoplasmic reticulum. *Proc Nat Acad Sci*, **105**, p. 5384, 2008
- [Alberts02] Alberts B, Johnson A, Lewis J, Raff M, Roberts K and Walter P. *Molecular Biology of the Cell*. Garland Science, 4th ed., 2002
- [Andersen80] Andersen H. Molecular dynamics at constant pressure and/or temperature. *J Chem Phys*, **72**, p. 2384, 1980
- [Appel06] Appel N, Schaller T, Penin F and Bartenschlager R. From structure to function: new insights into Hepatitis C virus RNA replication. *J Biol Chem*, **281**, p. 9833, 2006
- [Axelrod76] Axelrod D, Koppel D, Schlessing J, Elson E and Webb W. Mobility measurement by analysis of fluorescence photobleaching recovery kinetics. *Biophys J*, **16**, p. 1055, 1976
- [Barlowe94] Barlowe C, Orci L, Yeung T, Hosobuchi M, Hamamoto S, Salama N, Rexach M, Amherdt M and Schekman R. COPII: a membrane coat formed by Sec proteins that drive vesicle budding from the endoplasmic reticulum. *Cell*, **77**, p. 895, 1994
- [Berendsen84] Berendsen H, Postma J, van Gunsteren W, DiNola A and Haak J. Molecular dynamics with coupling to an external bath. *J Chem Phys*, **81**, p. 3684, 1984
- [Boal02] Boal D. *Mechanics of the Cell*. Cambridge University Press, 1st ed., 2002

BIBLIOGRAPHY

- [Bouchaud90] Bouchaud JP and Georges A. Anomalous diffusion in disordered media: statistical mechanics, models and physical applications. *Phys Rep*, **195**, p. 127, 1990
- [Brannigan04] Brannigan G and Brown F. Solvent-free simulations of fluid membrane bilayers. *J Chem Phys*, **120**, p. 1059, 2004
- [Bretscher93] Bretscher M and Munro S. Cholesterol and the Golgi apparatus. *Science*, **261**, p. 1280, 1993
- [Bruinsma96] Bruinsma R and Pincus P. Protein aggregation in membranes. *Curr Opin Solid State Mater Sci*, **1**, p. 401, 1996
- [Callen51] Callen H and Welton T. Irreversibility and generalized noise. *Phys Rev*, **83**, p. 34, 1951
- [Cheng96] Cheng A and jr KM. The pressure and pressure tensor for macromolecular systems. *J Phys Chem*, **100**, p. 905, 1996
- [Chuang01] Chuang J, Kantor Y and Kardar M. Anomalous dynamics of translocation. *Phys Rev E*, **65**, p. 011802, 2001
- [Cole96] Cole N, Smith C, Sciaky N, Terasaki M, Edidin M and Lippincott-Schwartz J. Diffusional mobility of Golgi proteins in membranes of living cells. *Science*, **273**, p. 797, 1996
- [Cooke05] Cooke I, Kremer K and Deserno M. Tunable generic model for fluid bilayer membranes. *Phys Rev E*, **72**, p. 011506, 2005
- [Cossart04] Cossart P and Sansonetti P. Bacterial invasion: the paradigms of enteroinvasive pathopogens. *Science*, **304**, p. 242, 2004
- [Crick56] Crick F and Watson J. Structure of small viruses. *Nature*, **177**, p. 473, 1956
- [Dan93] Dan N, Pincus P and Safran S. Membrane-induced interactions between inclusions. *Langmuir*, **9**, p. 2768, 1993
- [Dan94] Dan N, Berman A, Pincus P and SASafran. Membrane-induced interactions between inclusions. *J Phys II France*, **4**, p. 1713, 1994
- [DeGennes99] DeGennes P. *Polymers in confined environments*, vol. 138 of *Advances in polymer science*. Springer Verlag Berlin, 1999

-
- [Dekker07] Dekker C. Solid-state nanopores. *Nature Nanotechnology*, **2**, p. 209, 2007
- [deMeyer08] deMeyer F, Venturoli M and Smit B. Molecular simulations of lipid-mediated protein-protein interactions. *Biophys J*, **95**, p. 1851, 2008
- [Doi01] Doi M and Edwards S. *The Theory of Polymer Dynamics*. Oxford University Press, 2001
- [Dubbeldam07] Dubbeldam J, Milchev A, Rostiashvili V and Vilgis T. Driven polymer translocation through a nanopore: a manifestation of anomalous diffusion. *Europhys Lett*, **79**, p. 18002, 2007
- [Edholm87] Edholm O and Johansson J. Lipid bilayer polypeptide interactions studied by molecular dynamics simulations. *Eur Biophys J*, **14**, p. 203, 1987
- [Edidin03] Edidin M. The state of lipid rafts: from model membranes to cells. *Annu Rev Biophys Biomol Struct*, **32**, p. 257, 2003
- [Einstein05] Einstein A. Über die von der molekularkinetischen Theorie der Wärme geforderte Bewegung von in ruhenden Flüssigkeiten suspendierten Teilchen. *Ann Phys*, **17**, p. 549, 1905
- [Español93] Español P and Warren P. Statistical mechanics of dissipative particle dynamics. *Europhys Lett*, **30**, p. 191, 1993
- [Essmann99] Essmann U and Berkowitz M. Dynamical properties of phospholipid bilayers from computer simulation. *Biophys J*, **76**, p. 2081, 1999
- [Falck03] Falck E, Punkkinen O, Vattulainen I and Ala-Nissila T. Dynamics and scaling of two-dimensional polymers in a dilute solution. *Phys Rev E*, **68**, p. 050102, 2003
- [Farago03] Farago O. Water-free computer model for fluid bilayer membranes. *J Chem Phys*, **119**, p. 596, 2003
- [Fick55] Fick A. Über Diffusion. *Ann Phys (Leipzig)*, **170**, p. 50, 1855
- [Flekkøy99] Flekkøy E and Coveney P. From molecular dynamics to dissipative particle dynamics. *Phys Rev Lett*, **83**, p. 1775, 1999

BIBLIOGRAPHY

- [Flory49] Flory P. The configuration of real polymer chains. *J Chem Phys*, **17**, p. 303, 1949
- [Flory69] Flory P. *Statistical Mechanics of Chain Molecules*. Interscience New York, 1969
- [Flyvbjerg94] Flyvbjerg H, Holy T and Leibler S. Stochastic dynamics of microtubules: a model for caps and catastrophes. *Phys Rev Lett*, **73**, p. 2372, 1994
- [Forster06] Forster R, Weiß M, Zimmermann T, Reynaud E, Verissimo F, Stephens D and Pepperkok R. Secretory cargo regulates the turnover of COPII subunits at single ER exit sites. *Curr Biol*, **16**, p. 173, 2006
- [Frank00] Frank J. The ribosome - a macromolecular machine par excellence. *Chem Biol*, **7**, p. R133, 2000
- [Geyer04] Geyer T, Gorba C and Helms V. Interfacing brownian dynamics simulations. *J Chem Phys*, **120**, p. 4573, 2004
- [Glick98] Glick B and Malhotra V. The curious state of the Golgi apparatus. *Cell*, **95**, p. 883, 1998
- [Glick00] Glick B. Organisation of the Golgi apparatus. *Curr Opin Cell Biol*, **12**, p. 450, 2000
- [Gorba04] Gorba C, Geyer T and Helms V. Brownian dynamics simulations of simplified cytochrome c molecules in the presence of a charged surface. *J Chem Phys*, **121**, p. 457, 2004
- [Gorter25] Gorter E and Grendel F. On bimolecular layers of lipoids on chromatocytes of blood. *J Exp Medicine*, **41**, p. 439, 1925
- [Groot97] Groot R and Warren P. Dissipative particle dynamics: Bridging the gap between atomistic and mesoscopic simulations. *J Chem Phys*, **107**, p. 4423, 1997
- [Gropp95] Gropp W, Lusk E and Skjellum A. *Using MPI – Portable parallel programming with the message-passing interface*. MIT Press Cambridge, 2nd ed., 1995
- [Guigas06] Guigas G and Weiß M. Size-dependent diffusion of membrane inclusions. *Biophys J*, **91**, p. 2393, 2006

-
- [Guigas07] Guigas G and Weiß M. Probing the nanoscale viscoelasticity of intracellular fluids in living cells. *Biophys J*, **93**, p. 316, 2007
- [Hackstadt00] Hackstadt T. Redirection of host vesicle trafficking pathways by intracellular parasites. *Traffic*, **1**, p. 93, 2000
- [Hancock05] Hancock J. *Cell signaling*. Oxford University Press, 2nd ed., 2005
- [Harroun99] Harroun T, Heller W, Weiss T, Yang L and Huang H. Experimental evidence for hydrophobic matching and membrane-mediated interactions in lipid bilayers containing Gramicidin. *Biophys J*, **76**, p. 937, 1999
- [Hartl96] Hartl F. Molecular chaperones in cellular protein folding. *Nature*, **381**, p. 571, 1996
- [Heinrich05] Heinrich R and Rapoport T. Generation of nonidentical compartments in vesicular transport systems. *J Cell Biol*, **168**, p. 271, 2005
- [Heinzer08] Heinzer S, Wörz S, Kalla C, Rohr K and Weiß M. A model for the self-organization of exit sites in the endoplasmic reticulum. *J Cell Sci*, **121**, p. 55, 2008
- [Helfrich73] Helfrich W. Elastic properties of lipid bilayers: theory and possible experiments. *Z Naturforschung C*, **28**, p. 693, 1973
- [Hell94] Hell S and Wichmann J. Breaking the diffraction resolution limit by stimulated emission. *Opt Lett*, **19**, p. 780, 1994
- [Hoogerbrugge92] Hoogerbrugge P and Koelman J. Simulating microscopic hydrodynamic phenomena with dissipative particle dynamics. *Europhys Lett*, **19**, p. 155, 1992
- [Hooke65] Hooke R. *Micrographia*. Royal Society London, 1665
- [Hoshen76] Hoshen J and Kopelman R. Percolation and cluster distribution I. Cluster labeling technique and critical concentration. *Phys Rev B*, **14**, p. 3438, 1976
- [Illya08] Illya G and Deserno M. Coarse-grained simulation studies of peptide-induced pore formation. *Biophys J*, **95**, p. 4163, 2008

BIBLIOGRAPHY

- [Jakobsen05a] Jakobsen A. Constant-pressure and constant-surface tension simulations in dissipative particle dynamics. *J Chem Phys*, **122**, p. 124901, 2005
- [Jakobsen05b] Jakobsen A, Mouritsen O and Besold G. Artifacts in dynamical simulations of coarse-grained model lipid bilayers. *J Chem Phys*, **122**, p. 204901, 2005
- [Jensen04] Jensen M and Mouritsen O. Lipids do influence protein function - the hydrophobic matching hypothesis revisited. *Biochim Biophys Acta*, **1666**, p. 205, 2004
- [Jiang07] Jiang W, Huang J and Wang Y. Hydrodynamic interaction in polymer solutions simulated with dissipative particle dynamics. *J Chem Phys*, **126**, p. 044901, 2007
- [Kääriäinen84] Kääriäinen L and Ranki M. Inhibition of cell functions by RNA-virus infections. *Annu Rev Microbiol*, **38**, p. 91, 1984
- [Kirkwood35] Kirkwood J. Statistical mechanis of fluid mixtures. *J Chem Phys*, **3**, p. 300, 1935
- [Kohler07] Kohler A and Hurt E. Exporting RNA from the nucleus to the cytoplasm. *Nat Rev Mol Cell Biol*, **8**, p. 761, 2007
- [Kolomeisky08] Kolomeisky A. How polymers translocate through pore: memory is important. *Biophys J*, **94**, p. 1547, 2008
- [Kornberg07] Kornberg R. The molecular basis of eukaryotic transcription. *Proc Nat Acad Sci*, **104**, p. 12955, 2007
- [Kralchevsky95] Kralchevsky P, Paunov V and Denkov N. Stresses in lipid membranes and interactions between inclusions. *J Chem Soc Faraday Trans*, **91**, p. 3415, 1995
- [Kramers40] Kramers H. Brownian motion in a field of force and the diffusion model of chemical reactions. *Physica*, **7**, p. 284, 1940
- [Kumar92] Kumar S, Bouzida D, Swendsen R, Kollman P and Rosenberg J. The Weighted Histogram Analysis Method for Free-Energy Calculations on Biomolecules. I. The Method. *J Comp Chem*, **13**, p. 1011, 1992

-
- [Landau05] Landau D and Binder K. *A guide to Monte Carlo simulations in statistical physics*. Cambridge University Press, 2nd ed., 2005
- [Lanoix01] Lanoix J, Ouwendijk J, Stark A, Szafer E, Cassel D, Deijgaard K, Weiß M and Nilsson T. Sorting of golgi resident proteins into different subpopulations of COPI vesicles: a role for Arfgap1. *J Cell Biol*, **155**, p. 1199, 2001
- [Laradji04] Laradji M and Kumar P. Dynamics of domain growth in self-assembled fluid vesicles. *Phys Rev Lett*, **93**, p. 198105, 2004
- [Lee05] Lee M, Orci L, Hamamoto S, Futai E, Ravazzola M and Schekman R. Sar1p N-terminal helix initiates membrane curvature and completes the fission of a COPII vesicle. *Cell*, **122**, p. 605, 2005
- [Lewis83] Lewis B and Engelman D. Bacteriorhodopsin remains dispersed in fluid phospholipid bilayers over a wide range of bilayer thicknesses. *J Mol Biol*, **166**, p. 203, 1983
- [Lim02] Lim H, Wortis M and Mukhopadhyay R. Stomatocyte-discocyte-echinocyte sequence of the human red blood cell: evidence for the bilayer-couple hypothesis from membrane mechanics. *Proc Nat Acad Sci*, **99**, p. 16766, 2002
- [Lodish04] Lodish H, Berk A, Matsudaira P, Kaiser C, Krieger M and Scott M. *Molecular Cell Biology*. W.H. Freeman and Company, 5th ed., 2004
- [Magde72] Magde D, Elson E and Webb W. Thermodynamic fluctuations in a reacting system - measurement by fluorescence correlation spectroscopy. *Phys Rev Lett*, **29**, p. 705, 1972
- [Maier98] Maier B and Rädler J. Conformation and self-diffusion of single DNA molecules confined to two dimensions. *Phys Rev Lett*, **82**, p. 1911, 1998
- [Majid84] Majid I, Avraham D, Havlin S and Stanley H. Exact-enumeration approach to random walks on percolation clusters in two dimensions. *Phys Rev B*, **30**, p. 1626, 1984
- [Marčelja76] Marčelja S. Lipid-mediated protein interactions in membranes. *Biochim Biophys Acta*, **455**, p. 1, 1976

BIBLIOGRAPHY

- [Meller03] Meller A. Dynamics of polynucleotide transport through nanometre scale pores. *J Physics Cond Matt*, **15**, p. R581, 2003
- [Metzler00] Metzler R and Klafter J. The random walk's guide to anomalous diffusion: a fractional dynamics approach. *Phys Rep*, **339**, p. 1, 2000
- [Mitchinson84] Mitchinson T and Kirschner M. Microtubule assembly nucleated by isolated centrosomes. *Nature*, **312**, p. 232, 1984
- [Mitra04] Mitra K, Ubarretxena-Belandia I, Taguchi T, Warren G and Engelmann D. Modulation of the bilayer thickness of exocytic pathway membranes by membrane proteins rather than cholesterol. *Proc Nat Acad Sci*, **101**, p. 4083, 2004
- [Moradpour07] Moradpour D, Penin F and Rice C. Replication of hepatitis C virus. *Nat Rev Microbiol*, **5**, p. 453, 2007
- [Mouritsen84] Mouritsen O and Bloom M. Mattress model for lipid-protein interactions in membranes. *Biophys J*, **46**, p. 141, 1984
- [Mouritsen05] Mouritsen O. *Life - as a matter of fat. The emerging science of lipidomics*. Springer Berlin Heidelberg, 1st ed., 2005
- [Munro95] Munro S. A comparison of the transmembrane domains of Golgi and plasma membrane proteins. *Biochem Soc Trans*, **23**, p. 527, 1995
- [Muthukumar99] Muthukumar M. Polymer translocation through a hole. *J Chem Phys*, **111**, p. 10371, 1999
- [Muthukumar01] Muthukumar M. Translocation of a confined polymer through a hole. *Phys Rev Lett*, **86**, p. 3188, 2001
- [Muthukumar07] Muthukumar M. Mechanism of DNA transport through pores. *Annu Rev Biophys Biomol Struct*, **36**, p. 435, 2007
- [Nikunen03] Nikunen P, Karttunen M and Vattulainen I. How would you integrate the equations of motion in dissipative particle dynamics? *Comp Phys Comm*, **153**, p. 407, 2003
- [Nilsson89] Nilsson T, Jackson M and Peterson P. Short cytoplasmic sequences serve as retention signals for transmembrane proteins in the endoplasmic reticulum. *Cell*, **58**, p. 707, 1989

-
- [Nilsson93] Nilsson T, Slusarewicz P, Hoe M and Warren G. Kin recognition: A model for retention of golgi enzymes. *FEBS Lett*, **330**, p. 1, 1993
- [Nilsson94] Nilsson T, Hoe M, Slusarewicz P, Rabouille C, Watson R, Hunte F, Watzele G, Berger E and Warren G. Kin recognition between medial Golgi enzymes in HeLa cells. *EMBO J*, **13**, p. 562, 1994
- [Nyquist28] Nyquist H. Thermal agitation of electric charge in conductors. *Phys Rev*, **32**, p. 110, 1928
- [Park04] Park P, Filipek S, Wells J and Palczewski K. Oligomerization of G protein-coupled receptors: past, present and future. *Biochemistry*, **43**, p. 15643, 2004
- [Pasenkiewicz99] Pasenkiewicz M, Takaoka Y, Miyagawa H, Kitamura K and Kusumi A. Charge pairing of headgroups in phosphatidylcholine membranes: A molecular dynamics simulation study. *Biophys J*, **76**, p. 1228, 1999
- [Patterson08] Patterson G, Hirschberg K, Polishchuck R, Gerlich D, Phair R and Lippincott-Schwartz J. Transport through the Golgi apparatus by rapid partitioning within a two-phase membrane system. *Cell*, **133**, p. 1055, 2008
- [Pawson97] Pawson T and Scott J. Signalling through scaffold, anchoring and adaptor proteins. *Science*, **278**, p. 2075, 1997
- [Pelham00] Pelham H and Rothman J. The debate about transport in the Golgi - Two sides of the same coin? *Cell*, **102**, p. 713, 2000
- [Peliti85] Peliti L and Leibler S. Effects of thermal fluctuations on systems with small surface tension. *Phys Rev Lett*, **54**, p. 1690, 1985
- [Phillips05] Phillips J, Braun R, Wand W, Gumbart J, Tajkhorshid E, Villa E, nad RD Skeet CC, Kale L and Schulten K. Scalable molecular dynamics with NAMD. *J Comp Chem*, **26**, p. 1781, 2005
- [Punkkinen05] Punkkinen O, Falck E and Vattulainen I. Dynamics and scaling of polymers in a dilute solution: analytical treatment in two and higher dimensions. *J Chem Phys*, **122**, p. 094904, 2005

BIBLIOGRAPHY

- [Rabouille95] Rabouille C, Hui N, Hunte F, Kieckenbusch R, Berger E, Warren G and Nilsson T. Mapping the distribution of Golgi enzymes involved in the construction of complex oligosaccharides. *J Cell Sci*, **108**, p. 1617, 1995
- [Rapoport07] Rapoport T. Protein translocation across the eukaryotic endoplasmic reticulum and bacterial plasma membranes. *Nature*, **450**, p. 663, 2007
- [Reynwar07] Reynwar B, Illya G, Harmandaris V, Müller M, Kremer K and Deserno M. Aggregation and vesiculation of membrane proteins by curvature-mediated interactions. *Nature*, **447**, p. 461, 2007
- [Riskin96] Riskin H. *The Fokker-Planck Equation*. Springer Berlin, 2nd ed., 1996
- [Ronchi08] Ronchi P, Colombo S, Francolini M and Borgese N. Transmembrane domain-dependent partitioning of membrane proteins within the endoplasmic reticulum. *J Cell Biol*, **181**, p. 105, 2008
- [Rouse53] Rouse P. A theory of the linear viscoelastic properties of dilute solutions of coiling polymers. *J Chem Phys*, **21**, p. 1271, 1953
- [Roux95] Roux B. The calculation of the potential of mean force using computer simulations. *Comp Phys Comm*, **91**, p. 275, 1995
- [Rubinstein06] Rubinstein M and Colby R. *Polymer Physics*. Oxford University Press, 2006
- [Saffman75] Saffman P and Delbrück M. Brownian motion in biological membranes. *Proc Nat Acad Sci*, **72**, p. 3111, 1975
- [Safran03] Safran S. *Statistical thermodynamics of surfaces, interfaces, and membranes*. Westview Press, 1st ed., 2003
- [Schröder77] Schröder H. Aggregation of proteins in membranes. An example of fluctuation-induced interactions in liquid crystals. *J Chem Phys*, **67**, p. 1617, 1977
- [Schrödinger44] Schrödinger E. *What is Life?* Cambridge University Press, 1944

-
- [Schuck04] Schuck S and Simons K. Polarized sorting in epithelial cells: raft clustering and the biogenesis of apical membranes. *J Cell Sci*, **117**, p. 5955, 2004
- [Schutz97] Schutz G, Schindler H and Schmidt T. Single-molecule microscopy on model membranes reveals anomalous diffusion. *Biophys J*, **73**, p. 1073, 1997
- [Schwarz09] Schwarz U. Lecture notes: Theory of soft and bio-matter. <http://www.bioms.de/schwarz/index.php?site=teaching>, 2009. Universität Heidelberg
- [Schwille09] Schwille P and Haustein E. Fluorescence correlation spectroscopy. An introduction to its concepts and applications. www.biophysics.org/education/schwille.pdf, 2009
- [Shannon97] Shannon S and Choy T. Dynamical scaling anomaly for a two dimensional polymer chain in solution. *Phys Rev Lett*, **79**, p. 1455, 1997
- [Shenoy07] Shenoy V, Tambe D, Prasad A and Theriot J. A kinematic description of the trajectories of *Listeria monocytogenes* propelled by actin comet tails. *Proc Nat Acad Sci*, **104**, p. 8229, 2007
- [Shilcock02] Shilcock J and Lipowski R. Equilibrium structure and lateral stress distribution of amphiphilic bilayers from dissipative particle dynamics simulations. *J Chem Phys*, **117**, p. 5048, 2002
- [Shusterman04] Shusterman R, Alon S, Gavrinyov T and Krichevsky O. Monomer dynamics in double- and single-stranded DNA polymers. *Phys Rev Lett*, **92**, p. 0483031, 2004
- [Simons97] Simons K and Ikonen E. Functional rafts in cell membranes. *Nature*, **387**, p. 569, 1997
- [Singer72] Singer S and Nicholson G. The fluid mosaic model of the structure of cell membranes. *Science*, **175**, p. 720, 1972
- [Sintes97] Sintes T and Baumgärtner A. Protein attraction in membranes induced by lipid fluctuations. *Biophys J*, **73**, p. 2251, 1997

BIBLIOGRAPHY

- [Sodeik00] Sodeik B. Mechanisms of viral transport in the cytoplasm. *Trends Microbiol*, **8**, p. 465, 2000
- [Stagg06] Stagg S, Gurkan C, Fowler D, LaPointe P, Foss T, Potter C, Carragher B and Balch W. Structure of the Sec13/31 COPII coat cage. *Nature*, **439**, p. 234, 2006
- [Stephens88] Stephens E and Compans R. Assembly of animal viruses at cellular membranes. *Annu Rev Microbiol*, **42**, p. 489, 1988
- [Stoyan95] Stoyan D, Kendall W and Mecke J. *Stochastic Geometry and its applications*. Wiley, 2nd ed., 1995
- [Szymanski09] Szymanski J and Weiß M. Elucidating the origin of anomalous diffusion in crowded fluids. *Phys Rev Lett*, **103**, p. 038102, 2009
- [Thijssen99] Thijssen J. *Computational Physics*. Cambridge University Press, 1st ed., 1999
- [Torrie74] Torrie G and Valleau J. Monte Carlo free energy estimates using non-Boltzmann sampling: application to the sub-critical Lennard-Jones fluid. *Chem Phys Lett*, **28**, p. 578, 1974
- [vanMeer08] van Meer G, Voelker D and Feigenson G. Membrane lipids: where they are and how they behave. *Nat Rev Mol Cell Biol*, **9**, p. 112, 2008
- [Veatch05] Veatch S and Keller S. Seeing spots: complex phase behaviour in simple membranes. *Biochim Biophys Acta*, **1746**, p. 172, 2005
- [Venturoli99] Venturoli M and Smit B. Simulating the self-assembly of model membranes. *Phys Chem Comm*, **2**, p. 45, 1999
- [Venturoli05] Venturoli M, Smit B and Speretto M. Simulation studies of protein-induced bilayer deformations and lipid-induced protein tilting on a mesoscopic model for lipid bilayers with embedded proteins. *Biophys J*, **88**, p. 1778, 2005
- [Verlet67a] Verlet L. Computer "Experiments" on classical fluids I. Thermodynamical properties of Lennard-Jones molecules. *Phys Rev*, **159**, p. 98, 1967

-
- [Verlet67b] Verlet L. Computer “Experiments” on classical fluids II. Equilibrium correlation functions. *Phys Rev*, **165**, p. 201, 1967
- [Wallace90] Wallace B. Gramicidin channels and pores. *Annu Rev Biophys Biophys Chem*, **19**, p. 127, 1990
- [Wei07] Wei D, Yang W, Jin X and Liao Q. Unforced translocation of a polymer chain through a nanopore: The solvent effect. *J Chem Phys*, **126**, p. 204901, 2007
- [Wei03a] Weiß M, Hashimoto H and Nilsson T. Anomalous protein diffusion in living cells as seen by fluorescence correlation spectroscopy. *Biophys J*, **84**, p. 4043, 2003
- [Wei03b] Weiß M and Nilsson T. A kinetic proof-reading mechanism for protein sorting. *Traffic*, **4**, p. 65, 2003
- [Weisstein09] Weisstein E. Gauss-Bonnet Formula, From MathWorld - A Wolfram Web Resource. <http://mathworld.wolfram.com/Gauss-BonnetFormula.html>, 2009
- [Wikstrom98] Wikstrom M. Proton translocation by bacteriorhodopsin and heme-copper oxidases. *Curr Opin Cell Biol*, **8**, p. 480, 1998
- [Yamamoto02] Yamamoto S, Maruyama Y and Hyodo S. Dissipative particle dynamics study of spontaneous vesicle formation. *J Chem Phys*, **116**, p. 5842, 2002
- [Zilman98] Zilman A and Granek R. Dynamics of fractal sol-gel polymeric clusters. *Phys Rev E*, **58**, p. R2725, 1998
- [Zimm56] Zimm B. Dynamics of polymer molecules in dilute solution: viscoelasticity, flow birefringence and dielectric loss. *J Chem Phys*, **24**, p. 269, 1956

Acknowledgement

In the end, I would like to thank the numerous people who have been involved in the successful finishing of this thesis. I ask for forgiveness if I accidentally miss one or the other.

First of all, I would like to thank Prof. Hausmann at the Kirchhoff-Institute for Physics in Heidelberg for his interest in my work. I really appreciate his willingness to serve as a referee for the Faculty of Physics and Astronomy.

Special thanks go to Matthias Weiß, head of our working group. His ever-positive way of thinking, his ability to inspire and to fascinate and his talent for clear illustrations have been a great support during the last three years. It was a pleasure to meet such an excellent scientist and wonderful person.

Not to forget my colleagues of the Cellular Biophysics group without whom the last years would not have been as interesting and delightful, and who supported me in numerous aspects. In particular, Gernot Guigas, who was, is and always will be a competent expert in dissipative particle dynamics; Marcel Hellmann, Jens Kühnle and Jędrzej Szymanski for discussing various physical issues; Diana Morozova for helpful comments on DPD simulations; Nina 'Rulez' Malchus for her biological expertise. Many thanks especially to Felix Kapahnke who pointed out a bug in one of the simulation codes, and to Claudia Kalla for taking care of my laboratory experiments. Thanks go also to Kristian Boye, Maria Hanulova and Laura Weimann.

My parents, sisters and brother are also deeply acknowledged. Thank you for encouraging and trusting me in every possible aspect.

What would the years of study be like without friends? Surely not as joyful and fun as with you: Axel, Bernd, David, Fabian, Florian D, Florian L, Franziska, Marcel, Marion, Max, Micha M, Micha V, Moritz, Nina, Tobias D, Tobias S, Ulrike.

A special person whose contribution was exclusively on the non-scientific side is Birte. Thank you so much for your understanding and tolerance, the patience you had with me and the strength and love you gave me.

List of Publications

U. Schmidt[†], G. Guigas[†] and M. Weiß

Cluster formation of transmembrane proteins due to hydrophobic mismatching
Phys Rev Lett, **101**, 128104 (2008)

U. Schmidt and M. Weiß

Facilitating protein sorting in the secretory pathway by hydrophobic mismatching
(in revision)

F. Kapahnke[†], U. Schmidt[†], D.W. Heermann and M. Weiß

Polymer translocation through a nanopore – the effect of solvent conditions
(in revision)

[†] equal contribution

